# INNOVATIVE THERMAL MANAGEMENT OF ELECTRONICS USED IN OIL WELL LOGGING

A Thesis
Presented to
The Academic Faculty

by

Juan-Carlos Jakaboski

In Partial Fulfillment
of the Requirements for the Degree
Master of Science in Mechanical Engineering

Georgia Institute of Technology

April 2004

# INNOVATIVE THERMAL MANAGEMENT OF ELECTRONICS USED IN OIL WELL LOGGING

Approved by:

Dr. Yogendra Joshi, Advisor

Dr. S. Mostafa Ghiaasiaan

Dr. Bruce H. Storm, Jr.

Date Approved: April 28, 2004

*To my wife, Blake, whom I love very much*

# ACKNOWLEDGEMENTS

I thank God for His rich blessings in my life, and for His Son, Jesus Christ, the Author of my faith. I thank Him for blessing me with a wonderful family, magnificent parents, and an extraordinary wife. My parents deserve a great amount of recognition for their love, encouragement, and dedication over the years. I owe a great deal of my success and accomplishments to them. The emotional, physical, and spiritual support from my wife the past few years has been phenomenal. Words cannot express the respect and admiration I have for her.

I would also like to thank my advisor, Dr. Yogendra Joshi, for his guidance, advice, and direction throughout this research effort. Dr. Bruce Storm from Halliburton Energy Services deserves special thanks for being the catalyst of this research. I am grateful for his vision, leadership and for giving us the freedom and resources to do the best job possible. Dr. Mostafa Ghiaasiaan provided many valuable suggestions, and I thank him for serving on my committee. I enjoyed working closely with Dr. Qinghua Wang the past two years, and appreciate his computer modelling advice.

Many people at Halliburton Energy Services made significant contributions to this undertaking. Special thanks to Jimmy Anders for the countless times I asked him to order equipment, and we had it the next day, and for assembling the thermal test boards. I thank Brent Phillips for his mechanical design efforts, for shepherding the construction of many prototype parts, and for his practical advice. I also thank Haoshi Song for his insight and help during the outset of this research.

This material is based upon work supported under a National Science Foundation Graduate Research Fellowship. Any opinions, findings, conclusions or recommendations expressed in this publication are those of the author and do not necessarily reflect the views of the National Science Foundation.

# TABLE OF CONTENTS

**ACKNOWLEDGEMENTS** . . . . . . . . . . . . . . . . . . . . . . . . **iv**

**LIST OF TABLES** . . . . . . . . . . . . . . . . . . . . . . . . . . **ix**

**LIST OF FIGURES** . . . . . . . . . . . . . . . . . . . . . . . . . **x**

**ABSTRACT** . . . . . . . . . . . . . . . . . . . . . . . . . . . . . **xv**

**CHAPTER 1 INTRODUCTION AND BACKGROUND** . . . . . **1**

1.1 Wireline versus LWD . . . . . . . . . . . . . . . . . . . . . . 2

1.2 Motivation . . . . . . . . . . . . . . . . . . . . . . . . . . . . 2

1.3 A Survey of Existing Patents . . . . . . . . . . . . . . . . . . 4

1.3.1 Thermoelectric Cooling . . . . . . . . . . . . . . . . . . 5

1.3.2 Vapor Compression Refrigeration . . . . . . . . . . . . . 7

1.3.3 Sorption Cooling . . . . . . . . . . . . . . . . . . . . . . 9

1.3.4 Thermal Insulation Techniques . . . . . . . . . . . . . . 10

1.3.5 Convection Cooling Cycle . . . . . . . . . . . . . . . . . 12

1.3.6 Refrigerant Circulation Cooling . . . . . . . . . . . . . . 12

1.3.7 Evaporative Thermal Protection . . . . . . . . . . . . . . 13

1.3.8 Thermoacoustic Refrigeration . . . . . . . . . . . . . . . 14

**CHAPTER 2 DESIGN TARGETS AND OVERALL CONCEPT** **16**

2.1 Design Targets . . . . . . . . . . . . . . . . . . . . . . . . . . 16

2.2 Conceptual Design . . . . . . . . . . . . . . . . . . . . . . . . 16

2.3 Concept-Specific Design Goals . . . . . . . . . . . . . . . . . 18

**CHAPTER 3 DETAILED DESCRIPTION OF PROTOTYPE** . . **21**

3.1 Overview of Prototype . . . . . . . . . . . . . . . . . . . . . 21

3.2 Vacuum Flask . . . . . . . . . . . . . . . . . . . . . . . . . . 22

3.3 Phase Change Material . . . . . . . . . . . . . . . . . . . . . 23

3.4 Phase Change Material Container . . . . . . . . . . . . . . . 24

3.5 Expansion Disk . . . 26
3.6 Coiled Tubing Heat Exchanger . . . 26
3.7 Thermocouple Probes . . . 27
3.8 Aluminum Adapter . . . 29
3.9 Cold Plate . . . 29
3.10 Inlet/Outlet Coolant Temperature Measurement . . . 31
3.11 Tube-Side Heat Transfer Enhancement . . . 32
3.12 Coolant Pump . . . 33
3.13 Fluid Expansion Compensator . . . 34
3.14 Thermal Test Chips . . . 36
3.15 Thermal Interface Material . . . 39

**CHAPTER 4 PROTOTYPE PERFORMANCE EXPERIMENTS 40**

4.1 Purpose . . . 40
4.2 Approach . . . 40
4.3 Apparatus and Procedure . . . 42
4.3.1 Evacuation and Fill Station . . . 42
4.3.2 Leak Test . . . 46
4.3.3 Oven . . . 46
4.3.4 Initial Setup and Tear Down . . . 47
4.4 Data Acquisition . . . 53
4.4.1 Hardware . . . 53
4.4.2 Software . . . 54
4.5 Results and Discussion . . . 60
4.5.1 Baseline Experiments . . . 60
4.5.2 Constant Chip Power Experiments . . . 64
4.5.3 Constant Flow Rate Experiments . . . 67
4.5.4 Control System Experiment . . . 70

**CHAPTER 5 FLOW RATE CORRELATION EXPERIMENTS . 73**

5.1 Purpose . . . . . . . . . . . . . . . . . . . . . . . . . . . . . 73

5.2 Approach . . . . . . . . . . . . . . . . . . . . . . . . . . . . 73

5.3 Apparatus and Procedure . . . . . . . . . . . . . . . . . . . . 74

5.4 Data Acquisition . . . . . . . . . . . . . . . . . . . . . . . . 75

5.4.1 Hardware . . . . . . . . . . . . . . . . . . . . . . . . 75

5.4.2 Software . . . . . . . . . . . . . . . . . . . . . . . . 75

5.5 Results and Discussion . . . . . . . . . . . . . . . . . . . . . 76

**CHAPTER 6 VACUUM FLASK THERMAL PERFORMANCE EXPERIMENTS . . . . . . . . . . . . . . . . . . . . . . . . . . 80**

6.1 Purpose . . . . . . . . . . . . . . . . . . . . . . . . . . . . . 80

6.2 Approach . . . . . . . . . . . . . . . . . . . . . . . . . . . . 80

6.3 Apparatus and Procedure . . . . . . . . . . . . . . . . . . . . 81

6.4 Thermocouple Probe . . . . . . . . . . . . . . . . . . . . . . . 86

6.5 Data Acquisition . . . . . . . . . . . . . . . . . . . . . . . . 87

6.5.1 Hardware . . . . . . . . . . . . . . . . . . . . . . . . 87

6.5.2 Software . . . . . . . . . . . . . . . . . . . . . . . . 88

6.6 Results and Discussion . . . . . . . . . . . . . . . . . . . . . 89

**CHAPTER 7 TUBE-SIDE HEAT TRANSFER EXPERIMENTS 93**

7.1 Purpose . . . . . . . . . . . . . . . . . . . . . . . . . . . . . 93

7.2 Approach . . . . . . . . . . . . . . . . . . . . . . . . . . . . 93

7.3 Apparatus and Procedure . . . . . . . . . . . . . . . . . . . . 95

7.4 Data Acquisition . . . . . . . . . . . . . . . . . . . . . . . . 100

7.4.1 Hardware . . . . . . . . . . . . . . . . . . . . . . . . 100

7.4.2 Software . . . . . . . . . . . . . . . . . . . . . . . . 100

7.5 Results and Discussion . . . . . . . . . . . . . . . . . . . . . 102

**CHAPTER 8 SUMMARY AND CONCLUSIONS . . . . . . . . . . 106**

**APPENDIX A — PROTOTYPE PERFORMANCE DATA . . . . 111**

**APPENDIX B — VACUUM FLASK THERMAL PERFORMANCE DATA** . . . . . . . . . . . . . . . . . . . . . . . . . . . . . . . . . . . . . . **120**

**APPENDIX C — LABVIEW$^{TM}$ BLOCK DIAGRAMS** . . . . . . . . **124**

**APPENDIX D — UNCERTAINTY ESTIMATES** . . . . . . . . . . . **140**

**REFERENCES** . . . . . . . . . . . . . . . . . . . . . . . . . . . . . . . . . **145**

# LIST OF TABLES


Table 2.1 Design Targets for Prototype Thermal Management System . . . 16

Table 2.2 Design Goals Specific to Thermal Management Concept . . . . . 20

Table 3.1 Properties of *Cerrobend* . . . . . . . . . . . . . . . . . . . . . . . 24

Table 3.2 Thermal Test Chip Details . . . . . . . . . . . . . . . . . . . . . . 37

Table 4.1 Apparatus Used in Evacuation and Fill Station for Prototype . . 45

Table 4.2 Summary of Prototype Performance Experiments . . . . . . . . . 61

Table 6.1 Apparatus Used in Vacuum Flask Thermal Performance Experiments 85

Table 6.2 Procedure for Vacuum Flask Thermal Performance Experiments . 85

Table 6.3 Results from Vacuum Flask Thermal Performance Experiments . 92

Table 7.1 Apparatus Used in Tube-Side Heat Transfer Experiments . . . . . 99

Table 7.2 Procedure for Tube-Side Heat Transfer Experiments . . . . . . . . 99

Table 7.3 Heat Transfer Coefficient Results for Tube with HiTRAN® . . . 103

Table 7.4 Heat Transfer Coefficient Results for Plain Tube . . . . . . . . . . 104

Table D.1 *Run E* values used in estimate of uncertainty of $U$ . . . . . . . . . 144

# LIST OF FIGURES

Figure 1.1 Schematic of a Borehole Wireline Measurement . . . . . . . . . . 3
Figure 2.1 Overall Concept of Thermal Management System . . . . . . . . . 18
Figure 3.1 Overall Schematic of Prototype . . . . . . . . . . . . . . . . . . . 21
Figure 3.2 Vacuum Flask Used for Prototype Thermal Management System . 22
Figure 3.3 Vacuum Flask End Cap, PEEK Stopper and Stainless Steel Adapter 23
Figure 3.4 Close-up CAD Drawing of PCM End Cap and Compression Fittings 25
Figure 3.5 CAD Drawing of Phase Change Material Container . . . . . . . . 26
Figure 3.6 CAD Drawing of Heat Exchanger and Thermocouple Probes . . . 27
Figure 3.7 Schematic of Thermocouple Probe, Thermocouples Spaced as Shown 28
Figure 3.8 CAD Drawing of Aluminum Adapter . . . . . . . . . . . . . . . . 29
Figure 3.9 Exploded CAD Drawing of Cold Plate, Side Rails, and PCBs . . 31
Figure 3.10 Close-up of HiTRAN® Matrix Element . . . . . . . . . . . . . . 32
Figure 3.11 Top View of Coolant Pump, Pump Motor, and Flow Loop Plumping 34
Figure 3.12 Top View of Fluid Expansion Compensator and Flow Loop Lines 35
Figure 3.13 Schematic of Thermal Test Chip Cross Section . . . . . . . . . . . 38
Figure 3.14 Circuit Diagram for Big and Small Thermal Test Chips . . . . . . 38
Figure 3.15 Thermal Test Chips, Two Big, One Small, Soldered to PCB . . . 38
Figure 3.16 PCBs Mounted to Cold Plate using Thermal Interface Material . 39
Figure 4.1 Close-up of Evacuation and Fill Station . . . . . . . . . . . . . . . 43
Figure 4.2 Prototype Connected to Evacuation and Fill Station . . . . . . . 45
Figure 4.3 Oven Used in Prototype Performance Tests . . . . . . . . . . . . 47
Figure 4.4 Fully Assembled Tool Resting on Table Prior to Test . . . . . . . 48
Figure 4.5 Tool Lowered into Oven Using Hoist, Leveller, and Tow Straps . . 50
Figure 4.6 Protoype Tool Resting in Work Chamber of Oven . . . . . . . . . 51
Figure 4.7 Close-up View of Marinite End Caps and Feed-through Wires . . 52
Figure 4.8 Schematic of DAQ Hardware Used in Prototype Experiments . . . 53

Figure 4.9 Front View of *Agilent* Data Acquisition Unit and Power Supply . 55
Figure 4.10 Thermocouples Wired to *Agilent* 34901A Multiplexer Module . . 56
Figure 4.11 *Main Temp Logger* User Interface, Top Window . . . . . . . . . . 57
Figure 4.12 *Main Temp Logger* User Interface, Bottom Window . . . . . . . . 58
Figure 4.13 Various Temperatures vs Time, Baseline 1 . . . . . . . . . . . . . 62
Figure 4.14 Temperature Gradient vs Time, Probe 1, Baseline 1 . . . . . . . . 63
Figure 4.15 Temperature Gradient vs Time, Probe 2, Baseline 1 . . . . . . . . 63
Figure 4.16 Various Temperatures vs Time, Constant Power 1 . . . . . . . . . 64
Figure 4.17 Temperature Gradient vs Time, Probe 1, Constant Power 1 . . . 65
Figure 4.18 Temperature Gradient vs Time, Probe 2, Constant Power 1 . . . 65
Figure 4.19 Total Run Time vs Flow Rate for Constant Chip Power Experiments 66
Figure 4.20 Various Temperatures vs Time, Constant Flow 1 . . . . . . . . . 67
Figure 4.21 Temperature Gradient vs Time, Probe 1, Constant Flow 1 . . . . 68
Figure 4.22 Temperature Gradient vs Time, Probe 2, Constant Flow 1 . . . . 69
Figure 4.23 Highest Chip Temperature vs Time for 2W, 5W, 10W, 15W, 18W 69
Figure 4.24 Time Chips Remain Below 95 Celsius vs Power Dissipated . . . . 70
Figure 4.25 Various Temperatures vs Time, Variable Flow . . . . . . . . . . . 71
Figure 4.26 Temperature Gradient vs Time, Probe 1, Variable Flow . . . . . . 71
Figure 4.27 Temperature Gradient vs Time, Probe 1, Variable Flow . . . . . . 72
Figure 5.1 Flow Sensor Added to Closed Flow Loop of Prototype . . . . . . 74
Figure 5.2 Schematic of DAQ Hardware for Flow Rate Correlation . . . . . . 75
Figure 5.3 Average Flow Rate vs Pump Voltage at Room Temperature . . . 77
Figure 5.4 Average Flow Rate vs Pump Voltage at 30 Celsius . . . . . . . . 78
Figure 5.5 Average Flow Rate vs Pump Voltage at 40 Celsius . . . . . . . . 78
Figure 5.6 Pump Power Consumption vs Flow Rate at 30 Celsius . . . . . . 79
Figure 6.1 Hot Plate, Stock Pot, Hand Drill, and Drill Pump . . . . . . . . . 82
Figure 6.2 Vacuum Flask Tipped onto Roller Stand . . . . . . . . . . . . . . 83
Figure 6.3 Overview of Setup for Vacuum Flask Performance Experiments . 84
Figure 6.4 Custom Thermocouple Probe and Thermocouple Spacing . . . . . 87

Figure 6.5 Close-up of Thermocouple Probe . . . . . . . . . . . . . . . . . . 87
Figure 6.6 Schematic of Data Acquisition Hardware Used to Test Vacuum Flask 88
Figure 6.7 Axial Temperature Gradient in Vacuum Flask vs Time, *Run A* . . 89
Figure 6.8 Axial Temperature Gradient in Vacuum Flask vs Time, *Run B* . 90
Figure 6.9 Average Internal Vacuum Flask Temperature vs Time, *Run A* . . 91
Figure 6.10 Average Internal Vacuum Flask Temperature vs Time, *Run B* . . 91
Figure 7.1 Schematic of Setup used in Tube-Side Heat Transfer Experiments 94
Figure 7.2 Overview of Setup for Tube-Side Heat Transfer Experiments . . . 96
Figure 7.3 Close-up of Pump, Inlet Thermocouple, and Heater Controller . . 97
Figure 7.4 Close-up of Flow Sensor, and Outlet Thermocouple Probe . . . . 98
Figure 7.5 Schematic of DAQ Hardware for Heat Transfer Experiments . . . 101
Figure 7.6 *Hitran* User Interface . . . . . . . . . . . . . . . . . . . . . . . . 101
Figure 7.7 Results for Heat Transfer Coefficient vs Flow Rate . . . . . . . . 105
Figure A.1 Various Temperatures vs Time, Baseline 2 . . . . . . . . . . . . . 112
Figure A.2 Temperature Gradient vs Time, Probe 1, Baseline 2 . . . . . . . . 112
Figure A.3 Temperature Gradient vs Time, Probe 2, Baseline 2 . . . . . . . . 113
Figure A.4 Various Temperatures vs Time, Constant Power 2 . . . . . . . . . 113
Figure A.5 Temperature Gradient vs Time, Probe 1, Constant Power 2 . . . 114
Figure A.6 Temperature Gradient vs Time, Probe 2, Constant Power 2 . . . 114
Figure A.7 Various Temperatures vs Time, Constant Power 3 . . . . . . . . . 115
Figure A.8 Temperature Gradient vs Time, Probe 1, Constant Power 3 . . . 115
Figure A.9 Temperature Gradient vs Time, Probe 2, Constant Power 3 . . . 116
Figure A.10 Various Temperatures vs Time, Constant Power 4 . . . . . . . . . 116
Figure A.11 Temperature Gradient vs Time, Probe 1, Constant Power 4 . . . 117
Figure A.12 Temperature Gradient vs Time, Probe 2, Constant Power 4 . . . 117
Figure A.13 Various Temperatures vs Time, Constant Flow 2 . . . . . . . . . 118
Figure A.14 Various Temperatures vs Time, Constant Flow 3 . . . . . . . . . 118
Figure A.15 Various Temperatures vs Time, Constant Flow 4 . . . . . . . . . 119
Figure B.1 Axial Temperature Gradient in Vacuum Flask vs Time, *Run C* . 121

Figure B.2 Average Internal Vacuum Flask Temperature vs Time, *Run C* . . 121
Figure B.3 Axial Temperature Gradient in Vacuum Flask vs Time, *Run D* . 122
Figure B.4 Average Internal Vacuum Flask Temperature vs Time, *Run D* . . 122
Figure B.5 Axial Temperature Gradient in Vacuum Flask vs Time, *Run E* . 123
Figure B.6 Average Internal Vacuum Flask Temperature vs Time, *Run E* . . 123
Figure C.1 *Main Temp Logger*, Northwest Corner . . . . . . . . . . . . . . . 125
Figure C.2 Main Temp Logger, Northeast Corner . . . . . . . . . . . . . . . . 125
Figure C.3 *Main Temp Logger*, Southeast Corner . . . . . . . . . . . . . . . . 126
Figure C.4 *Main Temp Logger*, Southwest Corner . . . . . . . . . . . . . . . 126
Figure C.5 *+6V Power Control*, Manual Mode . . . . . . . . . . . . . . . . . 127
Figure C.6 *+6V Power Control*, Automatic Mode, Internal Case 0 . . . . . . 127
Figure C.7 *+6V Power Control*, Automatic Mode, Internal Case 1 . . . . . . 128
Figure C.8 *+6V Power Control*, Automatic Mode, Internal Case -1 . . . . . . 128
Figure C.9 *-25V Power Control*, Manual Mode . . . . . . . . . . . . . . . . . 129
Figure C.10 *-25V Power Control*, Automatic Mode, Internal Case 0 . . . . . . 129
Figure C.11 *-25V Power Control*, Automatic Mode, Internal Case 1 . . . . . . 130
Figure C.12 *-25V Power Control*, Automatic Mode, Internal Case -1 . . . . . . 130
Figure C.13 *Pump Power Control*, Manual Mode . . . . . . . . . . . . . . . . 131
Figure C.14 *Pump Power Control*, Automatic Mode, Internal Case 0 . . . . . 131
Figure C.15 *Pump Power Control*, Automatic Mode, Internal Case 1 . . . . . 132
Figure C.16 *Pump Power Control*, Automatic Mode, Internal Case -1 . . . . . 133
Figure C.17 *High Chip Temp* SubVI . . . . . . . . . . . . . . . . . . . . . . . 133
Figure C.18 *Flow Rate vs Voltage Logger*, Northwest Corner . . . . . . . . . . 134
Figure C.19 *Flow Rate vs Voltage Logger*, Northeast Corner . . . . . . . . . . 134
Figure C.20 *Flow Rate vs Voltage Logger*, Southeast Corner . . . . . . . . . . 135
Figure C.21 *Flow Rate vs Voltage Logger*, Southwest Corner . . . . . . . . . . 135
Figure C.22 *F vs V Pump Control*, External Case 0 . . . . . . . . . . . . . . . 136
Figure C.23 *F vs V Pump Control*, External Case 1, Internal Case True . . . . 136
Figure C.24 *F vs V Pump Control*, External Case 1, Internal Case False . . . . 137

Figure C.25 *F vs V Pump Control*, External Case -1, Internal Case True . . . 137
Figure C.26 *F vs V Pump Control*, External Case -1, Internal Case False . . . 138
Figure C.27 *Hitran*, Left Side, Internal Case True . . . . . . . . . . . . . . . . . 138
Figure C.28 *Hitran*, Left Side, Internal Case False . . . . . . . . . . . . . . . . . 139

# ABSTRACT

The oil and gas industries use sophisticated logging tools during and after drilling. These logging tools employ internal electronics for sensing viscosity, pressure, temperature, and other important quantities. To protect the sensitive electronics, which typically have a maximum allowable temperature of 100 °C, they are shielded and insulated from the harsh external drilling environment. The insulation reduces the external heat input, but it also makes rejection of the heat generated within the electronics challenging. Electronic component failures promoted by elevated temperatures, and thermal stress, require a time consuming and expensive logging tool replacement process. Better thermal management of the electronics in logging tools promises to save oil and gas companies time and money.

This research focuses on this critical thermal management challenge. Specifically, this thesis describes the design, fabrication, and test of an innovative thermal management system capable of cooling commercial-off-the-shelf electronics for extended periods in harsh ambient temperatures exceeding 200 °C. Resistive heaters embedded in quad-flat-packages simulate the electronics used in oil well logging. A custom high temperature oven facilitates the evaluation of a full scale prototype of the thermal management system. We anticipate the prototype device will validate computer modeling efforts on which its design was based, and advance future designs of the thermal management system.

# CHAPTER 1

# INTRODUCTION AND BACKGROUND

In order to find and reach underground hydrocarbon deposits, oil and gas industries must drill holes into the earth, often thousands of feet deep. Drilling such a deep hole requires a drill bit connected to many lengths of pipe or coiled tubing, known as the drill string. The surface end of the drill string, called the drilling rig, includes a rotating system that rotates the drill string, causing the drill bit to plunge deeper into the earth. The lower end of the drill string, known as the down hole assembly, often includes many sophisticated sensors. For example, these include magnetic resonance imaging (MRI) sensors, gamma scintillators, which are used to determine the radioactivity of a rock formation, and nuclear detectors, which measure density and porosity of a formation [8].

These sensors and supporting electronics provide information as the drill bit advances into the rock formation, known as logging-while-drilling (LWD), or measurement-while-drilling (MWD). Much like a desktop computer or laptop, the electronics in a down hole assembly consist of components to store and process data, printed circuit boards, power converters, etc. However, unlike a desktop computer, which operates in a relatively benign room temperature environment, the environmental conditions in a subterranean bore hole can be extremely harsh. Both pressure and temperature tend to increase with depth into the earth. Downhole temperatures in excess of 200 °C, and pressures greater than 135 MPa (20,000 psi) are not uncommon. High shock and vibration during the drilling process also characterize the downhole environment. LWD sensors must often remain in this harsh environment up to several weeks [13].

## 1.1 Wireline versus LWD

Another way to gain information about a formation is after a bore hole has been drilled. Known as wireline logging, this type of measurement technique involves lowering a measurement tool into a cased or open bore hole on a wireline, or cable [26]. This cable serves as the mechanical and electrical conduit of the wireline tool. The electrical lines in a cable are used both for data transmission to and from the surface, and to power downhole components. Like LWD tools, wireline tools carry a host of sophisticated sensors to monitor and record quantities such as temperature, pressure, rock resistivity, and porosity, etc. The electronics aboard a wire-line tool may include data acquisition boards, motor amplifier boards, and printed circuit board electronics for other tasks. Unlike LWD tools, wireline tools usually stay in the down hole environment for no more than twenty-four hours. However, wireline tools often carry high-power electronic components that may dissipate up to 100 Watts of power, whereas the electronics in LWD tools usually dissipate up to 10 Watts [8]. Figure 1.1 shows a schematic of a wireline measurement in a borehole.

## 1.2 Motivation

High temperature electronic components exist that can operate at temperatures as high as 300 °C. However, the number of commercial vendors and the variety of high temperature electronic components and sensors that can withstand such high temperatures is very limited. Available high temperature electronic components, which often require silicon-on-insulator technology at the semiconductor level, and high temperature die-attach materials, solder, and printed circuit boards at the packaging level can be very expensive [20]. Add to this the cost of selection, screening, and maintenance, and the costs associated with using high temperature electronic components in downhole LWD and wireline tools quickly becomes prohibitively expensive. Fortunately, many commercial vendors market a large variety of electronic

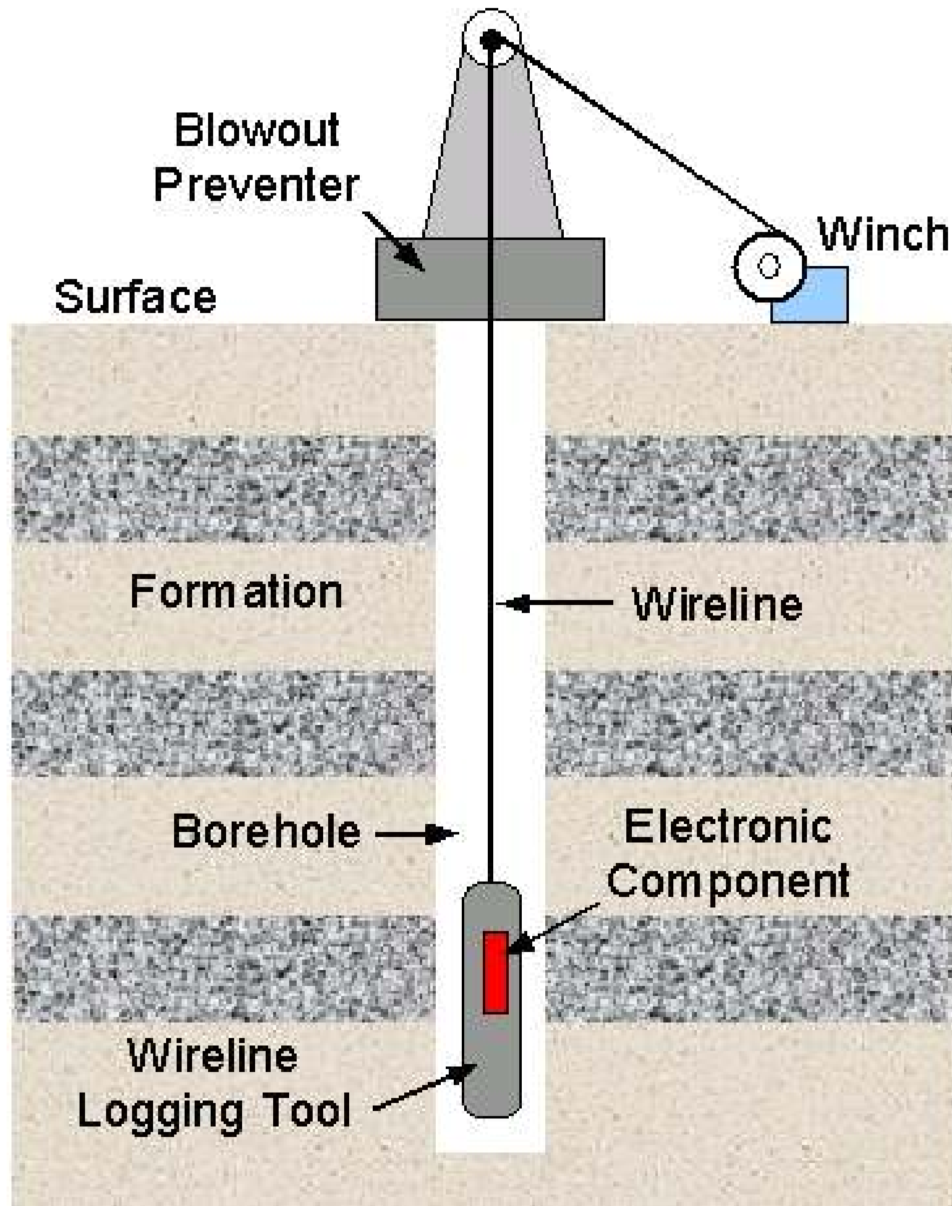


**Figure 1.1:** Schematic of a Borehole Wireline Measurement

components that can continuously operate up to 125 °C [19]. Therefore, most LWD and wireline tools today contain these commercial-off-the-shelf electronic components.

The standard thermal management approach to protect commercial-off-the-shelf electronic components from high borehole temperatures (around 200 °C) consists of insulating them from the environment [3]. This insulation keeps heat out, but it also prevents rejection of heat produced by the components themselves. Overheating results in thermal failure and reduced life expectancy of the electronic components. This is very expensive for two main reasons. First, there are significant parts and labor costs associated with replacement of the electronic components. Second, and more importantly, thermal failure of these components often occurs during drilling. This requires a time consuming removal and replacement process, which increases the cost to operate the entire drilling rig, and not just the logging tool. Better thermal management of commercial-off-the-shelf electronic components used in well logging promises to save significant time and money.

In the highly competitive oil-exploration industry, the company that has better electronics cooling technology also gains three important competitive advantages. First, the technology allows longer use of logging tools in relatively cooler boreholes, with temperatures of about 150 °C. Second, better electronics cooling technology leads to increased market share of logging services for deeper, hotter boreholes, with temperatures exceeding 200 °C. Third, the technology facilitates the use of new high-performance logic and processing electronic components, which equates to better, more accurate downhole measurements.

## *1.3 A Survey of Existing Patents*

Many U.S. patents disclose methods for cooling electronic components in the high temperatures and pressures of subterranean bore holes. This section provides an extensive, though not comprehensive, review of several such patents. The cooling

techniques often seek to dissipate excess heat from electronics to the surrounding well bore fluids, shield the electronics from high temperatures, or a combination of the two. Several inventions employ thermoelectric coolers, heat pipes, and thermally conductive materials to drive the excess heat from electronics to the surrounding well bore fluids. Other inventions describe novel insulation methods to shield electronic components or cooling fluids from the surrounding high temperatures. Many inventions use thermodynamic cycles such as vapor compression refrigeration. Still others use techniques such as sorption cooling, convection cooling, and refrigerant circulation. One patent describes a compact acoustic refrigerator to actively cool electronic components.

### 1.3.1 Thermoelectric Cooling

U.S. Pat. No. 6,134,892 to Turner et al. presents a thermoelectric system for cooling downhole electronic components [28]. The system includes thermally conductive potting, an electronics shell, a thermoelectric cooler, a cylindrical pressure housing, a thermally conductive strip, and a spring mechanism. The electronics are mounted to a substrate and surrounded by a thermally conductive potting. The potting features many longitudinally extending ridges that allow for thermal expansion of the potting at high temperatures. An electronics shell encloses the potting, electronics, and substrate. Heat passes through the potting and shell from the electronics to the thermoelectric cooler. Thermoelectric coolers transfer heat from the electronics to the thermally conductive strip, and through the pressure housing for dissipation to the passing drill fluids. A spring mechanism forces all components together to maintain good thermal contact, to minimize heat transfer from the environment to the electronics, and to absorb downhole shock, vibration, and thermal expansion.

U.S. Pat. No. 5,931,000 to Turner et al. discloses another thermoelectric downhole electronics cooling system [27]. In one embodiment, the system contains thermally

conductive potting, an electronics chassis, several thermoelectric coolers, a cylindrical pressure housing, thermally conductive silicone rubber, thermal interface material, thermal insulating material, several springs, and several guide pins. In general, heat flows from the electronics, through several system components, and ultimately to the housing for dissipation to the well fluids. The thermally conductive potting and silicone rubber serve as efficient thermal conductors, and absorb differential thermal expansion of other components. Placed between many component surfaces, thermal interface material lowers the resistance to heat transfer between dissimilar materials. Thermal insulating materials reduce heat transfer from the surroundings to the electronics and thermoelectric coolers. The springs and guide pins force the electronics chassis outward to provide good contact with the inner surface of the cylindrical pressure housing, to absorb thermal expansion of the system components, and to provide a means to withstand shock and vibration. Other embodiments of the invention consist of devices such as wedges, springs, thermal expansion materials, expanding foam, and careful machining to ensure good thermal contact between electrical components, and to account for differential thermal expansion between components.

U.S. Pat. Nos. 5,730,217, 5,720,342, and 5,547,028 to Owens et al. describe a thermoelectric cooling system for extending the lifetime of electronic components in a high temperature well [21] [22] [23]. The system features several electronic components, a printed circuit board, a thermoelectric cooler, a thermal conductor, thermal grease, cover with O-ring, and an evacuated interior space. The printed circuit board supports the electronic components, and a thermal conductor contains several shaped surfaces that match the shape of the electronic components. The thermal conductor provides an efficient thermal path between the electronics and the cold end of the thermoelectric cooler. As current passes through the thermoelectric cooler, it transfers heat from its cold end to its hot end. Thermal grease occupies the interface space between the hot end of the thermoelectric cooler and the annular wall of the

well tool. Ultimately, the thermoelectric cooler transfers heat from the electronics to the well bore fluids, even though the electronics are at a lower temperature than the well bore fluids. A cover protects the electronics and thermoelectric cooler from the surrounding well fluids, and an O-ring provides a seal about the cover. An evacuated interior space surrounds the electronic components to insulate them from the high temperature surroundings.

U.S. Pat. No. 4,375,157 to Boesen relates a thermoelectric cooling system that cools electronic components well below the downhole ambient temperature [4]. The invention includes several thermoelectric coolers, a vacuum flask with thermal insulation stopper, a vapor phase heat transfer pipe, and heat conducting fins. Arranged in a multi-stage configuration, the thermoelectric coolers pump heat "uphill" against the temperature gradient from the cold end attached to the electronic components to the hot end joined to the vapor phase heat transfer pipe. The heat pipe protrudes through the thermal insulation stopper, and transfers heat "downhill" to the surrounding well bore fluid, which is at a lower temperature than the hot end of the multi-stage thermoelectric system. Heat conducting fins aid heat transfer from the heat pipe to the well bore fluid. A vacuum flask surrounds the thermoelectric cooler assembly and electronic components to insulate them from the hot ambient environment. Boesen claims his system can maintain an electronics temperature of 135 °C indefinitely while in ambient bore hole temperatures of 200 °C.

### 1.3.2 Vapor Compression Refrigeration

U.S. Pat. No. 5,701,751 to Flores reveals a vapor compression cooling system for actively cooling downhole electronic circuits in high temperature environments [11]. The system contains a lower tank, and electronics chassis with integral heat pipes, an upper tank, a high temperature compressor, and a dewar. The dewar surrounds the lower tank, electronics chassis, and integral heat pipes. Heat pipes

transfer heat from the electronics to the lower tank, which contains approximately one liter of water. The water eventually vaporizes as it heats up, and rises to the high temperature compressor. The components of this reciprocating compressor are rated for temperatures up to 232 °C, and a downhole time of 1000 hours at shaft speeds of 2000 rpm. A 500 Watt downhole electric motor spins the crankshaft of the compressor via a universal joint. Compressed water vapor rises to the upper tank. The upper tank, sized at least 1.16 times larger than the lower tank, stores the high pressure steam and transfers the steam's heat to the surrounding well bore by conduction through its walls. A control system between the compressor and lower tank maintains a constant value for the vaporization pressure in the lower tank. Cooling action ceases when all the water in the lower tank vaporizes, but refilling the tank at the surface, and emptying the upper tank "resets" the cooling system. Flores claims his invention maintains the temperature of electronics within the tool below 125 °C in borehole temperatures in excess of 200 °C.

U.S. Pat. No. 5,265,677 to Schultz features a vapor compression refrigeration cooling system to maintain electrical components in a downhole tool within their rated temperature operating range [25]. One embodiment of the cooling system consists of refrigerant, a two chamber container for refrigerant and downhole mud separated by a piston, conduit to distribute refrigerant throughout the system, an expansion valve, an evaporator, and a low pressure dump chamber. Downhole mud pressure forces the container's piston into the liquid refrigerant, thereby pressurizing it. An expansion valve opens and closes in response to input from a temperature sensor adjacent the electronics, and throttles the liquid refrigerant into a liquid/vapor mixture. The evaporator vaporizes the liquid/vapor refrigerant mixture from the expansion valve, and thereby cools the adjoining electronics. Spent refrigerant vapor then flows to the low pressure dump chamber for storage. This embodiment of the cooling system is not reusable once the refrigerant is depleted.

Another embodiment of Schultz's cooling system adds to the system a condenser, two check valves, and a slightly more complicated piston/container assembly with four chambers to recompress and regenerate the refrigerant. The first chamber contains high pressure vapor refrigerant at 345 kPa to 2 MPa (50 to 300 psi). The second chamber contains a pressurized gas, such as nitrogen, at about 7 MPa to 70 MPa (1,000 to 10,000 psi) to match hydrostatic pressures in the well bore. The third chamber contains ports to accept well bore mud. Two movable annular dividers define the fourth chamber, which contains a fluid such as hydraulic oil, and a check valve to separate the fourth chamber into two regions. Pumps on the surface pressurize the well bore mud above hydrostatic pressure, causing the piston to compress both the refrigerant and pressurized nitrogen chambers. The high pressure vapor refrigerant flows through a check valve to the condenser. Rejecting heat to the well bore, the condenser converts the high pressure vapor refrigerant to high pressure liquid refrigerant. The refrigerant then flows to the expansion valve, and other system components to cool the electronics as in the first embodiment. When surface pumping of the well bore mud ceases, the high pressure nitrogen gas in chamber two forces the piston in the opposite direction. As it moves, the piston draws low pressure vapor refrigerant into chamber one from the evaporator through a check valve, resetting the system.

### 1.3.3 Sorption Cooling

U.S. Pat. No. 6,341,498 to DiFoggio presents a sorption cooling system of downhole electronics used in wireline or measurement while drilling applications [9]. The system features a pressure housing, a water supply in close proximity to the electronics, a vapor passage from the electronics, a dewar flask lined with phase change material that shields the electronics and water supply from high well bore temperatures, and a sorbent that adsorbs water vapor and transfers heat through the housing

to the well bore. Heat from the electronics in DiFoggio's invention causes the adjacent water to vaporize. The water vapor rises through a tube, or vapor passage, to a heat sink region within the tool, which is outside the dewar flask. The heat sink region contains a desiccant that adsorbs the water vapor at elevated temperatures. A filter made from porous rock, and located inside the vapor passage, controls the evaporation rate of the liquid adjacent to the electronics, and thereby controls the temperature of the water. Heat transfers from the desiccant to the well bore since it is in efficient thermal contact with the pressure housing. In a preferred embodiment, the volumetric ratio of desiccant to water is approximately 6.25 to 1. Once the water completely evaporates, the system no longer provides cooling, but heating the desiccant to high temperatures regenerates it by releasing the water vapor adsorbed during sorption cooling, and allows for system reuse in subsequent logging runs.

### 1.3.4 Thermal Insulation Techniques

U.S. Pat. No. 6,336,408 to Parrott et al. discloses a method and apparatus for maintaining a component inside a tool at a temperature lower than the surrounding borehole [24]. The invention includes a cylindrical pressure housing, vacuum layer, several reflective and insulating layers, and eutectic phase change material. The vacuum layer and insulating layers reduce heat transfer from the bore hole via conduction and convection, and the reflective layers reduce radiation heat transfer from the surroundings. A eutectic alloy in contact with the internal components acts as a heat sink and absorbs any remaining heat that enters the tool by melting. The commercially available eutectic alloy consists of about 91% tin, 9% zinc, and melts at 199 °C. Parrot et al. claim their invention can maintain the components inside their tool below a temperature of 200 °C for over 100 hours in a 260 °C bore hole. Applications of their invention may include such heat sensitive components as explosives and detonating cords used in a perforating apparatus, or batteries, and other

electronic circuitry.

U.S. Pat. No. 6,220,346 to Gissler describes a novel thermal insulation vessel of downhole electronics that virtually eliminates all conductive heat transfer paths from the environment to an internal cavity through magnetic levitation [12]. Conventional vacuum flasks, though excellent insulators, contain significant paths for conductive heat transfer. Gissler's invention improves on their design by using a plurality of permanent magnets to maintain a gap between an outer housing and an inner housing. The inner housing, or thermal insulation vessel, may further contain an evacuated space as in conventional vacuum flasks, and highly polished surfaces to reduce heat transfer via radiation. Gissler describes several possible magnet arrangements on the inner and outer housings, which maintain their gap with magnetic forces that either repel, or attract, or a combination of the two. Some magnet arrangements allow for easy assembly of the device. In one embodiment, only electrical signal and power wires provide a conductive heat transfer path between the inner and outer housings. In another embodiment, inductive coupling completely eliminates any physical connection between the two housings, and allows power and signal transfer between housings.

U.S. Pat. No. 5,715,895 to Champness et al. relates a dual walled, thermally insulated pipe with low thermal conductivity granules hard-packed into the annulus [6]. The invention provides a means to insulate and distribute drilling fluids chilled by heat exchangers on the surface to a downhole tool. Spherical silica or aluminum oxide beads fill the gap between the inner cylinder and outer cylinder of the pipe, increase the pipe's overall thermal resistance, and oppose high pressure collapse of the annulus. Bead size depends on the downhole pressure a pipe section must withstand, where smaller beads can withstand higher pressures than larger beads. A high pressure inert gas fills the interstitial spaces between beads. The internal pressure of this sealed pipe section increases with temperature and therefore depth, opposing the increasing

well bore pressures of the surrounding fluid. By varying the bead size, the inventors assert one can assemble a drill string of several pipe sections with high pressure pipe at the bottom, and lower pressure pipe at the top, minimizing cost, and maximizing thermal insulation of the chilled drilling fluids.

### 1.3.5 Convection Cooling Cycle

U.S. Pat. No. 5,554,897 to Martin et al. reveals a downhole motor cooling and protection system [18]. The system contains a shroud, two annular chambers, a longitudinal annular baffle, cooling fluid, and a sealed section that encloses the motor. A large shroud separates the cooling fluid from the downhole well fluid, and surrounds the motor, motor housing, longitudinal baffle, and both annular chambers. The longitudinal baffle defines two annular chambers, and strategically placed ports allow fluid communication between the two chambers. As the motor heats up the cooling fluid, it circulates up the inner annular chamber and down the outer annular chamber via natural convection. Since the motor housing is in direct contact with the cooling fluid, the fluid motion enhances heat transfer from the motor to the downhole well fluid outside the shroud. In another embodiment, the motor drives a flow inducer, or pump, that enhances fluid circulation. Vanes or ribs along the inner surface of the shroud increase surface area, and thereby heat transfer.

### 1.3.6 Refrigerant Circulation Cooling

U.S. Pat. No. 4,407,136 to de Kanter features two embodiments of a refrigeration circulation cooling system for use in a downhole oil well logging tool [7]. The first embodiment consists of several printed circuit boards with electronic components, a cylindrical pressure housing, an internal metallic housing, a sump full of liquid refrigerant at the downhole end of the tool, conduits replete with small holes for refrigerant spraying, and a liquid refrigerant pump. The pump, located at the downhole end of the tool, distributes liquid refrigerant to the printed circuit boards via conduits.

These conduits possess several small holes through which the refrigerant sprays onto the printed circuit boards. A thermally conductive coating on each printed circuit board protects electrical components from chemical interaction with the refrigerant. As it vaporizes, the refrigerant cools the surface of this coating, and thereby the electronics. Next, the vapor escapes through openings in the internal metallic housing, and condenses on the inner surface of the pressure housing, eventually dripping down to the sump at the downhole end of the tool for recirculation.

The second embodiment of de Kanter's invention also includes a cylindrical pressure housing, several printed circuit boards covered by a mesh or wick, and features a thermos chamber, heat sink housing containing a eutectic alloy, and refrigerant sump at the downhole end of the tool that immerses the hottest electrical components. These components heat up the refrigerant and eventually vaporize it to some extent. The vapors rise to the heat sink housing and condense on its surface as the eutectic alloy absorbs the heat. Droplets collect and run down to the mesh, which then distributes liquid refrigerant to the upper regions of the printed circuit boards and eventually, the lower sump. At equilibrium, a continuous flow of refrigerant transfers heat from the electrical components to the eutectic alloy via the refrigeration vaporization and condensation process.

### 1.3.7 Evaporative Thermal Protection

U.S. Pat. No. 4,248,298 to Lamers et al. presents an evaporative thermal protection system for cooling electronics in which the working fluid flow path extends from the surface to the downhole tool, and back again [17]. Components located downhole include a thermal protection cartridge, an evaporative working fluid, and an expansion valve. Surface components of the system include a vacuum pump, a working fluid pump, and a cable drum winch unit. A flexible fluidic communication mechanical cable provides electrical and fluidic communication between the surface

and downhole tool. Metal tubes at the core of the mechanical cable serve as the intake and exhaust conduits for the working fluid.

Surface pumps drive high pressure cooling liquid such as water from the surface to the downhole tool via metal conduits in the mechanical cable. The liquid expands to a low pressure liquid/vapor mixture as it passes through an expansion valve. Then, the mixture vaporizes in a coiled tubing evaporator as it absorbs the excess heat from the electronics. This vapor exhausts to the surface via the exhaust conduit in the cable. A surface vacuum pump regulates the pressure in the exhaust conduit to aid evaporation. Lamers et al. claim their system can keep the downhole electronics temperature to less than 190 °C with heat loads of 44 Watts in a well 4,300 m deep, with well bore temperatures between 250 °C and 375 °C, and using an exhaust tube with an outer diameter of less than 0.38 cm.

### 1.3.8 Thermoacoustic Refrigeration

U.S. Pat. No. 5,165,243 to Bennett discloses a compact acoustic refrigeration system for actively cooling electronics in hostile downhole environments [1] [2] . The system consists of an acoustic engine, acoustic refrigerator, resonator, heater, two annular heat pipes, a hot micro heat pipe, a cold micro heat pipe, and a two dewars to provide insulation. A heater assembly provides thermal energy to an acoustic engine. The acoustic engine, fabricated from low thermal conductivity ceramic acoustic plates, generates a standing wave in a selected medium such as helium. An acoustic refrigerator made from fiberglass acoustic plates cooperates with the acoustic engine to produce the standing wave, and consequently a relatively hot end, and relatively cold end. The resonator provides the "acoustic capacity" necessary to maintain the standing wave.

Heat flows from the electronics to the refrigerator's cold end via an annular heat pipe and micro heat pipe assembly. The standing wave within the refrigerator causes

heat to flow “uphill” from the cold end to the hot end of the refrigerator. Another micro heat pipe transfers heat from the hot end of the refrigerator to another annular heat pipe, which rejects this heat to the bore hole. Two Dewars limit heat transfer to/from the surrounding well bore. Bennett claims a particular configuration of the acoustic refrigerator provides about 8 Watts of cooling at the price of 44 Watts, and achieves a minimum electronics temperature of 181 °C in bore hole temperatures as high as 300 °C.

# CHAPTER 2

# DESIGN TARGETS AND OVERALL CONCEPT

## *2.1 Design Targets*

This research effort focuses on the development of a thermal management system for electronics used in wireline logging tools. It begins with an accurate definition of the pertinent operating conditions and design constraints. A list of critical design criteria for the thermal management system was compiled, which includes expected environmental conditions, space constraints, and preferred performance requirements based on current and future business needs. These ambitious design targets, if met, promise to increase the competitive advantage of the research sponsor, *Halliburton Energy Services*, over its competitors, and to open new business markets and opportunities. Table 2.1 itemizes the design targets, constraints, and operating conditions.

## *2.2 Conceptual Design*

An innovative thermal management system was developed to address the design targets outlined above. Three main techniques or approaches describe this system.

**Table 2.1:** Design Targets for Prototype Thermal Management System

1. Maximum downhole time = 24 hours
2. Total power dissipated by electronics = 18 Watts
3. Borehole operating temperature = 200 °C
4. Maximum case temperature of any chip should not exceed 100 °C
5. Max power dissipated by a single chip = 1.5 to 2 Watts
6. Available electrical power = 20 Watts at 200 Volts
7. Entire system must fit within standard 3" diameter vacuum flask

First, the system insulates the sensitive electronic components from the harsh external environment. Second, the system stores the heat dissipated by the electronic components. Third, the system consists of an efficient means to transfer heat from the electronic components to a heat storage medium.

Specifically, a vacuum flask thermally insulates the bulk of the thermal management system, and electronic components. Containing a vacuum between concentric, highly polished walls, the vacuum flask minimizes heat transfer from the environment via conduction, convection, and radiation. However, the vacuum flask keeps heat in as well as it keeps heat out. If the heat cannot be rejected to the environment, then it must be stored.

A phase change material (PCM) provides heat storage for the electronic components and any heat that leaks through the vacuum flask. The PCM stores heat in two ways. First, heat is required to raise the temperature of a PCM to its melting temperature, known as the sensible heating. Second, melting the PCM from solid to liquid requires a significant amount of thermal energy per unit mass of PCM, called the latent heat of fusion [14]. By choosing a PCM with low melting point, and high latent heat of fusion, the electronic components can remain below their maximum temperature rating for extended periods.

However, optimal heat storage requires an efficient thermal path between the electronic components and PCM. A closed coolant flow loop provides this thermal path. The main components of the flow loop include a cold plate, coolant pump, and heat exchanger. Placed in intimate thermal contact with the electronic components, the cold plate transfers heat dissipated by the electronics to a cooling fluid. The pump circulates the coolant through the loop to the heat exchanger, where the heat from the cooling fluid is rejected to the surrounding PCM. Slowly, the PCM will change phase from solid to liquid, storing the heat generated by the electronics. Figure 2.1 shows a conceptual view of the thermal management system packaged into a long,

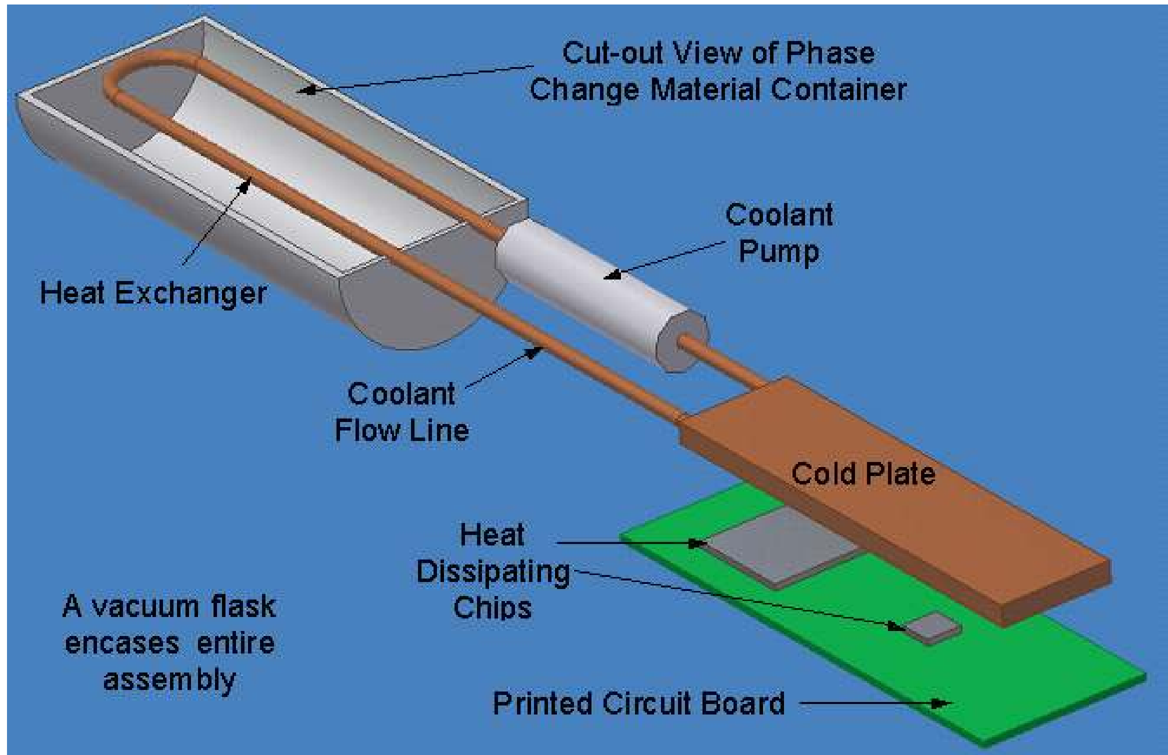


**Figure 2.1:** Overall Concept of Thermal Management System

thin, cylindrical configuration.

## *2.3 Concept-Specific Design Goals*

The selection of an overall concept leads to several concept-specific design goals, which ultimately determine the final design of a prototype. This section lists several concept-specific goals used to design the prototype of the thermal management system. These goals often conflict or compete with one another, a situation common to many design projects.

First, the amount of heat that enters the vacuum flask from the environment should be minimized. In particular, this requires careful design and sealing of the vacuum flask opening and electrical wire feed-through. Any heat that leaks into the vacuum flask necessitates additional amounts of PCM, which increases the overall mass and volume of the thermal management system.

Second, the overall thermal resistance between the electronic components and phase change material should be minimized. A large resistance equates to a high temperature difference between the electronic components and PCM, and a reduction in the overall downhole service time of the electronics. A small temperature difference between the PCM and electronic components maximizes PCM heat storage via latent and sensible heating, thereby maximizing downhole service time.

Third, the pressure drop through the flow loop should be minimized. For a given pumping power, cooling fluid circulates more quickly through a flow loop with low pressure drop than one with a high pressure drop. Faster coolant circulation equates to higher heat transfer rates between the electronic components and the PCM.

Fourth, coolant pumping power should be minimized. At high efficiency operation, most of the electric power supplied to a pump is used to drive the flow. However, a significant fraction dissipates as heat, adding to the heat load on the thermal management system. Higher heat loads on the thermal management system demand greater amounts of PCM.

Fifth, the volume of the heat exchanger should be minimized. This design goal competes with the goal to minimize pressure drop through the flow loop, and thermal resistance between the electronic components and PCM. A low volume heat exchanger maximizes the volume available for PCM. However, a low volume heat exchanger might call for small diameter coolant tubing, which leads to increased pressure drop through the loop, or for short lengths of coolant tubing, which might increase the thermal resistance between the electronic components and PCM.

Finally, the overall size of the thermal management system should be minimized. A low volume thermal management system maximizes the total space available for other components in a wireline logging tool, and helps minimize cost. Table 2.2 summarizes these concept-specific design goals. The next chapter gives a detailed description of the prototype designed with these goals in mind.

**Table 2.2:** Design Goals Specific to Thermal Management Concept

1. Minimize the amount of heat that enters the vacuum flask.
2. Minimize the thermal resistance between the chips and PCM.
3. Minimize the pressure drop through the flow loop.
4. Minimize coolant pumping power.
5. Minimize volume of the heat exchanger.
6. Minimize overall size of thermal management system.

# CHAPTER 3

# DETAILED DESCRIPTION OF PROTOTYPE

## *3.1 Overview of Prototype*

The previous chapter outlined the prototype design targets, the overall concept for the proposed thermal management solution, and some concept-specific design goals. This chapter gives a detailed description of the prototype, and describes the design and manufacturing of thermal test chips used to simulate downhole electronic components. The major components of the prototype system include a vacuum flask, a heat exchanger, phase change material, a phase change material container, an aluminum adapter, two thermocouple probes, a cold-plate, a fluid expansion compensator, and a commercially available pump. Figure 3.1 gives an overall schematic of the prototype, including the flow path of coolant through the flow loop.

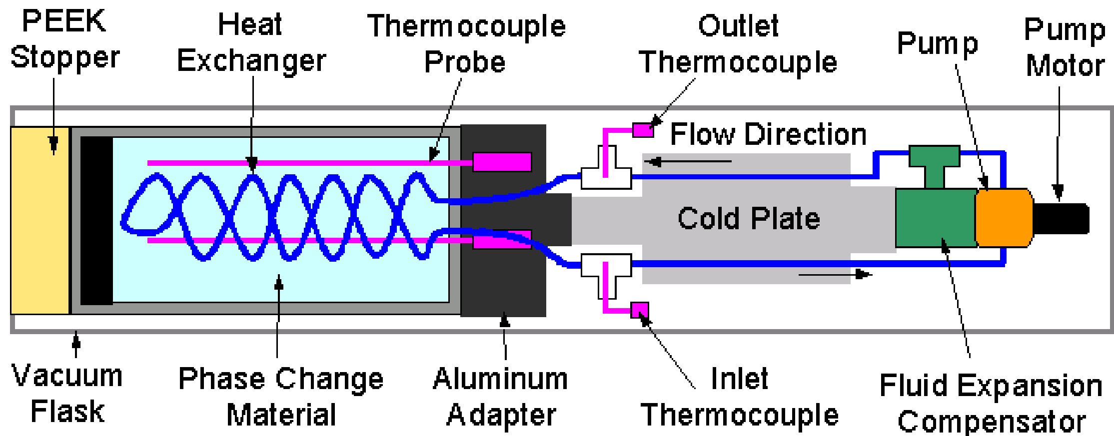


**Figure 3.1:** Overall Schematic of Prototype

**Figure 3.2:** Vacuum Flask Used for Prototype Thermal Management System

## *3.2 Vacuum Flask*

A custom vacuum flask, or dewar, manufactured by *Vacuum Barrier Corporation*, of Woburn, Massachusetts, protects the sensitive electronics from high temperatures. The vacuum flask consists mainly of two concentric, thin-wall, stainless steel tubes, permanently cold-welded at both ends. The annular space between the tubes is evacuated at high temperatures, providing an excellent barrier to heat transfer via conduction and convection. The inner surfaces of the stainless steel tubes possess a highly polished finish that minimizes heat transfer via radiation. A radial spacer maintains concentricity of the two tubes, and allows for thermal expansion. The vacuum flask is 2.362 m (93") long, has a 7.62 cm (3") inner diameter, a 8.48 cm (3.34") outer diameter, and a total internal length of 2.235 m (88"). Figure 3.2 shows the vacuum flask resting on supports on a laboratory table.

A special two piece end cap inserts into the open mouth of the vacuum flask, sealing it from the environment. This end cap consists of a 8.51 cm (3.35") diameter by 8.26 cm (3.25") long stainless steel adapter, and a 7.54 (2.97") diameter by 12.7 cm (5") long PEEK (polyetheretherketone) insulating stopper. The stopper consists of PEEK for two main reasons. First, PEEK possesses an high maximum operating temperature, which exceeds 200 °C. Second, PEEK has a low thermal conductivity. This minimizes the amount of thermal energy that can leak into the flask via the mouth. At one end, the PEEK stopper bolts to the stainless steel adapter, which in turn bolts to the vacuum flask itself. The other end of the PEEK stopper bolts to the heat storage unit. The heat storage unit cantilevers within the vacuum flask

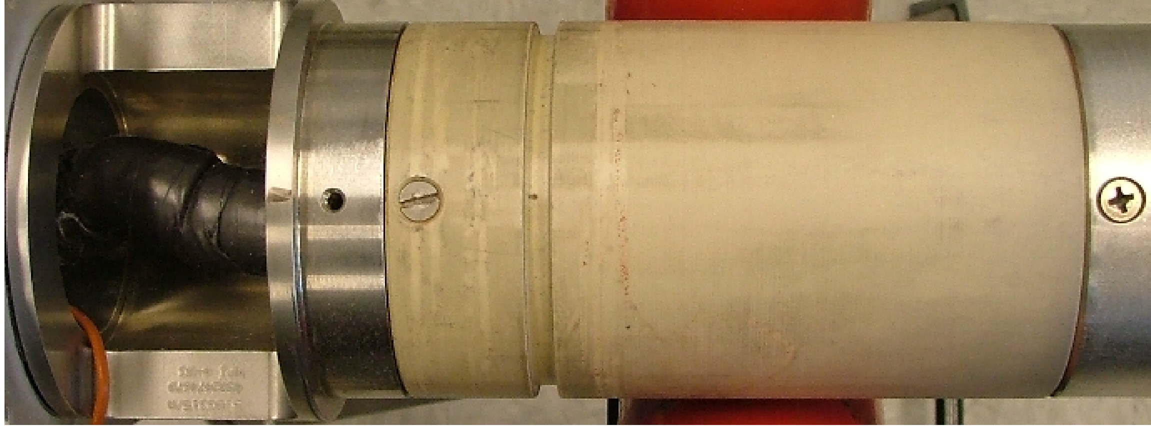

**Figure 3.3:** Vacuum Flask End Cap, PEEK Stopper and Stainless Steel Adapter

from the PEEK stopper.

The two piece end cap also contains a 0.953 cm (3/8") diameter through-hole drilled axially through its center. In practice, this hole allows passage of electrical power and data transmission into the interior of the vacuum flask. For this research, the through-hole serves as a conduit for thermocouples, and DC power to the components within the vacuum flask. Figure 3.3 shows the PEEK stopper connected to the stainless steel adapter on the left, the phase change material container on the right, and wires wrapped in black silicone tape exiting the 0.953 cm (3/8") diameter through-hole. Chapter 6 describes a set of experiments carried out to quantify the thermal insulation performance of the vacuum flask, critical to the design and modelling of the thermal management system.

## *3.3 Phase Change Material*

The choice of phase change material (PCM) is critical to the design of both the heat exchanger and PCM container. Eutectic salts, organic paraffins, and eutectic metal alloys are all examples of PCMs with high latent heats of fusion and low melting temperature [10]. Both eutectic salts and organic paraffins typically possess higher latent heats of fusion than eutectic metal alloys. However, because of their high

**Table 3.1:** Properties of *Cerrobend*

| Melting Point °C | Latent Heat of Fusion kJ/kg | Thermal Conductivity W/m·K | Density Solid kg/m$^3$ | Specific Heat Solid kJ/kg·K | Specific Heat Liquid kJ/kg·K |
|---|---|---|---|---|---|
| 70 | 32.5 | 18.8 | 9580 | 0.146 | 0.184 |

density, eutectic metal alloys have a high latent heat per unit volume. Therefore, consistent with the design goal of minimizing the total volume of the thermal management system, a commercially available eutectic metal alloy was chosen for the first prototype. The particular alloy chosen consists of 50% bismuth, 26.7% lead, 13.3% tin, and 10% cadmium. Also known as *Cerrobend*, or *Indalloy-158*, this PCM has the highest latent heat of fusion of any commercially available eutectic metal alloy with a melting temperature below 125 °C [5]. The high thermal conductivity of *Cerrobend* ensures a low thermal resistance between the electronic components and PCM. Other investigators in this research effort plan to benchmark computer models of the thermal management system against experiments of the first prototype, which uses *Cerrobend* as the PCM. Once validated, these computer models will investigate the use of other PCMs. Table 3.1 summarizes the material and thermal properties of *Cerrobend*.

## *3.4 Phase Change Material Container*

Made entirely from 304 stainless steel, the PCM container holds about 35 kg of *Cerrobend*. A lumped capacitance analysis was used to estimate the amount of phase change material needed for the prototype [16]. Stainless steel was chosen as the material for the PCM container mainly because of its high corrosion resistance. Much like the vacuum flask, the PCM container consists of two concentric stainless steel tubes, each 0.318 cm (1/8") thick, and two 1.27 cm (1/2") thick stainless steel

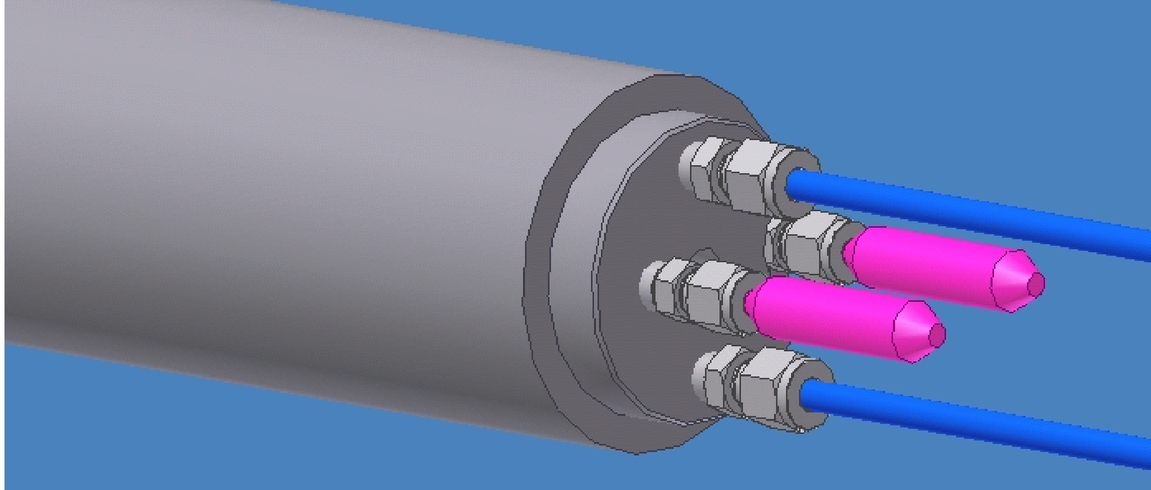

**Figure 3.4:** Close-up CAD Drawing of PCM End Cap and Compression Fittings

end caps. One end cap contains four threaded holes, tapped to accept male 1/8-NPT (National Pipe Thread) fittings. These fittings seal the inlet and outlet heat exchanger tubes, and the two thermocouple probes into place. Figure 3.4 shows a close-up CAD drawing of the PCM container end cap, including the compression fittings, heat exchanger tubes (shown in blue), and thermocouple probes (shown in magenta).

Final assembly of the PCM container consists of several steps. First, the end cap with threaded holes is welded to the concentric tubes. Then, the heat exchanger, and thermocouple probes are installed using bored-through 1/8-MNPT fittings. Next, the PCM is heated and poured into the annular space of the container. To prevent trapping air bubbles or voids in the PCM, each layer is allowed to cool before adding more PCM. Finally, a viton expansion disk is installed, and the remaining end cap is welded into place. The final assembly measures about 1.118 m (44") long, has an outer diameter of about 7.54 cm (2.97"), and an inner diameter of 0.953 cm (3/8"), through which all thermocouples and power lines pass. Figure 3.5 shows a CAD drawing of the PCM container.

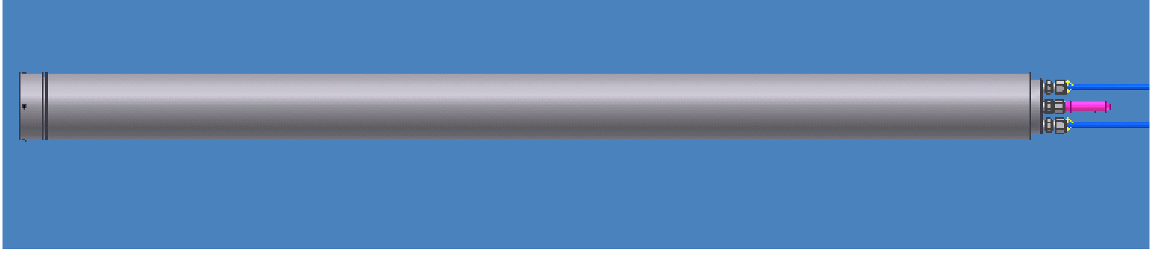

**Figure 3.5:** CAD Drawing of Phase Change Material Container

## *3.5 Expansion Disk*

Much like water, *Cerrobend* is one of the few materials known to expand as it solidifies, and contract as it melts. A viton rubber disk installed at one end within the PCM container annulus ensures the *Cerrobend* solidifies tightly about the heat exchanger. It does this by expanding at high temperatures, keeping a positive pressure on the molten *Cerrobend*. Viton was chosen for the expansion disk material because of its high thermal expansion coefficient, high maximum temperature rating, and because it does not react appreciably with molten *Cerrobend*. Having low thermal conductivity, the expansion disk also provides extra insulation to the PCM from any heat that leaks through the PEEK stopper.

## *3.6 Coiled Tubing Heat Exchanger*

The high thermal conductivity of copper and aluminum make them excellent heat exchanger materials. However, *Cerrobend* reacts with bare aluminum, copper, and brass in the molten state (above 70 °C) and these metals may dissolve into the eutectic, causing it to become sluggish or gritty, and possibly changing its melting temperature [5]. Therefore, the coiled tubing heat exchanger consists entirely of stainless steel.

Specifically, the heat exchanger consists of two coils of seamless 304 stainless steel tubing with a 0.635 cm (1/4") outer diameter and 0.711 mm (0.028") wall thickness. Each coil has a radius of 2.129 cm (0.838"), which is halfway between the inner and

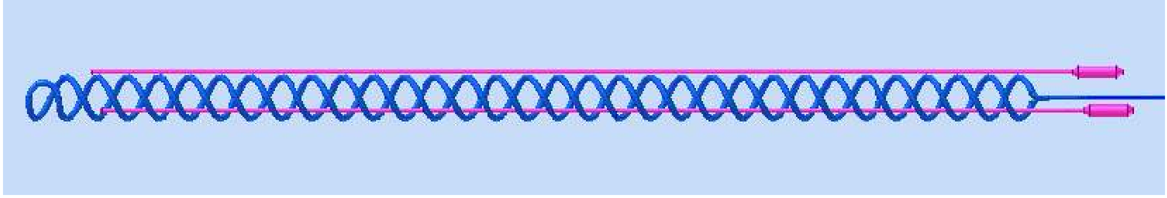

**Figure 3.6:** CAD Drawing of Heat Exchanger and Thermocouple Probes

outer radius of the PCM container, and a 6.35 cm (2.5") coil pitch. The double helix design of the coiled tubing heat exchanger permits an inlet and outlet from the same end of the PCM container. These geometries equate to a total tubing length of about 5 meters. However, the design takes up only 4% of the available volume within the PCM container.

To hasten and simplify fabrication of the prototype, only commercially available diameters of stainless steel tubing were considered for the heat exchanger. Several preliminary design calculations reveal the chosen diameter of coiled tubing represents an excellent compromise between the competing design goals of low pressure drop through the heat exchanger, and minimal heat exchanger volume. From a practical perspective, a large selection of standard, commercially available compression fittings are made especially for 0.635 cm (1/4") outer diameter tubing. This expedites the assembly of the rest of the prototype flow loop. Figure 3.6 shows a CAD drawing of the coiled tubing heat exchanger (shown in blue) and the position of the thermocouple probes (shown in magenta) relative to the heat exchanger. The next section describes these probes in more detail.

## 3.7 Thermocouple Probes

Accurate modelling and characterization of the thermal management system requires knowledge of the temperature distribution within the PCM container over time. Manufactured by *Omega Engineering*, of Stamford, Connecticut, two custom thermocouple probes (Part# OSK/PP10-36-T-316U-40) deliver a robust, compact

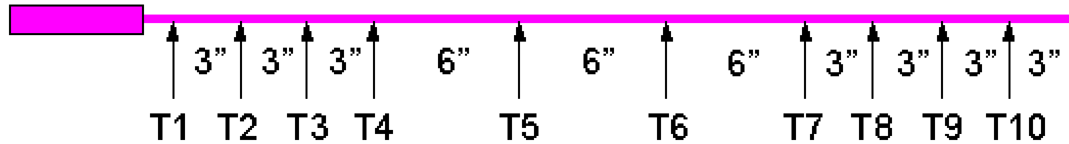


**Figure 3.7:** Schematic of Thermocouple Probe, Thermocouples Spaced as Shown

temperature measurement solution that provides a large amount of information for a minimal number of potential leak paths in the PCM container. Installed at two radial positions, these 1.016 m (40") long temperature probes map both radial and axial temperature distributions within the PCM. Each temperature probe consists of ten type-T thermocouples embedded within a 0.476 cm (3/16") diameter stainless steel sheath. Made from special limits of error wire, these bare thermocouples feature an accuracy of $\pm$ 0.5 °C, and are electrically insulated from one another within the sheath by aluminum oxide. Figure 3.7 shows a schematic of the thermocouple probe, and the spacing of thermocouples within each probe. Close spacing of thermocouples at each end of the probe gives more information in areas where high temperature gradients might occur.

Two bored-through stainless steel 1/8-MNPT compression fittings (*Swagelok* Part# SS-300-1-2BT) swage to the 0.476 cm (3/16") OD thermocouple probes, and thread into the PCM container to provide a reliable, leak-tight seal at high temperatures. It is crucial these fittings consist of stainless steel to match the coefficient of thermal expansion of both the thermocouple probes and the PCM container. At temperatures of only 80 °C to 90 °C, compression fittings made from another material, brass, for example, will expand at a higher rate than the stainless steel sheath of the temperature probes. This difference in thermal expansion provides a leak path through which molten PCM will escape, especially since it is under pressure by the expansion disk.

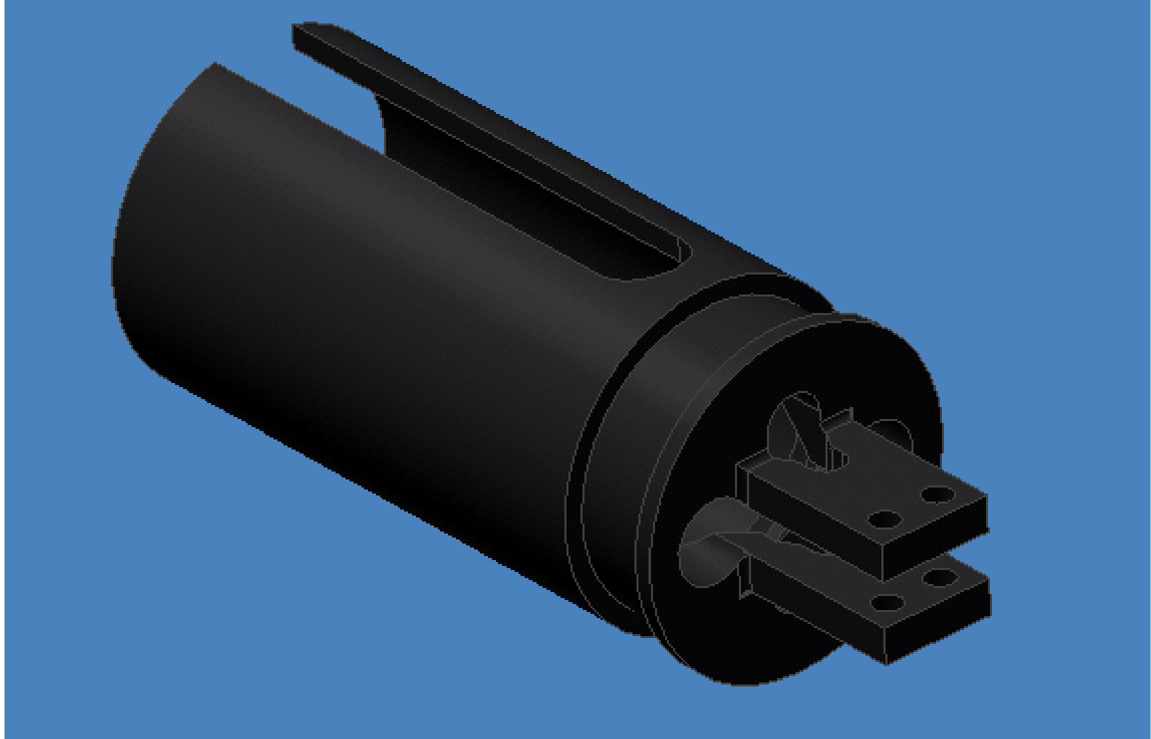

**Figure 3.8:** CAD Drawing of Aluminum Adapter

## *3.8 Aluminum Adapter*

A custom-made aluminum adapter joins the PCM container to the cold plate. One end of the adapter resembles a hollow cylinder, which slides over and shoulders against the PCM container. The other end of the adapter includes a slot with two bolt holes that slides over, and lines up with, bolt holes in the cold plate. Several holes near this slot allow passage of the flow loop tubing, and thermocouple wires. Also, the adapter encloses and protects the thermocouple probe ends and compression fittings. Figure 3.8 shows a CAD drawing of the aluminum adapter.

## *3.9 Cold Plate*

A custom cold plate, manufactured at Georgia Tech, facilitates the transfer of heat dissipated by the electronic components to the cooling fluid, and doubles as a mechanical chassis, or structural support. This combination of functions reduces the

total volume and mass of the thermal management system. The cold plate measures about 38 cm (15") long, 5.72 cm (2.25") wide, 0.953 cm (3/8") thick, and contains two runs of stainless steel tubing through which cooling fluid flows. Assembled on printed circuit boards, thermal test chips mount face-down on two sides of the cold plate. On two sides, the cold plate features rectangular raised "standoffs" that account for the height difference between thermal test chips. Aligned with low height thermal test chips, these standoffs reduce the thermal resistance between the test chips and cold plate. Two aluminum side rails bolt to the cold plate and center the cold-plate within the vacuum flask. One end of the cold plate mates to an aluminum adapter, and the other end connects to a fluid expansion volume. Figure 3.9 shows an exploded CAD drawing of the cold plate, cold plate tubing (shown in blue), side rails, and printed circuit boards (PCBs), to which thermal test chips are soldered (shown in copper).

Fabrication of the cold plate involved several steps. Using a 2-axis CNC milling machine, the overall dimensions of the cold plate, including standoffs, were machined from a single bar of 6061 aluminum 40.64 cm (16") long, 7.62 cm (3") wide, and 1.59 cm (5/8") thick. Then, all necessary bolt and screw holes were drilled and tapped into the cold plate. Next, two slots were machined through the full length of the cold plate using a 0.635 cm (1/4") spherical ball end mill, and their surfaces polished to a smooth finish. Two 0.635 cm (1/4") OD 316 stainless steel tubes were then inserted into these slots from one end of the cold plate. The spherical slots were machined such that the tubing protruded beyond the top surface of the cold plate by only 0.5 mm to 0.75 mm (0.020" to 0.030"). Finally, an arbor press was used to compress the stainless tubing flat and level with the top surface of the cold plate. As the tubing deformed from above, its walls were forced outward into close contact with the highly polished slots in the cold plate. This press-fit greatly reduces the thermal resistance at the interface between the stainless steel tubes and aluminum slots, and produces a strong mechanical connection between the two.

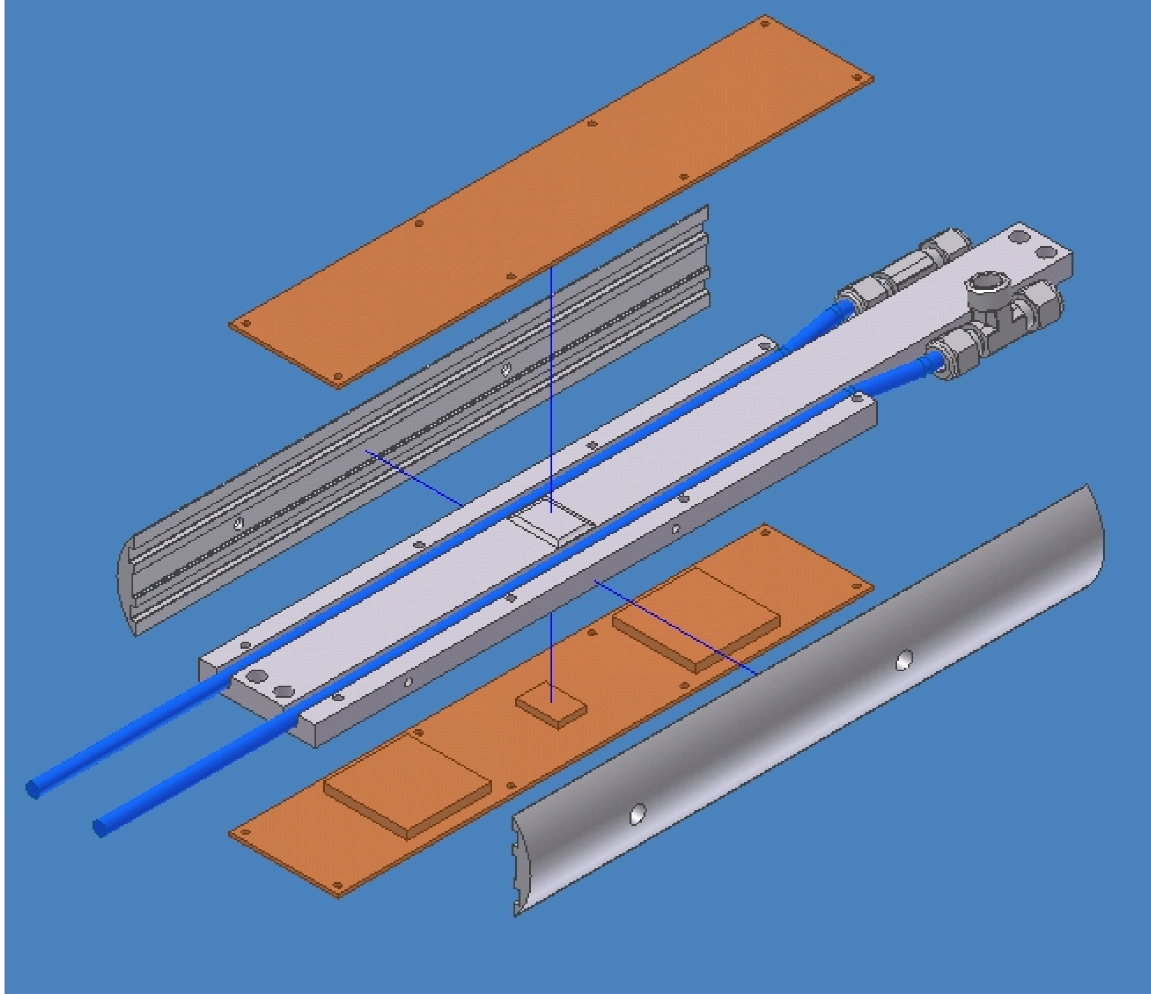

**Figure 3.9:** Exploded CAD Drawing of Cold Plate, Side Rails, and PCBs

## *3.10 Inlet/Outlet Coolant Temperature Measurement*

The inlet and outlet tubing lines of the coiled heat exchanger mate with the two cold plate tubes via two stainless steel tee fittings (*Swagelok* Part# SS-400-3TTF). Manufactured by *Omega Engineering*, two standard thermocouple probes (Part# TMQSS-125G-6) insert into each tee branch to acquire the inlet and outlet temperature of the water as it flows through the heat exchanger. Resembling the thermocouple probes in the PCM container, each 15.24 cm (6") thermocouple probe consists of a type-T thermocouple, made from special limits of error wire, embedded within a 0.318 cm (1/8") diameter stainless steel sheath. A 1/8-MNPT brass plug,

**Figure 3.10:** Close-up of HiTRAN® Matrix Element

wrapped with Teflon tape, seals the branch of each tee fitting. This plug contains a 0.318 cm (1/8") hole drilled through its center, which allows insertion of the thermocouple probe tip into the water flow stream. High temperature epoxy secures the thermocouple probe in place, and completes the fluidic seal of the tee branch. To fit within the vacuum flask, each thermocouple probe bends 90° slightly beyond the epoxy interface.

## *3.11 Tube-Side Heat Transfer Enhancement*

The stainless steel tubing throughout the coiled tubing heat exchanger and cold plate contains a heat transfer enhancement device that improves tube-side heat transfer. Specifically, the temperature management system uses HiTRAN® Matrix Elements manufactured by *Cal Gavin, Inc.* These devices promote coolant fluid mixing by disrupting the laminar flow regime near the inner walls of the coiled heat exchanger tubing and cold plate. Better mixing of the coolant enhances heat transfer from the thermal test chips to the coolant in the cold plate, and from the coolant to the phase change material via the coiled heat exchanger, especially at low coolant flow rates. Made into one meter lengths from three twisted wires, these devices are connected end to end and inserted into the tubing prior to bending it. Since they are highly flexible, they do not significantly impede the tubing from being formed into coils. They consist of stainless steel to provide the best corrosion resistance. Figure 3.10 shows a close-up view of a HiTRAN® Matrix Element.

HiTRAN® Matrix Elements offer three main advantages over a plain-tube configuration. First, enhanced heat transfer reduces the thermal resistance between the electronic components and the PCM. Second, consistent with the design goal of minimizing the total volume and mass of the thermal management system, enhanced heat transfer allows a smaller overall flow loop to be used. Third, lower coolant flow rates made possible through enhanced heat transfer reduce the size and power consumption of the coolant pump. However, the main disadvantage of using these heat transfer enhancement devices is they increase the pressure drop through the flow loop. Chapter 7 describes a set of experiments that seek to quantify the amount of heat transfer enhancement these devices provide.

## *3.12 Coolant Pump*

A suction shoe gear pump (Part# GAT23PFSC), manufactured by *Micropump, Inc.* of Vancouver, Washington, pumps deionized water through the closed flow loop. The pump consists of an entirely sealed stainless steel unit that contains carbon fiber drive gears, a carbon fiber suction shoe, PTFE (polytetrafluoroethylene) static seals, and a driven magnet sealed by a magnetic cup. Connected to a DC electric motor, a driving magnet surrounds the magnetic cup, and couples to the internal driven magnet, which rotates the pump components.

This pump was chosen for several reasons. First, it is a commercially available, off-the-shelf pump. Second, measuring only 3.81 cm (1.5") in diameter, and 12.7 cm (5") long, including the DC electric motor, the pump easily fits within the space constraints of the vacuum flask. Third, as a gear pump, it supplies a nearly constant flow rate at any given shaft speed up to the maximum pressure drop of 517 kPa (75 psi). Fourth, it delivers flow rates from 0 to 450 mL/min. Fifth, the pump features a maximum operating temperature of 177 °C, and a maximum system pressure of 2.41 MPa (350 psi).

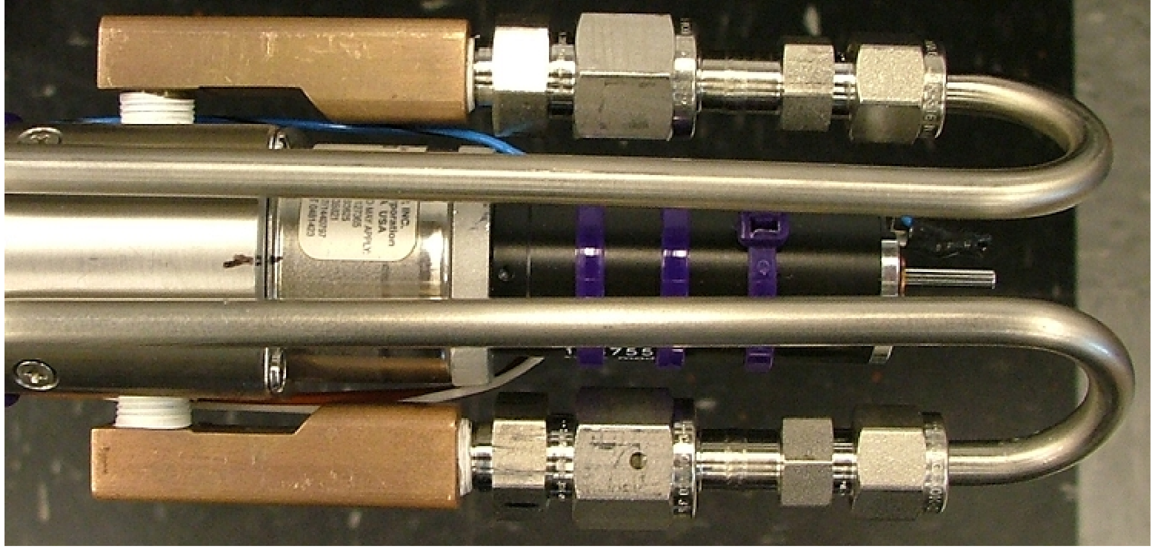

**Figure 3.11:** Top View of Coolant Pump, Pump Motor, and Flow Loop Plumping

Unfortunately, the DC electric motor originally supplied with the gear pump is rated to only 60 °C, ten degrees below the melting temperature of *Cerrobend*. This called for a search for an electric motor capable of higher temperatures. An RE25 DC motor (Part# 118755), from *Maxon Motor Company*, was selected to replace the original motor. This all metal motor features a maximum continuous operating temperature of 125 °C, includes graphite brushes, ball bearings, and high quality rare earth magnets, and possesses an efficiency over 70%. A custom aluminum adapter machined at Georgia Tech joins the new motor to the pump. This pump/motor assembly connects to the fluid expansion compensator with a 304 stainless steel adapter. Figure 3.11 shows the pump and motor, along with fluid lines running to the inlet and outlet of the pump.

## *3.13 Fluid Expansion Compensator*

As the deionized water within the flow loop heats up, it expands. If the flow loop includes no means to compensate for this expansion, pressure rapidly increases within the flow loop, and threatens to violently burst the tubing in a worst-case scenario.

**Figure 3.12:** Top View of Fluid Expansion Compensator and Flow Loop Lines

Therefore, the flow loop contains a fluid expansion compensator. This compensator consists mainly of a hollow, cylindrical 304 stainless steel chamber, which measures 20.32 cm (8") long, has a 3.81 cm (1.5") outer diameter, and contains a 2.54 cm (1") cylinder bore. A piston/spring assembly within the cylinder bore moves in response to the expanding coolant. Above room temperature, the piston applies an equal and opposite force on the expanding water, pressurizing it.

The piston assembly consists of a brass piston backed by a stainless steel spring. Two viton O-rings seal the brass piston to the cylinder bore. The stainless steel chamber contains two openings. One opening allows insertion of the piston/spring assembly into the cylinder bore, and is capped by the stainless steel adapter connected to the pump/motor assembly. A retaining ring butts up against a shoulder just inside this first opening, and grounds one end of the spring within the cylinder bore. The other opening consists of a threaded hole to accept a 1/8-MNPT tee fitting. Water from the flow loop fills one side of the cylinder bore through this tee. The third branch of this tee serves as an evacuation and fill port for the flow loop, described in more detail in the next chapter. Figure 3.12 shows a close-up of the fluid expansion compensator from the top, and stainless steel flow loop plumbing.

## *3.14 Thermal Test Chips*

In order to test the effectiveness of the prototype thermal management system, it is necessary to simulate the heat dissipated by electronic components in a well logging tool. Rather than use actual electronic components, which quickly becomes expensive, several thermal test chips were designed, manufactured and used in prototype tests. These thermal test chips resemble the actual electronic components in two important ways. First, they simulate the heat rate and heat density dissipated by actual well logging electronic components. Second, the electronic packaging of the thermal test chips, including materials and geometry, bears a close similarity to the real components. This ensures the relevant heat transfer paths throughout the chips are taken into account.

Two different thermal test chips were developed, a "big" chip, and a "small" chip. Each consists of a kapton resistive heater from *Minco*, to simulate heat dissipation, and a dummy QFP (quad-flat-pack) component from *Practical Components*, to simulate the packaging of the electronic components. The small chip, 14mm by 20mm, contains a 10 Ohm resistive heater in order to dissipate about 1.5 Watts. The big chip, 40mm by 40mm, contains an 18.3 Ohm resistive heater to dissipate on the order of 4.5 Watts. Each plastic dummy component contains an integral copper heat spreader, and electrical leads on all four sides. Table 3.2 summarizes the important details of each thermal test chip configuration.

*Quik Pak* of San Diego, CA, a company that specializes in reworking electronic packages, fabricated the thermal test chips. For each thermal test chip, they first "opened" the dummy component by carefully removing a portion of the plastic packaging material beneath the chip, stopping at the integral copper heat sink. Next, they attached the resistive heater directly to the copper heat sink using a thermally conductive epoxy. Four gold wire-bonds connect two external package leads to the resistive heater to complete the resistive circuit. Two wire-bonds per lead allow a

**Table 3.2:** Thermal Test Chip Details

| Item | Part# | Manufacturer | Size (mm) |
|---|---|---|---|
| Small chip heater | HK5565R10.OL12A | Minco | 6.4 by 6.4 |
| Big chip heater | HK5578R18.3L12A | Minco | 19.1 by 19.1 |
| Small chip package | A-PQ2-QFP100-14x20mm-.65-3.2 | Practical Components | 14 by 20 |
| Big chip package | A-PQ2-QFP304 -40mm-.5mm-2.6 | Practical Components | 40 by 40 |

greater amount of current to pass through the resulting circuit. Finally, they refilled the cavity with plastic molding compound, sealing the resistive heater within the electronic package. Figure 3.13 shows a cross section of the thermal test chip after final assembly.

For the prototype test, these test chips were soldered to several high temperature polyimide printed circuit boards (PCBs). The PCBs were made at *Halliburton Energy Services* using equivalent materials and manufacturing methods used for actual downhole well logging tools. Each PCB measures 25.4 cm (10") long, 5.08 cm (2") wide, 0.318 cm (1/8") thick, and contains two big chips and one small chip. Two boards (six total thermal test chips) were used to test the prototype thermal management system. These test boards mount to two sides of the cold plate. Type-T thermocouples, sandwiched between the thermal test chips and cold plate, monitor the case temperature of each thermal test chip. An *Agilent* DC power supply powered all six chips via two outputs. The four big chips were connected to a power supply output with a maximum rating of 25 Volts and 1 Amp. The two small chips were connected to a power supply output with a maximum rating of 6 Volts and 5 Amps. Figure 3.14 gives the resulting circuit diagram for the both the big chips and small chips. Figure 3.15 shows two big chips and one small chip soldered to a custom printed circuit board, and typical power dissipations for each.

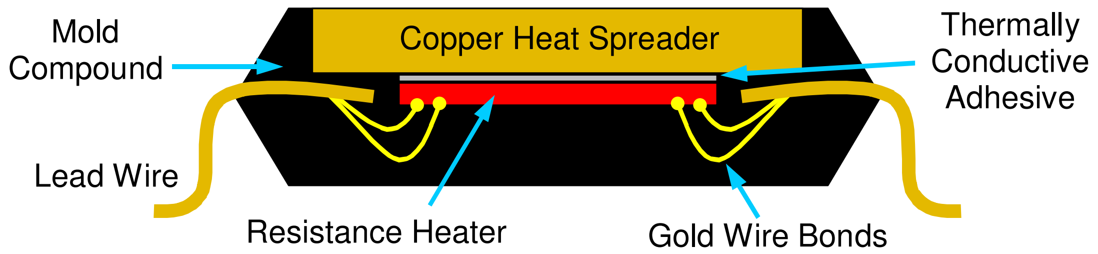


**Figure 3.13:** Schematic of Thermal Test Chip Cross Section

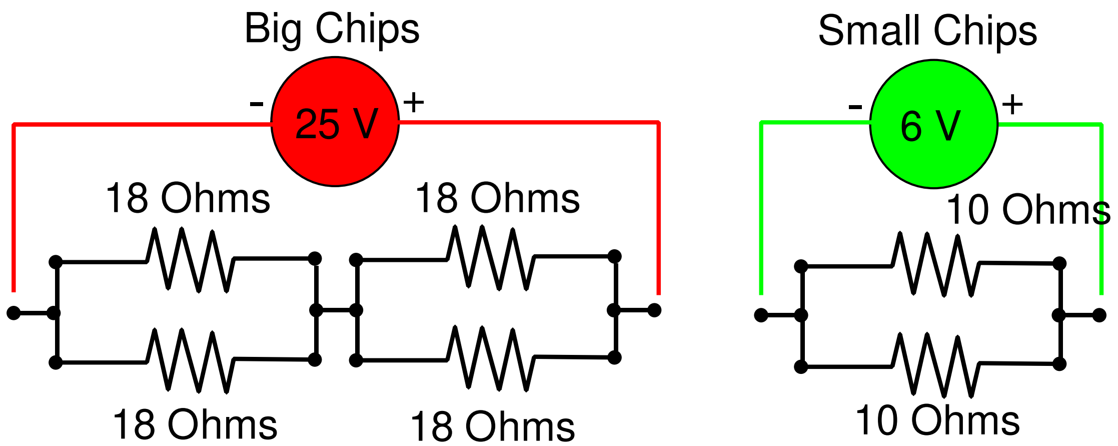


**Figure 3.14:** Circuit Diagram for Big and Small Thermal Test Chips

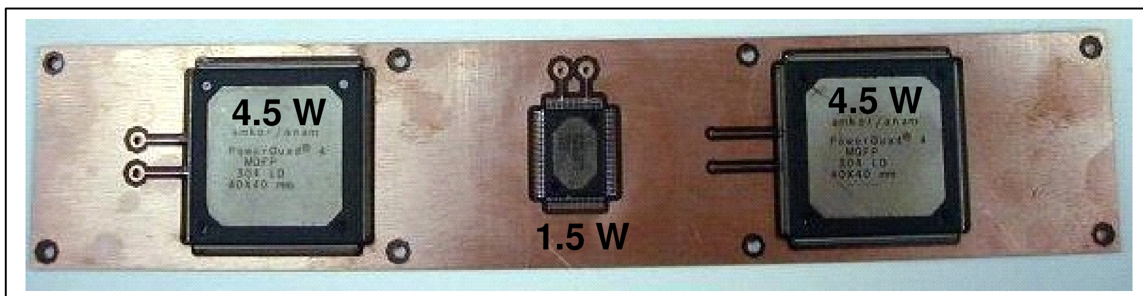


**Figure 3.15:** Thermal Test Chips, Two Big, One Small, Soldered to PCB

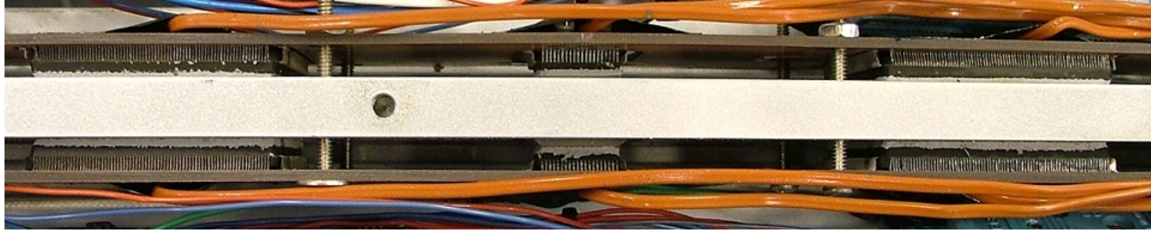

**Figure 3.16:** PCBs Mounted to Cold Plate using Thermal Interface Material

## *3.15 Thermal Interface Material*

Thermal interface material plays a critical role in ensuring low thermal resistance between the thermal test chips and the cold plate. Sarcon® XR-e/XR-He thermal interface material, manufactured by *Fujipoly* of Carteret, New Jersey, fills the gap between each thermal test chip and the cold plate. This gel type thermally conductive silicone rubber features a thermal conductivity of 11 W/m·K, and measures only 1 mm (0.040") thick. Bolted snugly to the cold plate, the thermal test chips compress the highly pliable thermal interface material. This pressure causes the material to fill in any voids at this critical interface, thereby reducing the resistance to heat transfer. Figure 3.16 gives a side view of the PCBs mounted to the cold plate, including light gray thermal interface material between each thermal test chip and the cold plate.

# CHAPTER 4

# PROTOTYPE PERFORMANCE EXPERIMENTS

## *4.1 Purpose*

The main objective of these experiments is to characterize and evaluate the performance of the prototype thermal management system and to compare these results to the design targets originally set. Beyond simply proof-of-concept, these experiments seek to answer the following key performance-related questions: First, how well does the flow loop transfer heat from the thermal test chips to the PCM? Second, how does coolant flow rate affect the length of time the thermal management system can maintain the case temperature of the hottest thermal test chip below 100 °C for a given heat dissipation rate in a 200 °C environment? Third, with a constant flow rate, how long will the hottest thermal test chip remain below 100 °C for different heat dissipation rates? Finally, how will a control system that varies coolant flow rate affect the length of time the thermal test chips remain below 100 °C?

## *4.2 Approach*

To answer the first question, several baseline, or control experiments were carried out. These baseline experiments involved several steps. First, the prototype was inserted into the vacuum flask, and placed in an oven running at 200 °C, which simulates the high temperature environment of a subterranean borehole. Then, with zero coolant flow rate through the flow loop (i.e. no power to the pump), the thermal test chips were powered to 18 Watts. Next, the temperatures of the thermal test chips, and phase change material were monitored and recorded until the highest chip temperature reached 100 °C.

In essence, the baseline experiments mimic a common industry approach to thermal management of electronics in wireline logging tools. In this "state-of-the-art" approach, the electronic components and phase change material are placed together within a vacuum flask. However, conduction alone serves as the primary heat transfer mechanism between the electronic components and phase change material [20]. By comparing these baseline tests, with the pump off, to tests in which the pump is on, one can assess the amount of enhanced performance realized by the prototype over the conduction-only scheme. Specifically, the extra time the thermal test chips remain below 100 °C gives a quantitative measure of enhanced performance.

To answer the second question of interest, whether flow rate influences the total time the thermal test chips remain below 100 °C, several constant chip power experiments were carried out at different flow rates. These tests start out exactly the same as the baseline tests. The tests chips are powered to 18 Watts, the oven runs at 200 °C, and all temperatures are recorded until the highest chip temperature surpasses 100 °C. However, coolant flows through the flow loop at a constant flow rate during these tests. If any optimal flow rate through the flow loop exists, one can determine it by comparing the total length of time the hottest thermal test chip remains below 100 °C for different flow rates.

Several tests with varying thermal test chip heat dissipation at a constant flow rate and oven temperature of 200 °C address the third key question. These experiments were carried out for several heat dissipation rates. These data give valuable information to designers of well logging tools, well logging electronics, and to other members of our research effort modelling the entire thermal management system.

Finally, a proportional control system that monitors the highest chip case temperature, and varies the coolant flow rate by varying the voltage to the pump was written using LabVIEW$^{TM}$. Using this program, and monitoring the temperatures of the thermal test chips, and phase change material, one can determine if a flow rate

control system enhances performance of the thermal management system appreciably. The goal of these experiments is to determine whether an actual field unit will benefit from using a coolant flow control system, or whether a predetermined constant flow rate will suffice. In the first case, a control system is more complicated and expensive to use than a constant flow rate system. However, significant performance increases from a simple control system may warrant the added investment and complexity.

## *4.3 Apparatus and Procedure*

### 4.3.1 Evacuation and Fill Station

The baseline experiments, constant chip power experiments, constant flow rate experiments, and variable control system experiments all require a coolant-filled flow loop prior to testing. Therefore, a reliable, highly repeatable evacuation and fill station was designed and built to charge the flow loop with water. This station virtually eliminates the possibility of trapped air within the flow loop lines, consistent with the design goal of minimizing the thermal resistance between the thermal test chips and PCM.

The evacuation and fill station consists mainly of a three way valve, ball valve, vacuum pressure gauge, graduated cylinder, stainless steel tubing and fittings, vinyl tubes, a two micron filter, and a vacuum pump. The common branch of the three way valve mates with the evacuation/fill tee threaded to the fluid expansion compensator via stainless steel tubing. The other end of this tee connects to tubing on the outlet side of the coolant pump in order to avoid applying a positive differential pressure across the pump inlet, which could jar the suction shoe loose, rendering the pump inoperable. In one position, the three way valve connects to a run that consists of the vacuum pressure gauge, ball valve, and vacuum pump. This position is used to evacuate the flow loop. In the other position, the three way valve leads to the two micron filter, vinyl tubing, and ultimately, deionized water in a graduated cylinder.

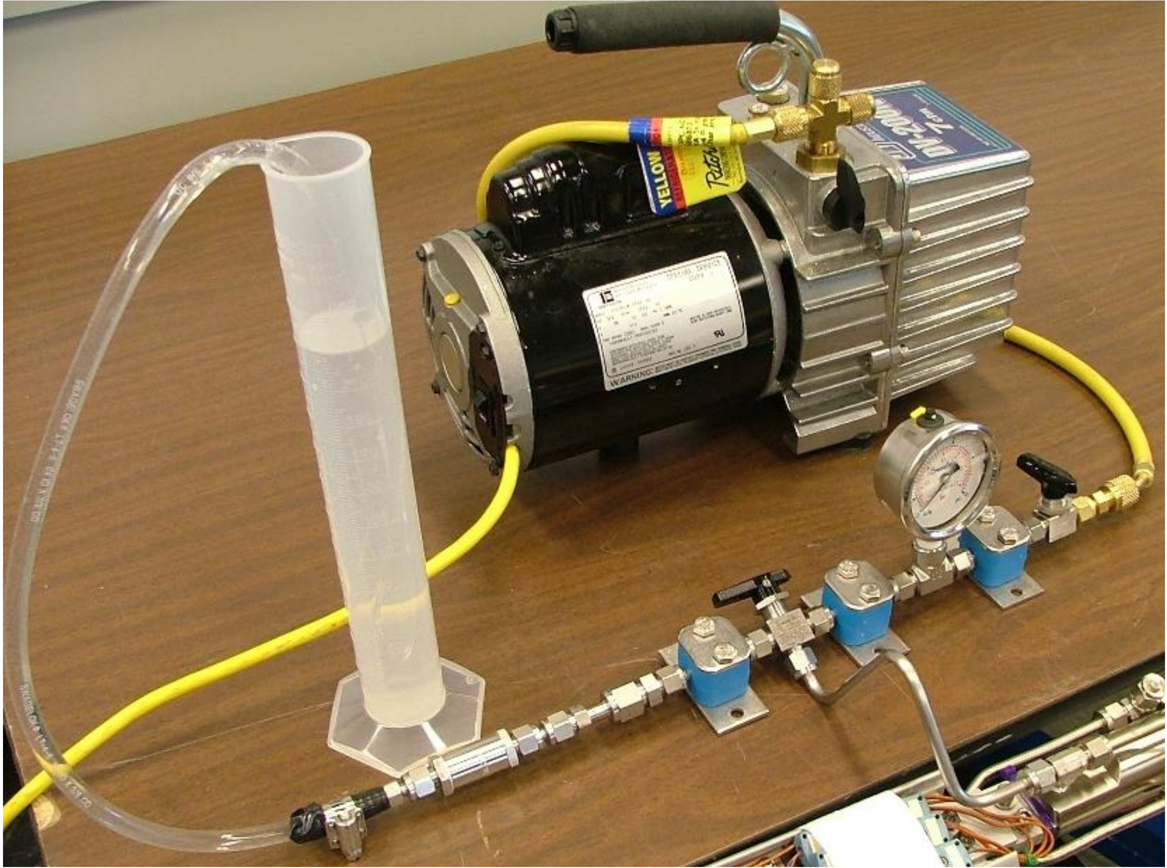


**Figure 4.1:** Close-up of Evacuation and Fill Station

This position is used to fill the flow loop. Figure 4.1 shows a close-up of the evacuation and fill station.

The evacuation and fill procedure for the prototype flow loop involves several steps. First, since the vacuum pump contains no liquid trap, the flow loop and evacuation and fill station must be dried out completely using compressed air prior to connecting it to the vacuum pump. Once all sign of moisture is removed from the flow loop, the flow loop is completely reassembled. Then, the three way valve is turned to the fill position and the graduated cylinder is filled with deionized water. After inserting the dry, empty vinyl tubing into the graduated cylinder, the vacuum tubing is attached to another run of vinyl tubing swaged to the common branch of the three way valve. Turning the vacuum pump on draws water from the graduated

cylinder through the filter and three way valve. Once water is seen to pass through the three way valve and into the vinyl tubing to which the vacuum pump is connected, the vacuum pump is turned off. At this point, the entire run of vinyl tubing from the graduated cylinder to the three way valve should be full of water, and free of bubbles. Next, the three way valve is switched to the evacuation position, which seals off the fill position.

Evacuation of the flow loop begins soon after the common branch of the three way valve is swaged to the evacuation/fill tee on the fluid expansion compensator. Then, the vacuum pump line is threaded to an AN-adapter, which is swaged to the ball valve. At this point, there is a completely sealed flow line that extends from the evacuation/fill tee of the flow loop to the vacuum pump. The ball valve is opened, the vacuum pump switched on, and the flow loop begins to evacuate. Evacuation continues until the vacuum pressure gauge reads –99.8 kPa (-29.5 in Hg), the maximum vacuum provided by the vacuum pump. Next, the ball valve is closed to trap the vacuum within the flow loop, and the vacuum pump is switched off. Any changes in the pressure gauge reading indicate a leak. Then, the graduated cylinder is filled with deionized water to the 250 mL mark.

Finally, the three way valve is turned back to the fill position, causing fluid from the graduated cylinder to rush into the evacuated flow loop. The flow loop fills with water until the water level in the graduated cylinder no longer changes. Then, the stainless steel line is removed from the evacuation/fill tee, and a cap is carefully swaged in its place. The fluid level drop in the graduated cylinder indicates the total internal volume of the flow loop, which is about 150 mL. Figure 4.2 shows the prototype thermal management system connected to the evacuation and fill station prior to filling the flow loop with water. Table 4.1 summarizes the apparatus used to evacuate and fill the prototype flow loop with water.

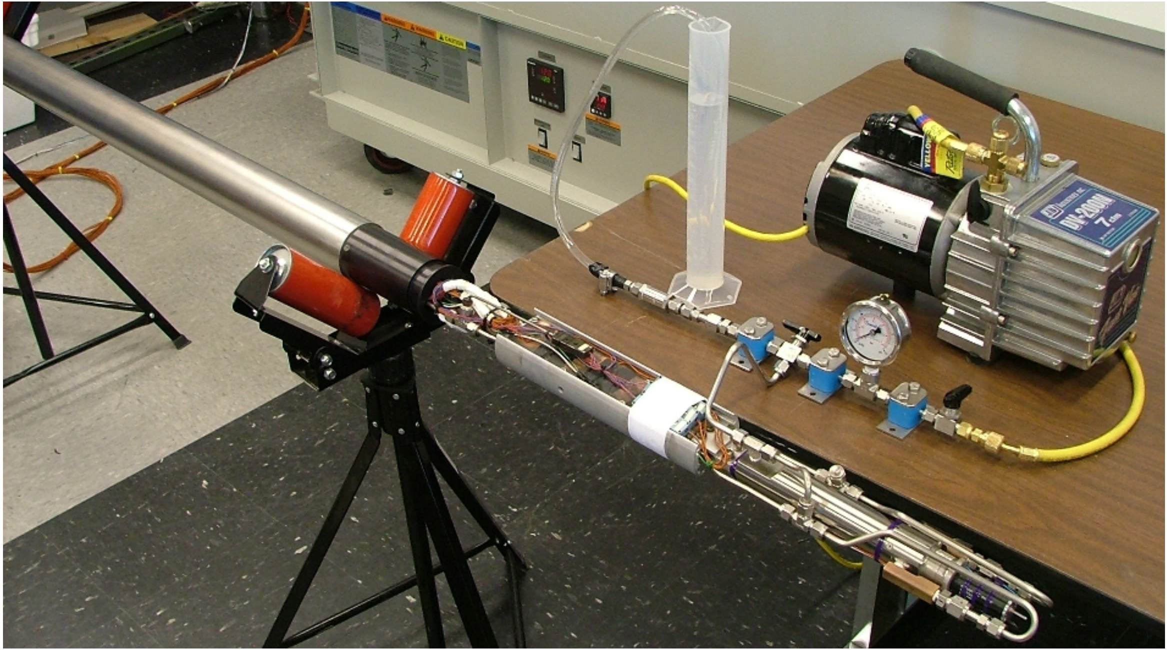

**Figure 4.2:** Prototype Connected to Evacuation and Fill Station

**Table 4.1:** Apparatus Used in Evacuation and Fill Station for Prototype

| ITEM | DESCRIPTION |
|---|---|
| Pressure Guage | Swagelok, Part# PGI-63C-PC30-LAOX |
| 316 Stainless tube | Swagelok, 1/4" OD, 0.035" wall thickness |
| 316 Stainless tee | Swagelok, 1/4- FNPT, Part# SS-400-4TTF |
| 3-way valve | Swagelok, Part# SS-42XS4 |
| Ball valve | Swagelok, Part# SS-42S4 |
| 2 Micron filter | Swagelok, Part# SS-4F-2 |
| Feed Hose | Swagelok, 3/8" OD, Vinyl, Part# LT-4-6 |
| AN-adapter | Swagelok, Part# B-4-TA-1-4AN |
| Tube Support Kit | Swagelok, Part# 304-S1-PP-4T |
| 250 mL Grad. Cylinder | McMaster-Carr, Part# 1475T14 |
| 2-stage Vacuum Pump | JB-Industries, Model DV-200N, Serial#1200 |
| 1/4" OD Charging Hose | Ritchie Engineering, Co., SN#P187OB |

### 4.3.2 Leak Test

The evacuation and fill station also provides the apparatus and opportunity needed to perform a leak test on the flow loop. A leak test ensures the prototype flow loop contains no gross leaks, which is critical both for safety reasons and to prevent damage to the prototype during testing. By evacuating the flow loop, and monitoring the change in vacuum pressure over time, one can test for gross leaks in the flow loop. Slow air leaks will cause the pressure gauge reading to change gradually from high vacuum to lower vacuum. Gross leaks will cause the pressure gauge to return to atmospheric pressure quickly, or, if the vacuum pump is turned on, the pressure within the flow loop will never reach a high vacuum. Though no system is perfectly leak tight, if the vacuum pressure does not change appreciably over a 24 hour period, then the flow loop can be assumed leak tight for the prototype tests. Since the evacuation and fill procedure requires making and breaking several plumbing connections, a leak test was performed on the flow loop whenever it was evacuated prior to filling it with water. Leaks, if present, were usually caused by improperly turned-up compression fittings, and remedied by tightening these connections.

### 4.3.3 Oven

A custom made, top-loading, forced convection oven simulates the high borehole temperatures for the prototype tests. Custom manufactured by *Despatch Industries*, the 12 kW electric oven measures 3.5 m (138") wide, 0.66 m (26") deep, and 0.89 m (35") high, and contains a work chamber 3.43 m (134") wide, 0.2 m (8") deep, and 0.15 m (6") high. It was specially constructed to the maximum size that would fit in the freight elevator used to carry it to its laboratory home on the third floor. The oven features a maximum operating temperature of 260 °C, and a 375 Watt horizontal airflow recirculating motor maintains a consistent and uniform temperature throughout the work chamber.

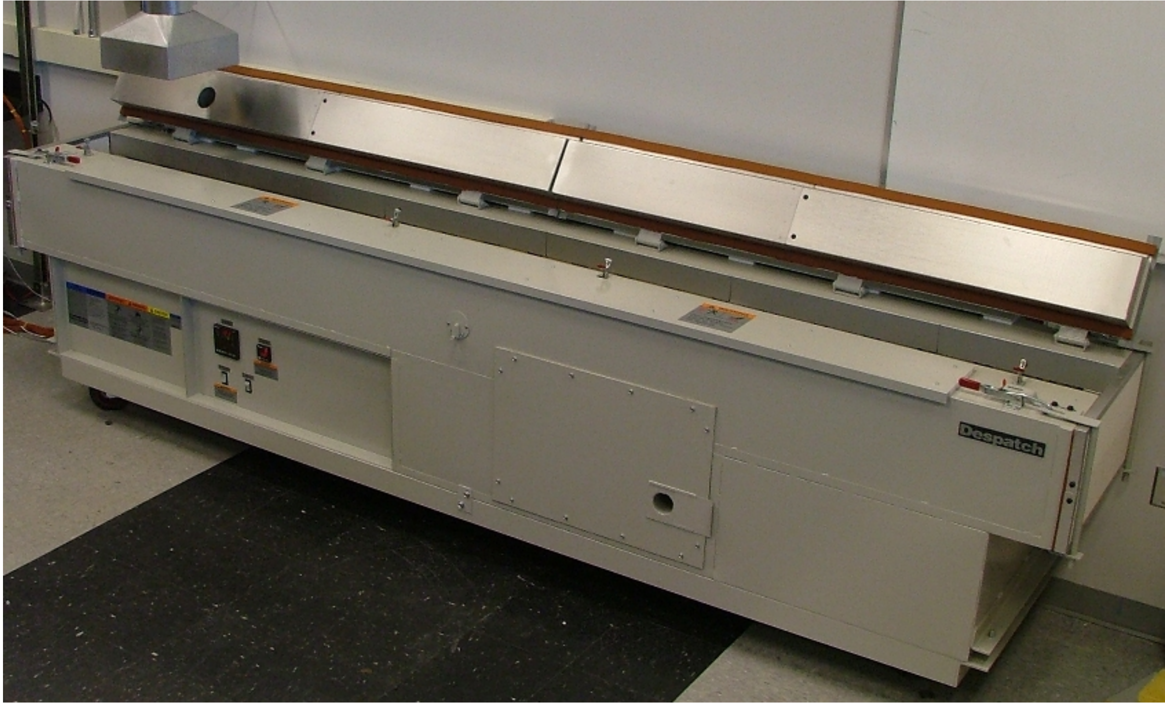


**Figure 4.3:** Oven Used in Prototype Performance Tests

A programmable, microprocessor-based temperature control unit with digital readout delivers PID (Proportional Integral Derivative) control of the temperature within the oven to an accuracy of ± 1/4 % of reading. Another solid-state backup controller provides over-temperature protection. The oven features mild steel, fully reinforced construction with 7.62 cm (3") of high grade insulation surrounding the work chamber to minimize heat losses. The doors and oven front contain an additional inch of insulation. Two easily machinable marinite end caps on each end of the oven allow multiple ovens to be placed end-to-end. To allow access of power and data wires into the oven's work chamber, a feed-through hole was drilled into one of these end caps. Figure 4.3 shows the oven with its top-loading doors open.

### 4.3.4 Initial Setup and Tear Down

All four sets of prototype experiments required the same initial set up before a test, and tear down at the conclusion of a test. The differences in these tests

**Figure 4.4:** Fully Assembled Tool Resting on Table Prior to Test

involve only variables such as flow rate, and thermal test chip dissipation. This section focuses on the initial setup and tear down procedure used for each test after a successful evacuation and fill of the flow was completed.

First, a standard hydraulic automobile engine hoist, engine leveler, and nylon tow straps were used to raise and support the entire prototype. Then the prototype was carefully inserted into the mouth of the vacuum flask, followed by the PEEK end cap. Since the resulting prototype/vacuum flask assembly experiences no adverse mechanical loads, vibration, or shock during these tests, it was not necessary to bolt the vacuum flask directly to the stainless steel adapter of the end cap. For all tests, either an O-ring around the PEEK stopper, or several wraps of high temperature silicone tape around the vacuum flask mouth provided an air-tight seal. Figure 4.4 shows the completely assembled tool resting on supports on a laboratory table, including thermocouple and power lines protruding from one end.

Next, the tow straps were carefully wrapped around the vacuum flask, which was usually held up off the surface of the laboratory table using metal supports, and the entire "tool" was lifted using the engine hoist and leveler. Then, the engine hoist was rolled to the oven, and the tool positioned over the open mouth of the oven.

Prior to lowering the tool into the oven, the top marinite end cap on one end was removed. Next, the tool was lowered onto four steel supports that keep it raised and centered within the work chamber of the oven. These supports each have a strip of high temperature silicone insulation that cushions the tool, and prevents it from rolling off the supports. Figure 4.5 shows a view of the engine hoist, leveler, and tow straps lowering the tool into the oven. Figure 4.6 shows the tool resting on supports within the oven work chamber.

Then, the bundled thermocouples and power lines running from the data acquisition system to the tool were positioned within a slot machined in the lower marinite end cap. Next the top marinite end cap was put back into position above the lower marinite end cap, and clamped into place. This clamping action forces the two marinite end caps together, and compresses the silicone insulation surrounding the feed-through wires, thereby minimizing heat loss from the oven. Then, the tow straps were removed from tool, the hoist backed away from the oven, and the oven's top-loading doors were closed and clamped shut. Figure 4.7 shows a close-up view of the marinite end caps, with the feed-through wires protruding from a slot in the bottom marinite end cap.

Next, data acquisition and control for each test began. The next section gives a complete description of the data acquisition hardware and software used for all four sets of prototype performance experiments. The Results and Discussion section of this chapter gives a complete description of the operating parameters for each test, and results for each test. Having switched on data acquisition, the oven was turned on and set to 200 °C, which it usually reached within a matter of minutes.

The tear down stage for each experiment begins at the conclusion of each test. The oven doors were opened to let the tool cool, and the oven heater turned off. To prevent damage to the oven, the recirculating fan was left on until the work chamber temperature dropped below 100 °C, as suggested by the manufacturer. Next, the

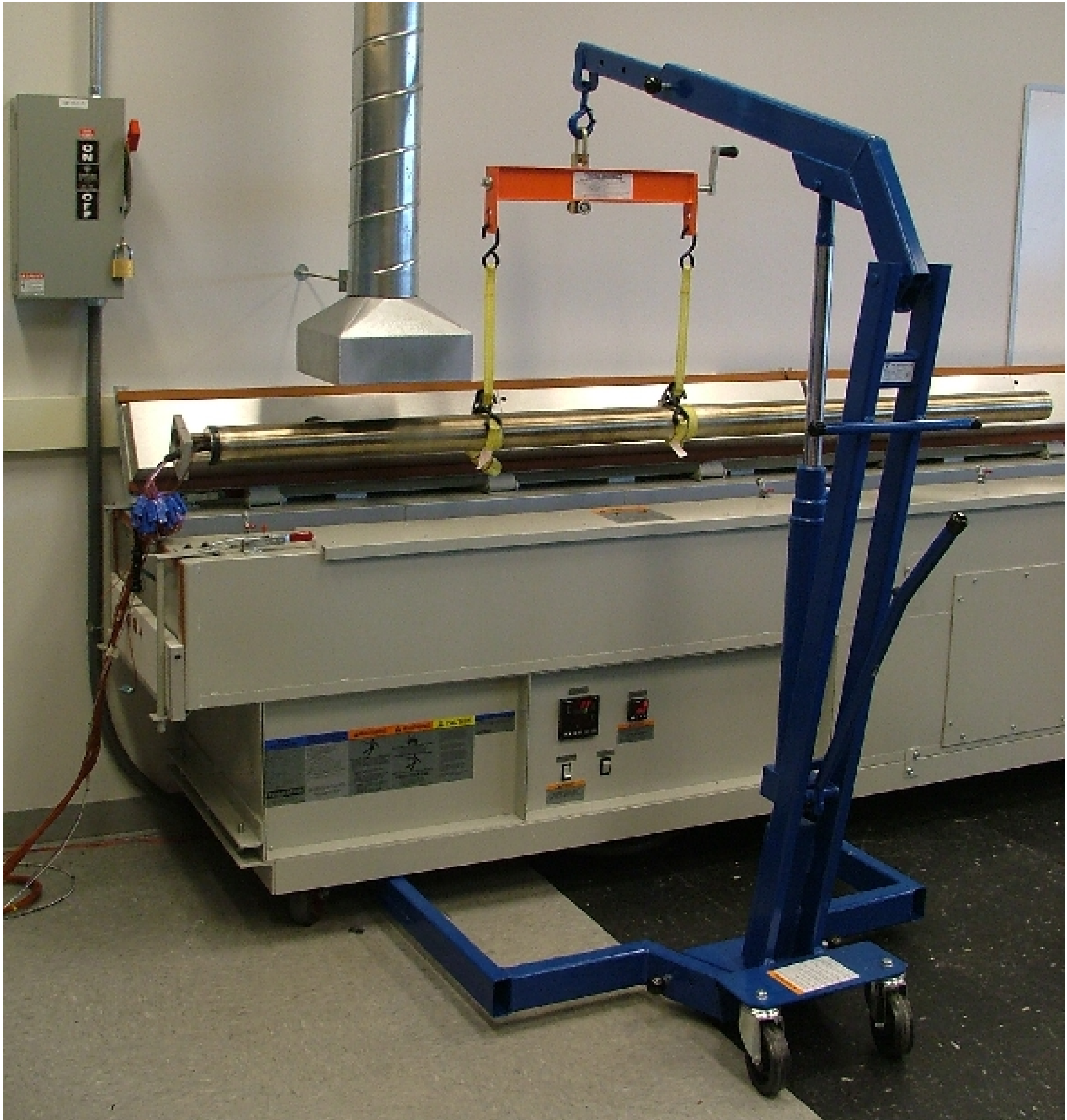

**Figure 4.5:** Tool Lowered into Oven Using Hoist, Leveller, and Tow Straps

**Figure 4.6:** Protoype Tool Resting in Work Chamber of Oven

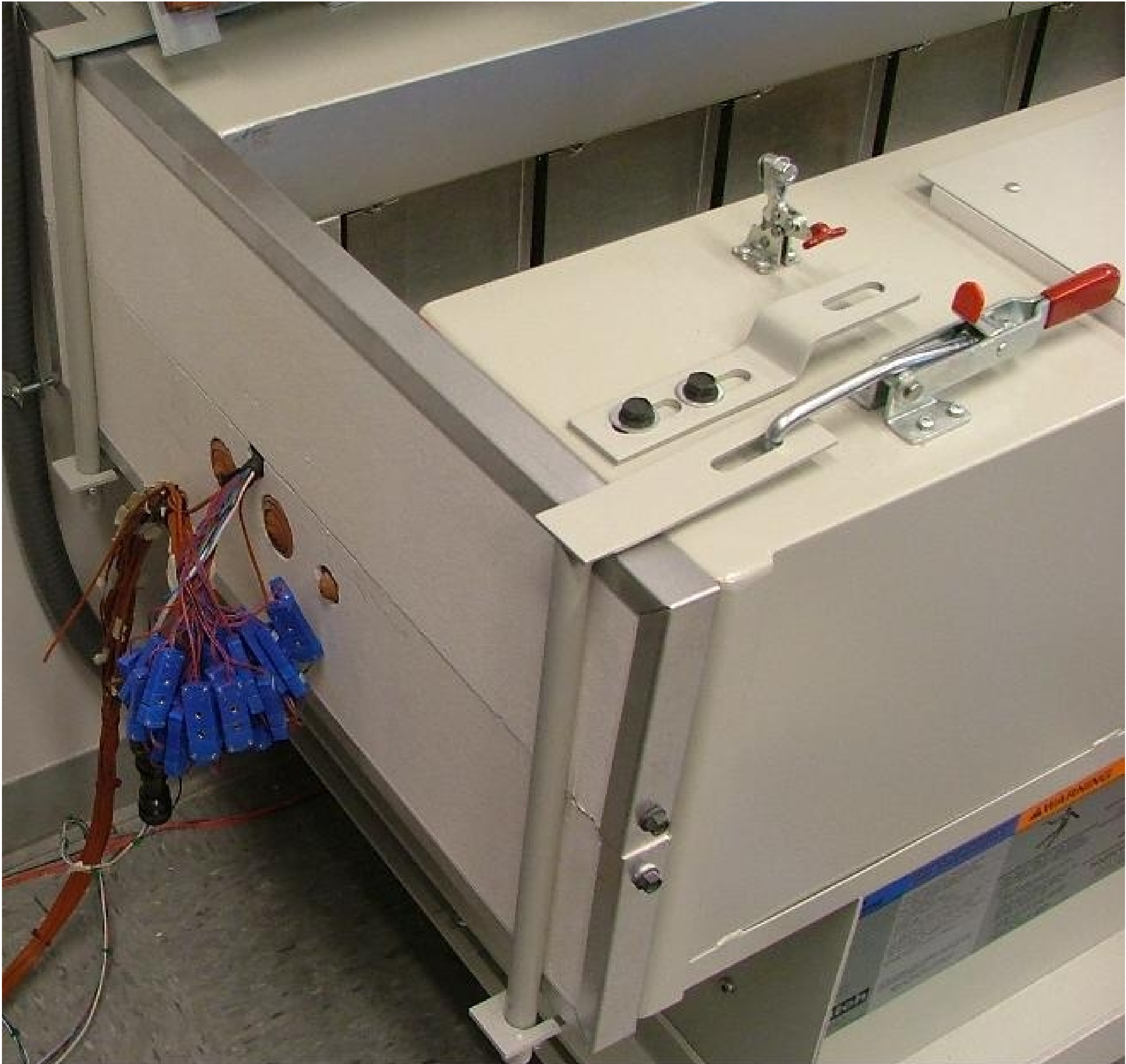

**Figure 4.7:** Close-up View of Marinite End Caps and Feed-through Wires

top marinite end cap was unclamped from the oven and set aside. Once the tool was cool enough to handle, the two nylon straps were wrapped around it, and it was lifted from the oven using the hydraulic engine hoist and leveler. Then, the tool was rolled to a nearby laboratory table, and lowered onto supports. After removing the tow straps from the tool, the prototype was first manually removed part way from the vacuum flask. Next, the protruding PCM container was strapped to the engine hoist and leveler to support its weight as it was completely removed from the vacuum flask. Finally, the hot prototype was placed on roller stands to allow it to cool to room temperature.

## *4.4 Data Acquisition*

### 4.4.1 Hardware

The data acquisition (DAQ) hardware used for all four sets of experiments consists of an *Agilent* 34970A data acquisition/switch unit, an *Agilent* E3631A DC power supply, two *Agilent* 34901A armature multiplexer plug-in cards, two standard GPIB (general purpose interface bus) cables, a GPIB PCI (peripheral component interconnect) card, and a *Dell* desktop computer. Figure 4.8 gives a schematic that shows the physical connections for the data acquisition hardware of this experiment.

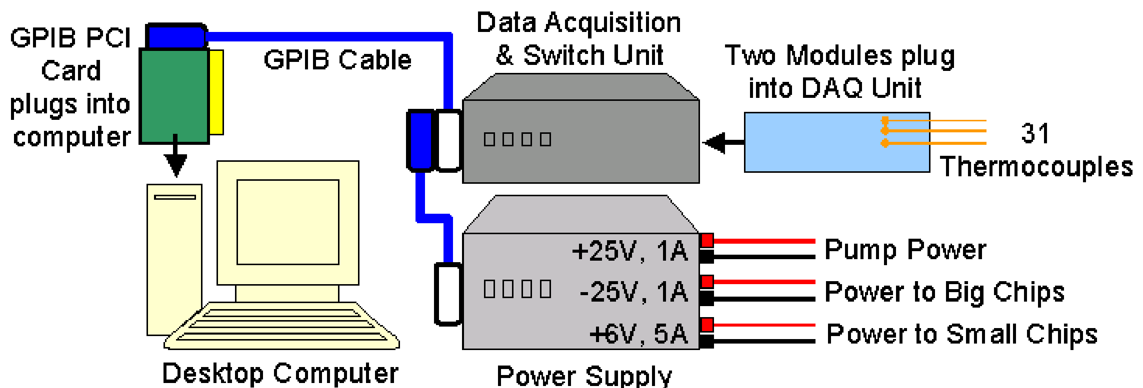


**Figure 4.8:** Schematic of DAQ Hardware Used in Prototype Experiments

The 34970A data acquisition/switch unit features a built-in 6 1/2 digit (22 bit) resolution digital multimeter, and measures eleven functions, such as DC voltage, DC current, and thermocouples without the need for external signal conditioning. It contains slots to accept up to three module plug-in cards, for up to sixty channels of data, and includes a built-in GPIB interface. The *Agilent* E3631A DC power supply features three outputs: +6 Volts, 5 Amps; +25 Volts, 1 Amp; and -25 Volts, 1 Amp. As mentioned in the previous chapter, the +6 Volt output powered the small thermal test chips, -25 Volt output powered the big thermal test chips, and the +25 Volt output was used to power the pump. Both the data acquisition/switch unit and the power supply communicate with the desktop computer via GPIB. Figure 4.9 shows a front view of the data acquisition/switch unit and power supply.

One of eight different plug-in modules made for the 34970A, the 34901A multiplexer module consists of twenty-two total channels, scan rates of up to sixty channels per second, and a built-in thermocouple reference junction. All thirty-one thermocouples used in the prototype performance tests were directly wired to screw terminals 101 - 211 on the 34901A multiplexer modules, and scanned by the 34970A data acquisition/switch unit at ten second intervals for all four sets of prototype tests. Figure 4.10 shows several thermocouples wired to an 34901A multiplexer module.

### 4.4.2 Software

A custom data acquisition and control program was written for the prototype performance experiments using LabVIEW™ 7 Express software from *National Instruments*. This LabVIEW™ program, called *Main Temp Logger* communicates with the *Agilent* 34970A data acquisition/switch unit to monitor and acquire all measurements. The program also provides for automatic and manual control of the *Agilent* E3631A DC power supply via GPIB, which controls the power supplied to the big chips, small chips, and flow loop pump. The user interface provides real-time

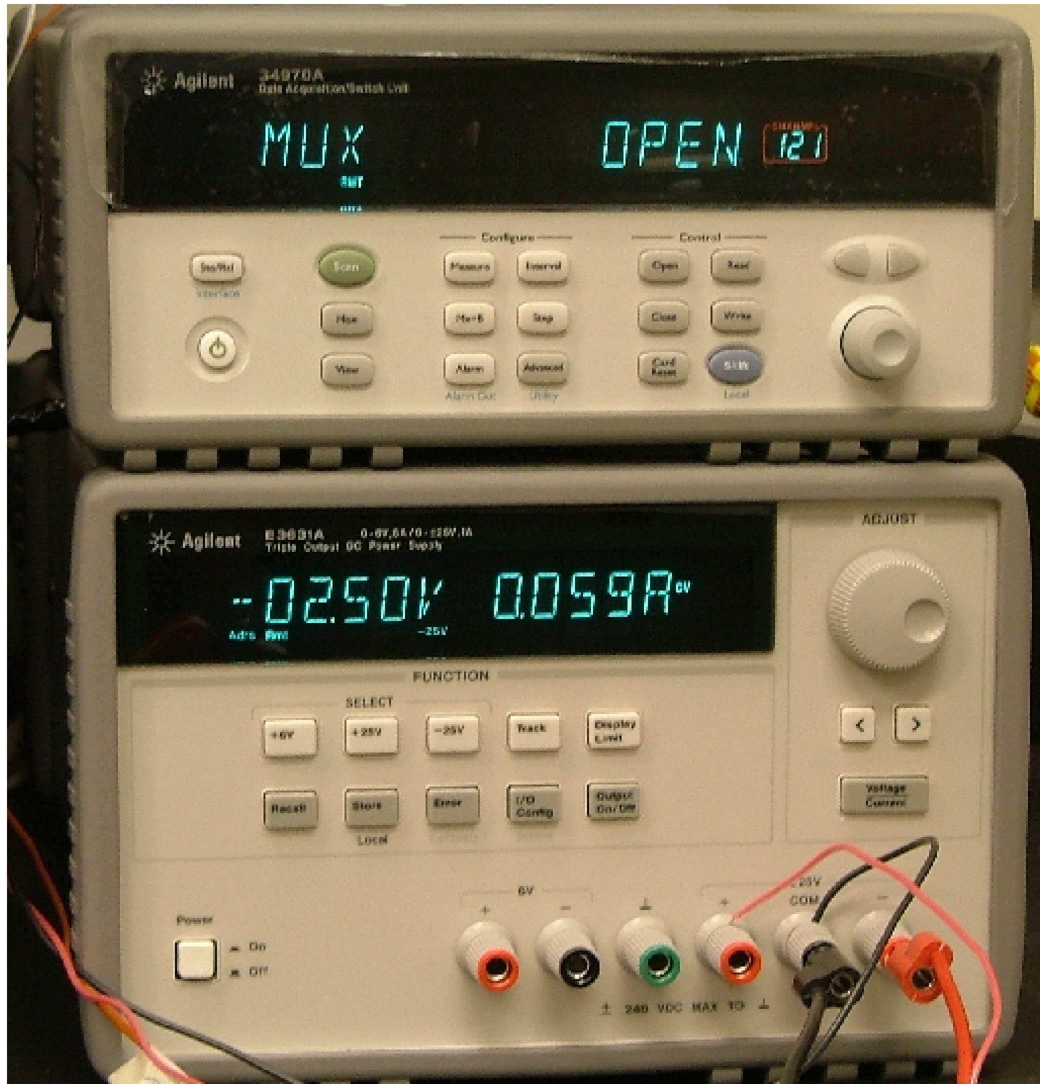


**Figure 4.9:** Front View of *Agilent* Data Acquisition Unit and Power Supply

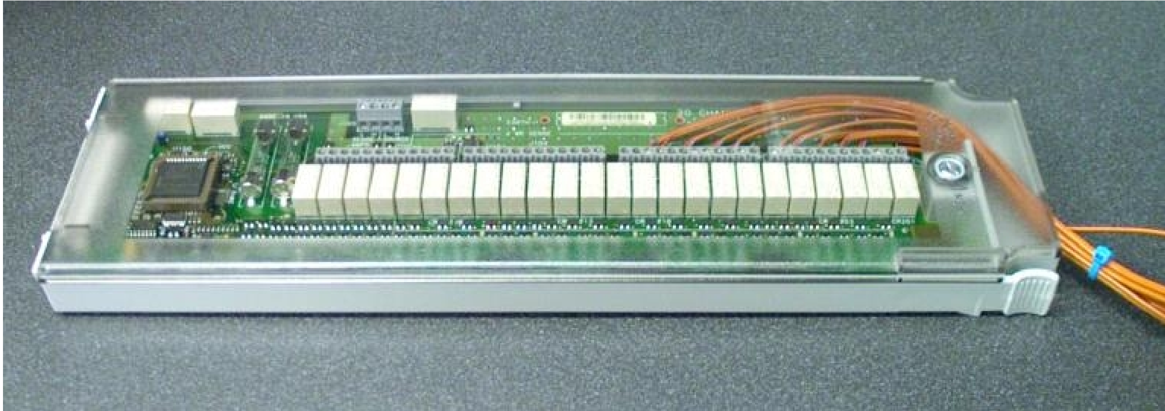

**Figure 4.10:** Thermocouples Wired to *Agilent* 34901A Multiplexer Module

numerical and graphical displays of all temperature readings, including the twenty readings of the two temperature probes, all six chip case temperatures, inlet and outlet temperature of the coolant, pump motor temperature, oven temperature, and room temperature. The user interface also includes elapsed time, and the volts, current, and power set to all three outputs. Finally, *Main Temp Logger* saves the raw data for all channels in spreadsheet format at the conclusion of each test. Figure 4.11 and Figure 4.12 show the user interface for *Main Temp Logger*.

The *Main Temp Logger* program consists of several modular sub-programs, known as subVIs, or sub-Virtual Instruments in LabVIEW™. The main subVIs of *Main Temp Logger* include *+6V Power Control*, *-25V Power Control*, *Pump Power Control*, and *High Chip Temp*. Each subVI acts programmatically like a black box. It accepts a certain number of inputs, whether these are constants, or controls on the user interface, runs them through its internal code or algorithm, and then returns one or more values to the main program in which the subVI is called. In this way, LabVIEW™ programs can be highly modular, and complex programs can be written as a sum of smaller, more simple programs.

The *+6V Power Control* subVI, and *-25V Power Control* subVI each have two modes of operation. In the first mode, the user selects the output volts for each

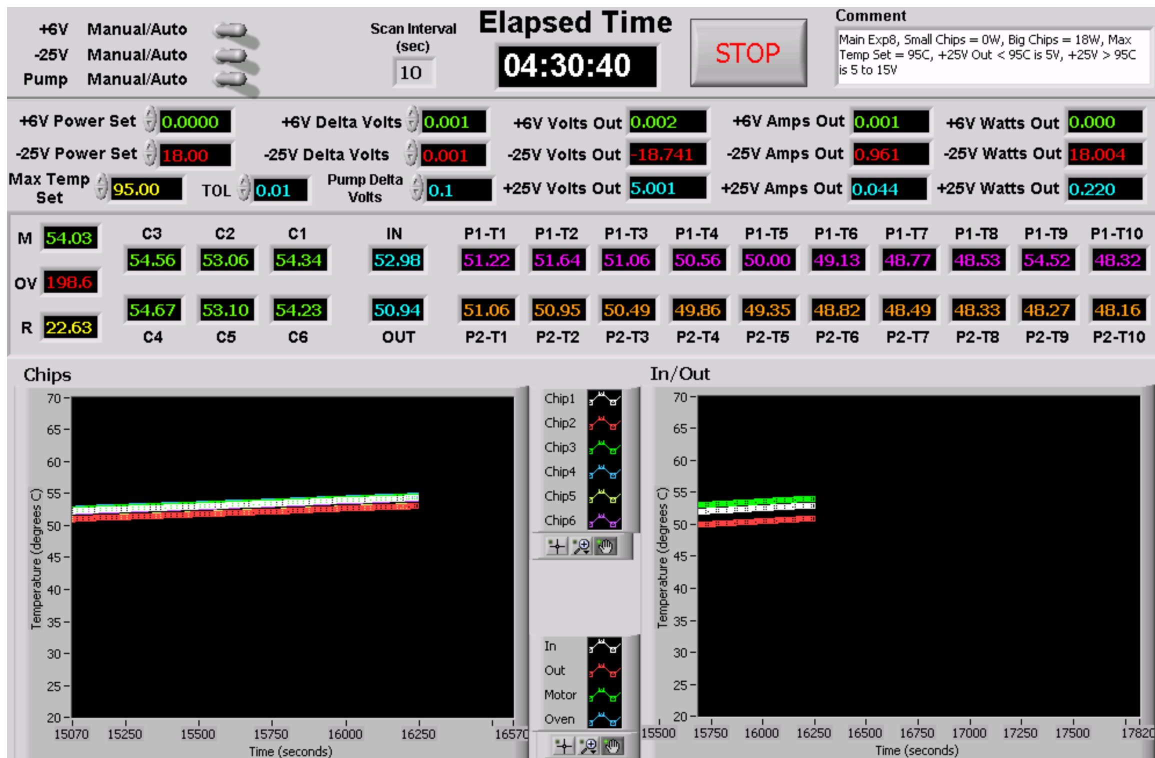


**Figure 4.11:** *Main Temp Logger* User Interface, Top Window

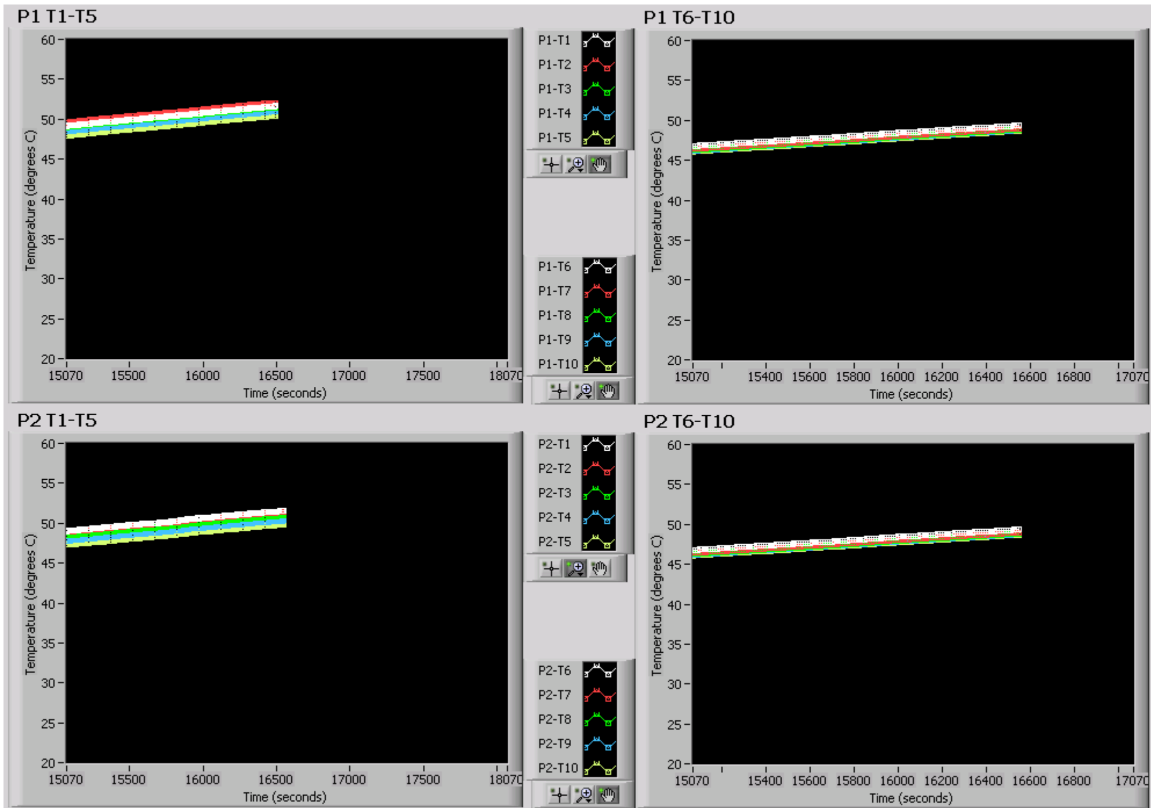


**Figure 4.12:** *Main Temp Logger* User Interface, Bottom Window

output manually. In automatic mode, the user selects the desired thermal test chip power for the big and small thermal test chips. Using a proportional control system, the *+6V Power Control* subVI and *-25V Power Control* subVI continuously monitor the power output to each set of chips, and raise or lower the voltage in increments of 1 mV to maintain the selected power. This simple control system maintains a nearly constant power to the chips, eliminating the effects of changing resistance with temperature.

The *Pump Power Control* subVI also features two modes of operation. In manual mode, the user selects the voltage output to the pump on the user interface. In automatic mode, the user selects the maximum temperature of any chip, and the *Pump Power Control* subVI uses a proportional control system that varies the flow rate to maintain the highest chip temperature at the maximum selected temperature, plus or minus 0.01 °C. If the highest chip temperature increases beyond the maximum set point by the tolerance, *Pump Power Control* increases the voltage to the pump (up to a maximum of 15 Volts), and thus flow rate through the loop, in increments of 0.1 Volts, until the highest chip temperature drops below the set point. Conversely, if the high chip temperature drops below the set point, *Pump Power Control* decreases the voltage to the pump until the voltage reaches zero, or another minimum voltage selected by the user.

The *High Chip Temp* subVI continuously monitors the case temperature of all six thermal test chips used in the four sets of prototype performance experiments. Then, it determines the highest chip temperature, and passes this information to the subVI in which the program is called. Both *Main Temp Logger*, and *Pump Power Control* call the *High Chip Temp* subVI within their code for various operations. Appendix C gives the full source code, in the form of graphical block diagrams for *Main Temp Logger*, *+6V Power Control*, *-25V Power Control*, *Pump Power Control*, and *High Chip Temp*.

## 4.5 Results and Discussion

In order to characterize the performance of the prototype thermal management system, four different sets of experiments were carried out. These include baseline experiments, experiments at various flow rates with constant power to the thermal test chips, experiments with various thermal test chip powers at a constant flow rate, and an experiment in which a proportional control system varied flow rate during a test. Table 4.2 summarizes the experimental parameters used for each of these four sets of tests. Table 4.2 also includes two durations for each test. The first represents the duration the highest chip case temperature remained below 95 °C at a fixed flow rate. The second gives the duration the highest chip case temperature remained below 100 °C, which equals the time below 95 °C at fixed flow rate, plus the time between 95 °C and 100 °C at variable flow rate. Flow rates shown come from experimental correlations described in the next chapter. Initially, distilled water was used in the flow loop, then deionized water when it became available. All tests initially start at room temperature.

### 4.5.1 Baseline Experiments

Two baseline experiments, Baseline 1 and Baseline 2, were carried out in which the thermal test chips dissipated a total of 18 Watts, at an oven temperature of 200 °C, and zero flow rate. The case temperature of the hottest thermal test chip exceeded 95 °C in only 4 hours, 2 minutes for Baseline 1, and 3 hours, 50 minutes for Baseline 2. Figure 4.13 shows various temperatures within the prototype as a function of time. Thermocouples within temperature probe 1, the inner radius probe, are labelled P1-T1 to P1-T10, P1-T1 being the closest to the thermal test chips. Thermocouples within temperature probe 2, the outer radius probe, are labelled P2-T1 to P2-T10, P2-T1 being the closest to the thermal test chips. Figure 4.14 shows the temperature gradient within the phase change material container in

**Table 4.2:** Summary of Prototype Performance Experiments

| Exp. Name | Chip Power Watts | Flow Rate kg/s (mL/min) | Cooling Fluid | Oven Temp °C | Time Below 95 °C (Fixed Flow) | Time Below 100 °C (Flow Varies) |
|---|---|---|---|---|---|---|
| Baseline 1 | 18 | 0 (0) | Distilled $H_2O$ | 200 | 4 hrs 2 min | n/a |
| Baseline 2 | 18 | 0 (0) | Distilled $H_2O$ | 200 | 3 hrs 50 min | n/a |
| Constant Power 1 | 18 | 0.00035 (21) | Distilled $H_2O$ | 200 | 20 hrs 32 min | 24 hrs 29 min |
| Constant Power 2 | 18 | 0.00084 (51) | Distilled $H_2O$ | 200 | 22 hrs 53 min | 24 hrs 52 min |
| Constant Power 3 | 18 | 0.00114 (69) | Deionized $H_2O$ | 200 | 23 hrs 43 min | 25 hrs 6 min |
| Constant Power 4 | 18 | 0.0015 (91) | Distilled $H_2O$ | 200 | 22 hrs 22 min | 23 hrs 31 min |
| Constant Flow 1 | 15 | 0.00114 (69) | Deionized $H_2O$ | 200 | 26 hrs 27 min | 27 hrs 50 min |
| Constant Flow 2 | 10 | 0.00114 (69) | Deionized $H_2O$ | 200 | 32 hrs 22 min | 33 hrs 55 min |
| Constant Flow 3 | 5 | 0.00114 (69) | Deionized $H_2O$ | 200 | 39 hrs 32 min | 41 hrs 25 min |
| Constant Flow 4 | 2 | 0.00114 (69) | Deionized $H_2O$ | 200 | 48 hrs 4 min | 50 hrs 8 min |
| Variable Flow | 18 | variable | Distilled $H_2O$ | 200 | n/a | 24 hrs 20 min |

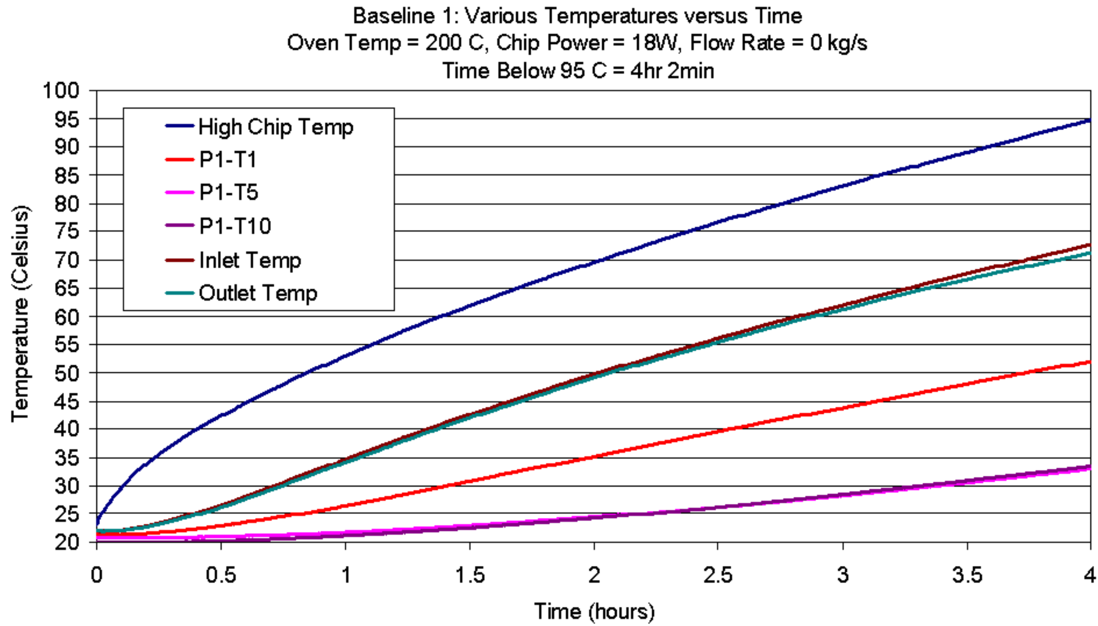


**Figure 4.13:** Various Temperatures vs Time, Baseline 1

1 hour increments for thermocouple probe 1. Figure 4.15 presents the same for thermocouple probe 2.

As expected, zero flow rate through the flow loop results in poor heat transfer between the thermal test chips and phase change material, and delivers heat storage via sensible heating only. In other words, a high thermal resistance exists between the thermal test chips and PCM. However, the temperature gradient within the PCM indicates some heat conducts to the PCM from both the thermal test chips and vacuum flask mouth, but temperatures remain at least 15 °C below melting. Small temperature differences between the temperature gradient of probe 1 and that of probe 2 suggest temperature varies little in the radial direction within the PCM container, which makes sense considering the high thermal conductivity of *Cerrobend*. Appendix A gives similar plots for Baseline 2.

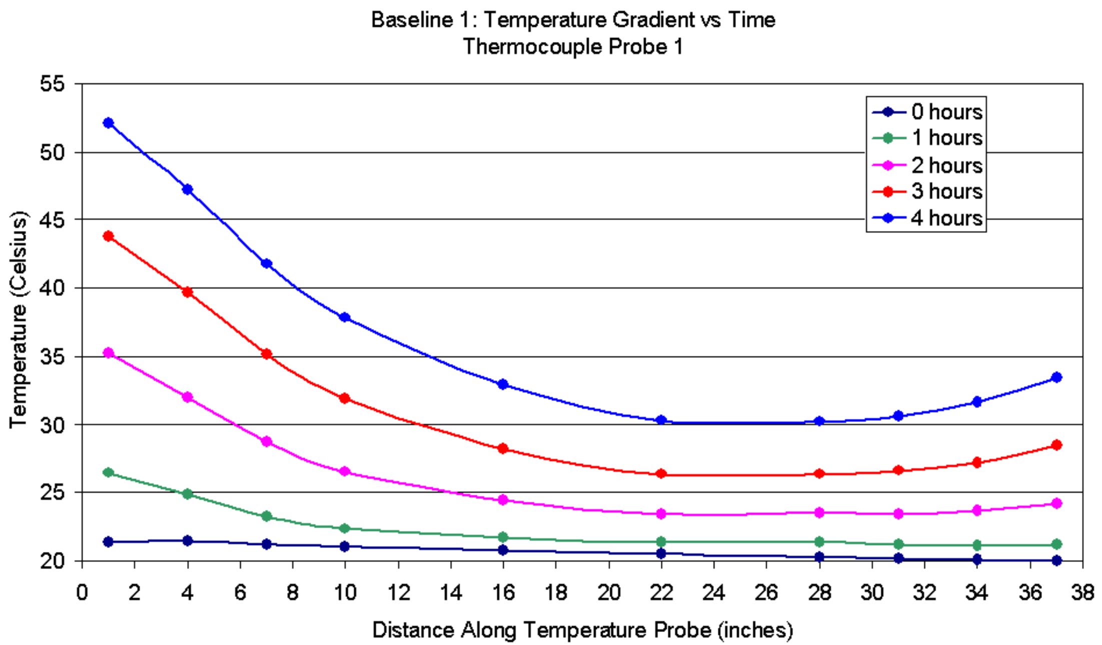


**Figure 4.14:** Temperature Gradient vs Time, Probe 1, Baseline 1

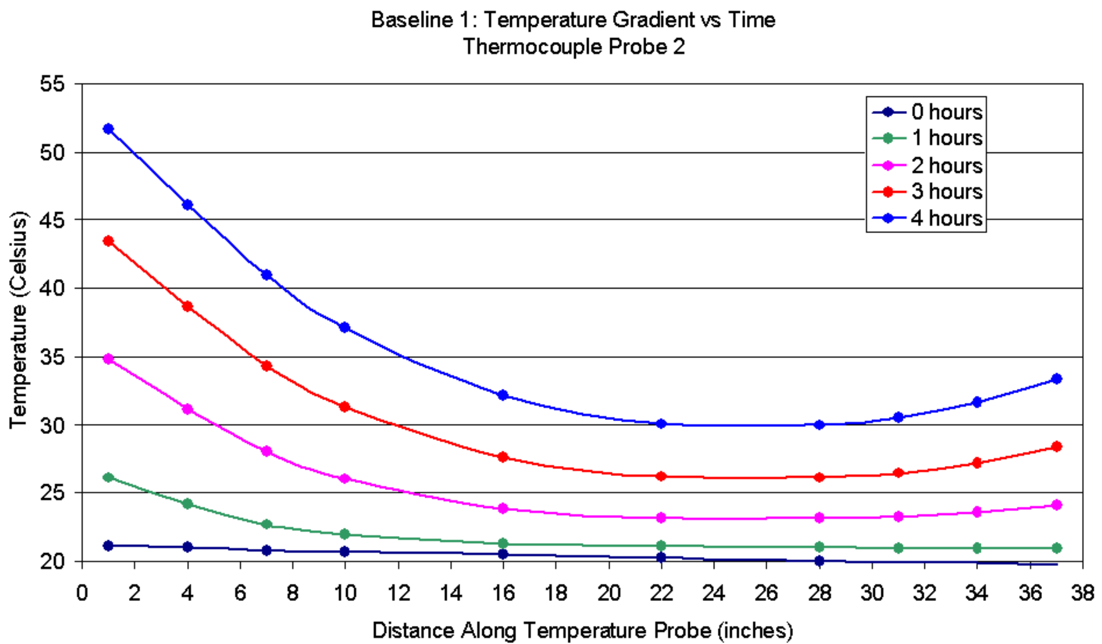


**Figure 4.15:** Temperature Gradient vs Time, Probe 2, Baseline 1

### 4.5.2 Constant Chip Power Experiments

Four experiments, Constant Power 1, Constant Power 2, Constant Power 3, and Constant Power 4, were performed with a total of 18 Watts dissipated by test chips, at flow rates of about 0.00035 kg/s (21 mL/min), 0.00084 kg/s (51 mL/min), 0.00114 kg/s (69 mL/min), and 0.0015 kg/s (91 mL/min), respectively. For all four experiments, flow rate was held constant to determine duration for which temperature is below 95 °C. Once this temperature is reached the LabVIEW™ control program, *Pump Power Control*, began to adjust the voltage to the pump, increasing the flow rate to maintain chip temperatures at or below the maximum set point, 95 °C. This maximized heat stored by the PCM, and downhole service time. Figure 4.16 shows various prototype temperatures as a function of time for Constant Power 1. The temperature gradient within the PCM from thermocouple probe 1 is shown in Figure 4.17, and Figure 4.18 gives the same for thermocouple probe 2. Appendix A gives plots for Constant Power 2, Constant Power 3, and Constant Power 4.

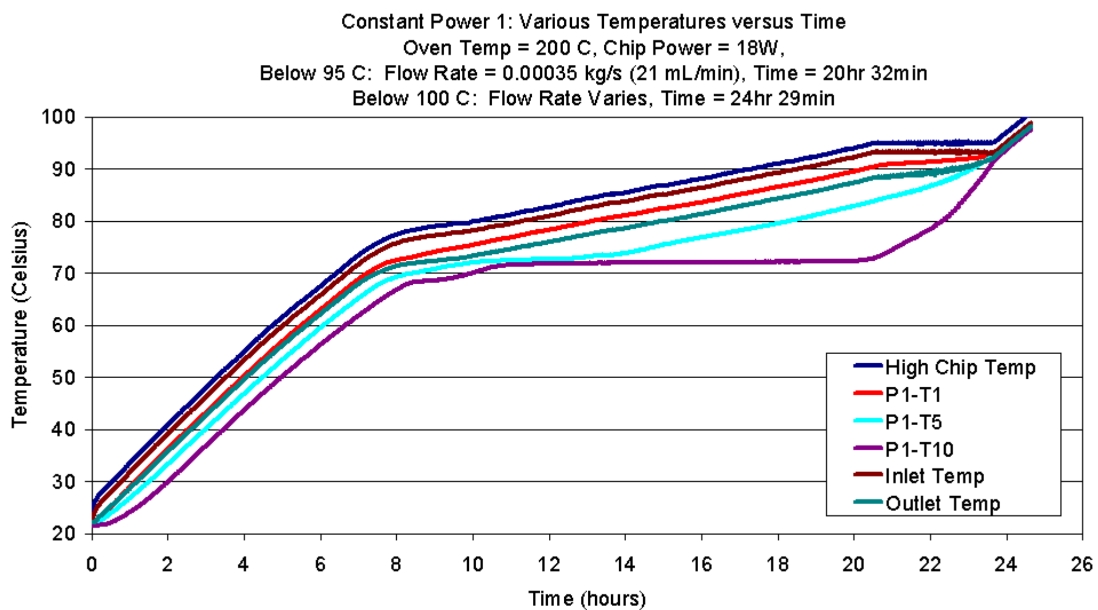


**Figure 4.16:** Various Temperatures vs Time, Constant Power 1

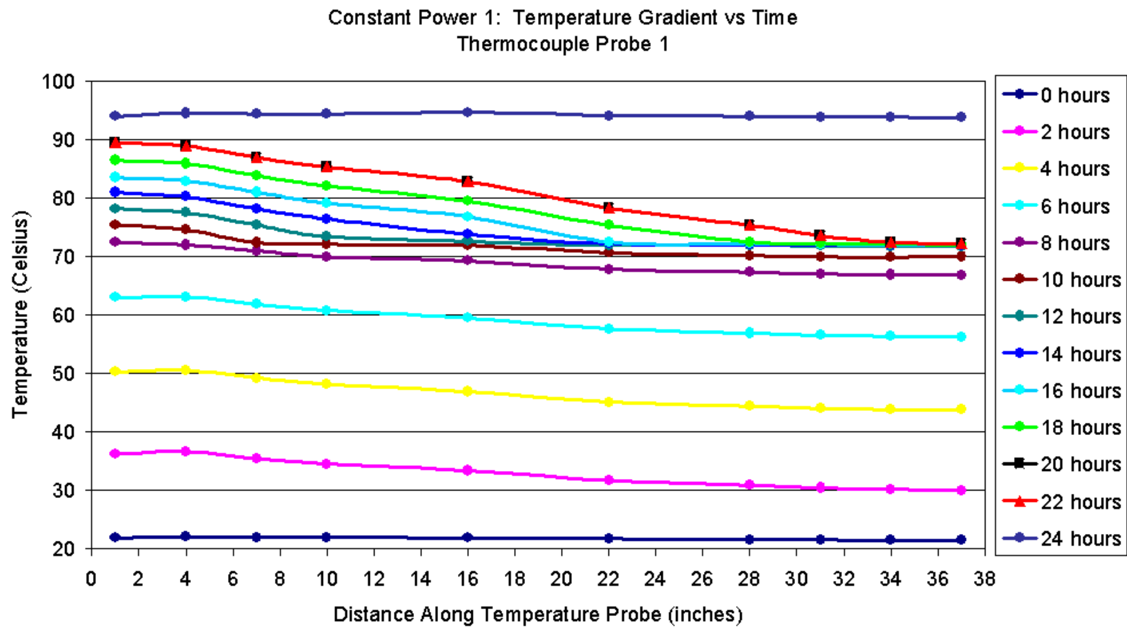


**Figure 4.17:** Temperature Gradient vs Time, Probe 1, Constant Power 1

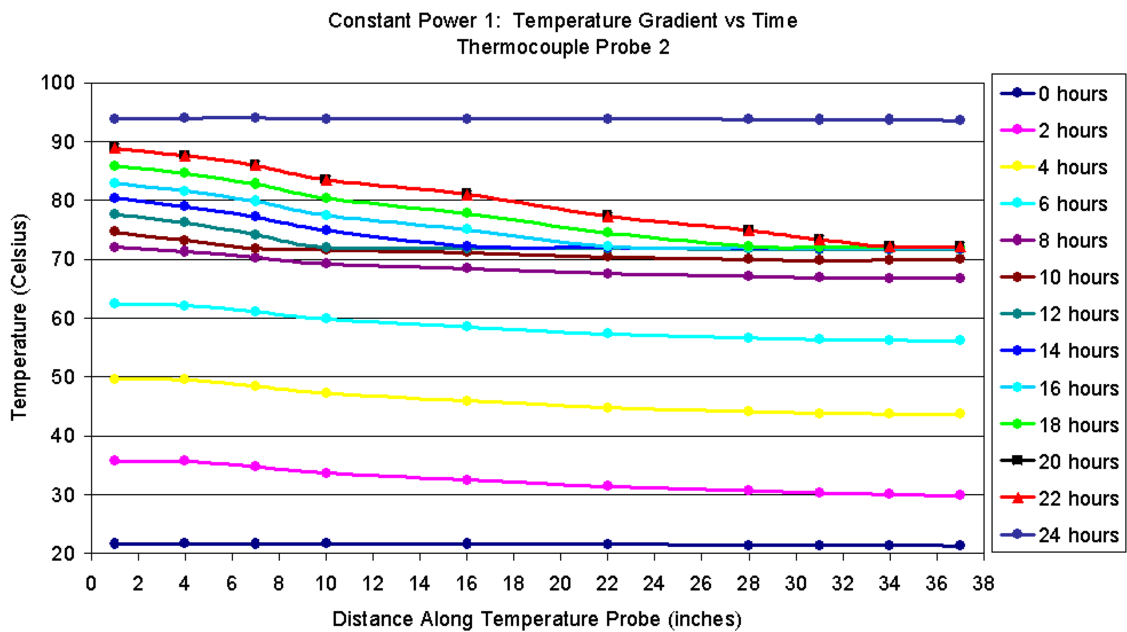


**Figure 4.18:** Temperature Gradient vs Time, Probe 2, Constant Power 1

For Constant Power 1, a flow rate of only 0.00035 kg/s (21 mL/min) through the flow loop maintains the case temperature of the hottest chip below 95 °C for over 20 hours. This represents a factor of five improvement over the baseline experiments. The *Pump Power Control* program maintains the hottest thermal test chip below 100 °C for an additional 4 hours, 29 minutes, which exceeds design targets by about a half-hour. The temperature gradient within the PCM container remains relatively flat for the duration of the Constant Power 1 test, except during melting. This indicates a low thermal resistance between the thermal test chips and PCM. Again, small differences in the results between thermocouple probe 1 and probe 2 suggest temperature does not vary significantly in the radial direction within the PCM container. Figure 4.19 summarizes the results for these experiments in terms of total time the highest chip temperature remains below 95 °C, while starting from a common average initial temperature of 22.8 °C. Clearly, a flow rate of about 0.00114 kg/s (69 mL/min) maintains the hottest chip below 95 °C for the longest time.

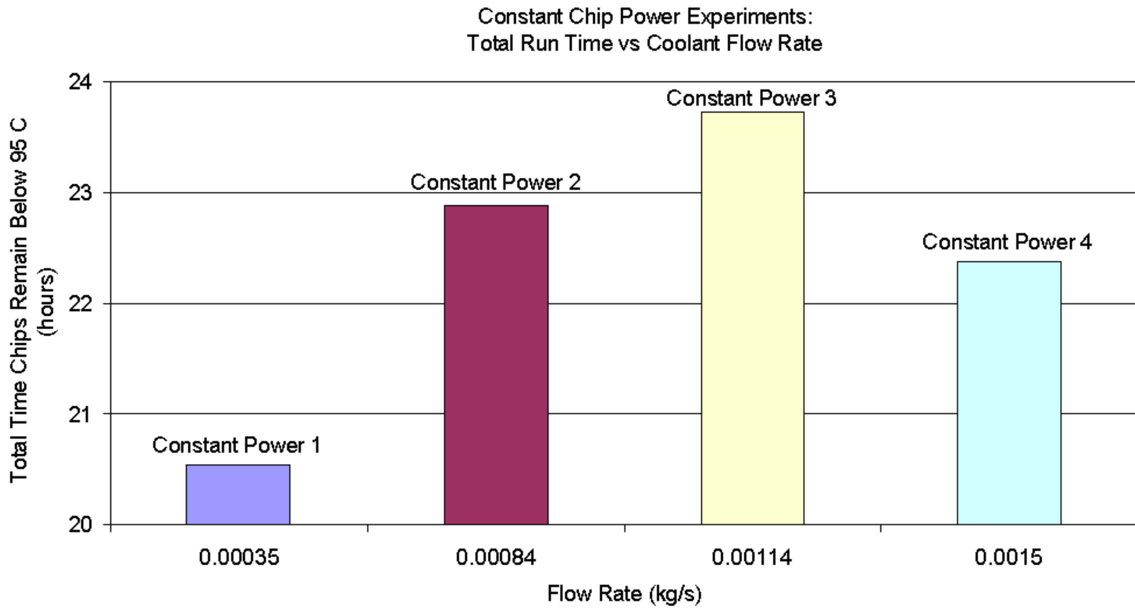


**Figure 4.19:** Total Run Time vs Flow Rate for Constant Chip Power Experiments

This flow rate most likely corresponds to the highest efficiency of the pump motor for the particular pressure drop through the flow loop, thereby minimizing extra heat introduced into the system via the pump.

### 4.5.3 Constant Flow Rate Experiments

This section describes prototype performance experiments wherein flow rate remains at an optimal 0.00114 kg/s (69 mL/min), with various power consumptions by the test chips. The four experiments, Constant Flow 1, Constant Flow 2, Constant Flow 3, and Constant Flow 4 were performed at test chip heat dissipations of 15 Watts, 10 Watts, 5 Watts, and 2 Watts, respectively. Figure 4.20 shows the variation of several prototype temperatures over time for Constant Flow 1. The highest chip case temperature in this case remains below 95 °C for 26 hours, 27 minutes. *Pump Power Control*, the LabVIEW™ control program, allows the flow rate to increase, extending the time the highest chip remains below 100 °C by 1 hour, 23

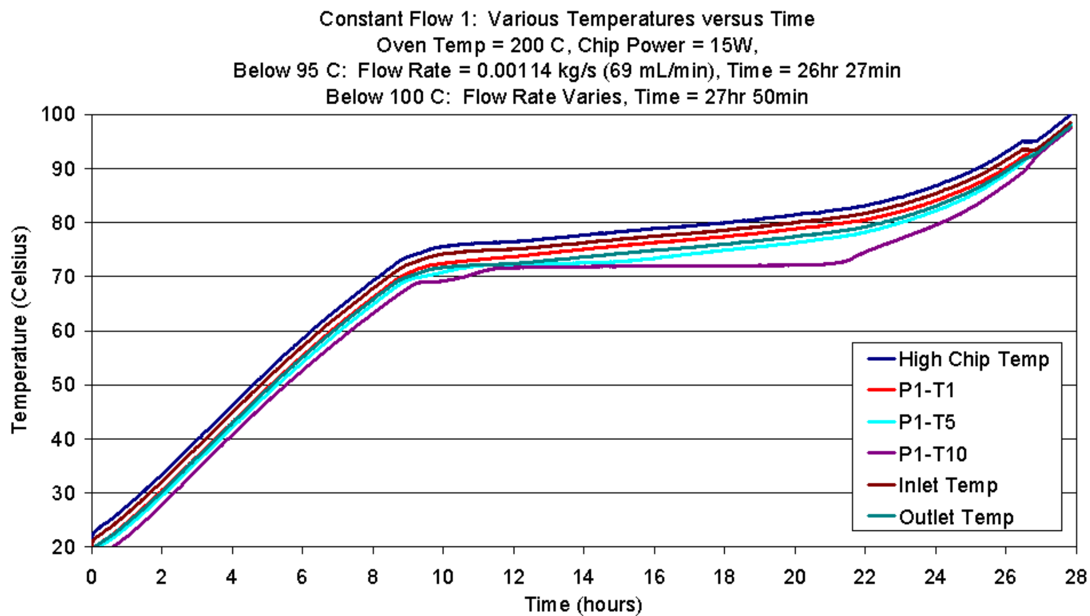


**Figure 4.20:** Various Temperatures vs Time, Constant Flow 1

minutes, for a total operating time of 27 hours, 50 minutes. Figure 4.21 shows the temperature distribution from thermocouple probe 1 over time, and a similar plot for thermocouple probe 2 is shown in Figure 4.22. Appendix A contains additional data plots for Constant Flow 2, Constant Flow 3, and Constant Flow 4. Figure 4.23 graphs the highest chip case temperature as a function of time for chip power dissipations of 2 Watts, 5 Watts, 10 Watts, 15 Watts, and 18 Watts. For these five power dissipations, Figure 4.24 summarizes the total time the chips remain below 95 °C.

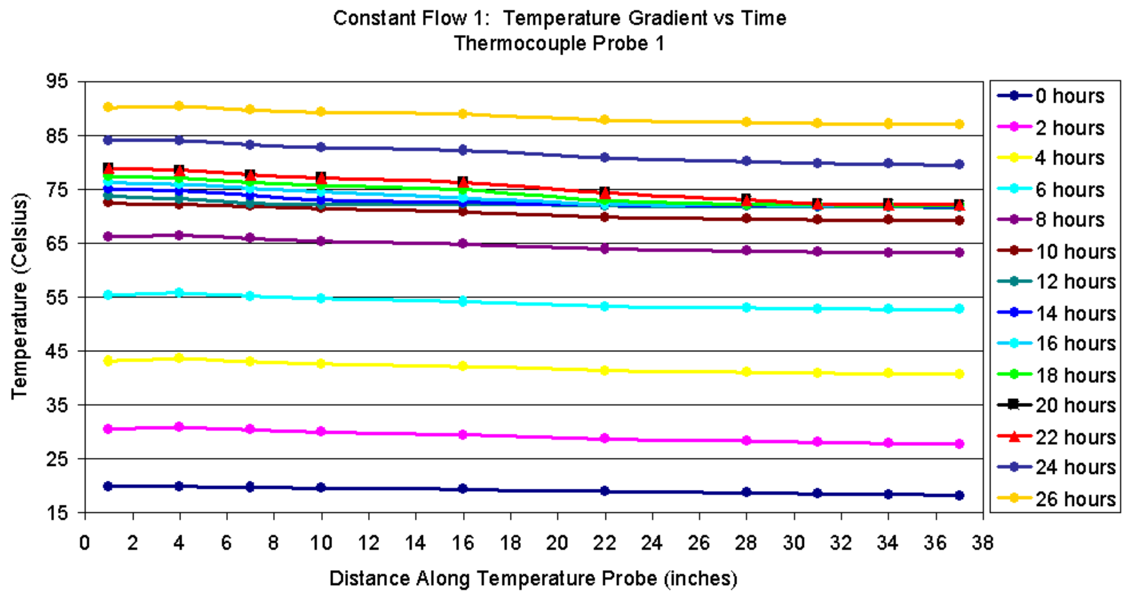


**Figure 4.21:** Temperature Gradient vs Time, Probe 1, Constant Flow 1

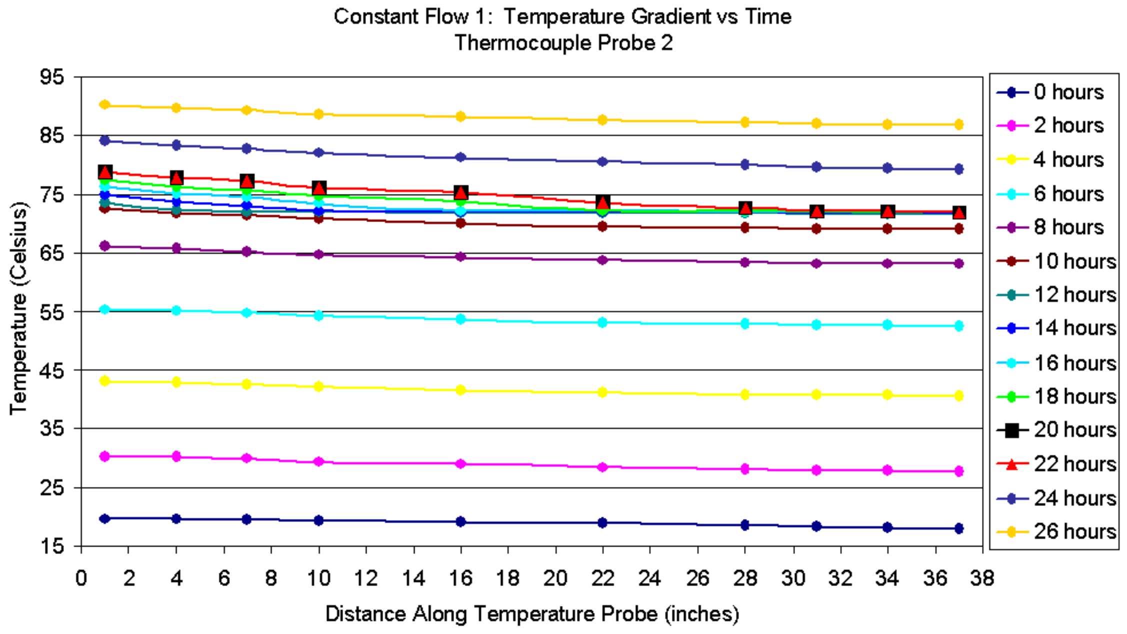


**Figure 4.22:** Temperature Gradient vs Time, Probe 2, Constant Flow 1

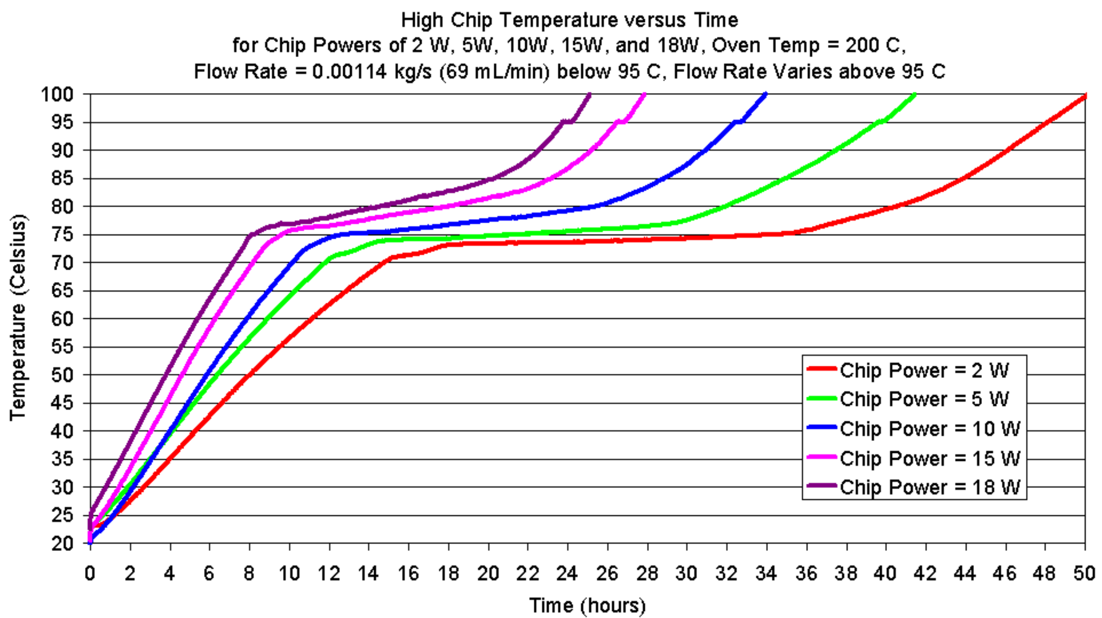


**Figure 4.23:** Highest Chip Temperature vs Time for 2W, 5W, 10W, 15W, 18W

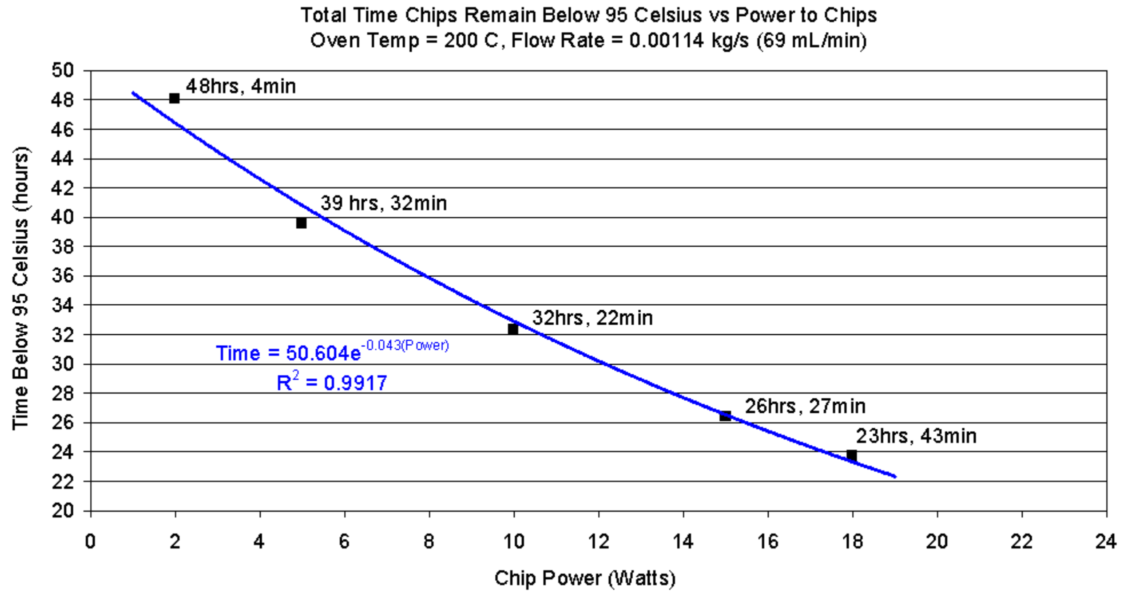


**Figure 4.24:** Time Chips Remain Below 95 Celsius vs Power Dissipated

### 4.5.4 Control System Experiment

In this experiment, Variable Flow, the LabVIEW™ control program monitors the highest chip case temperature and varies the flow rate through the flow loop to maintain this temperature at or below 95 °C, while the chips dissipate 18 Watts. Until this temperature exceeds 95 °C, the pump remains off. Results show the control system successfully maintained the highest chip case temperature below 100 °C for 24 hours, 20 minutes. This is about 46 minutes less than Constant Power 3. Figure 4.25 gives various temperatures as a function of time for the Variable Flow test. The simplicity of the control algorithm, and a lag in response time contribute to the oscillations shown in these data. Figure 4.26 gives the temperature distribution in the PCM from thermocouple probe 1, and Figure 4.27 gives the same for thermocouple probe 2.

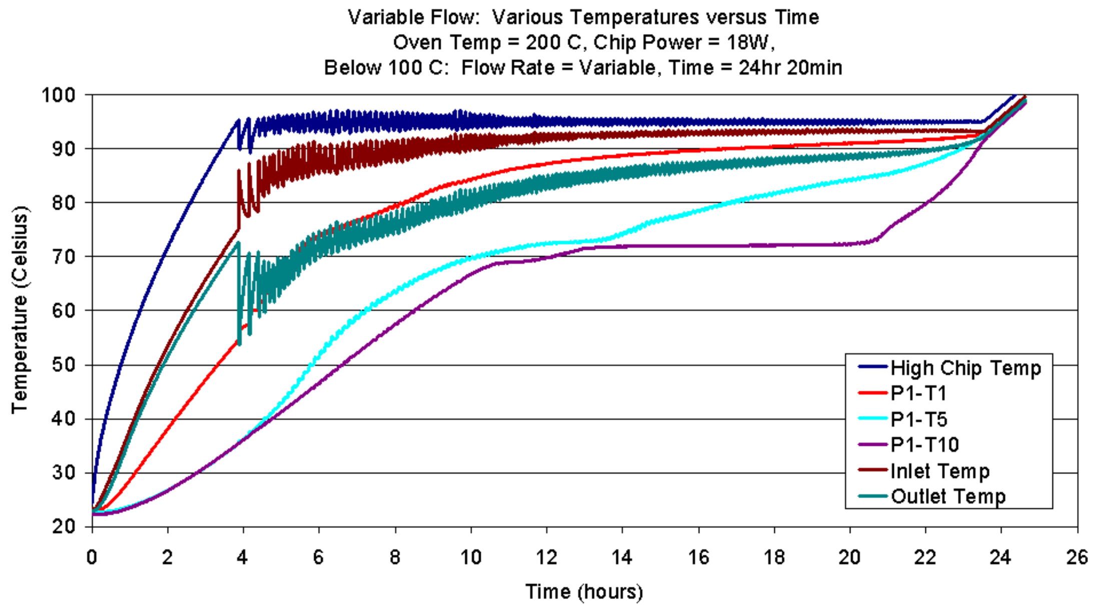


**Figure 4.25:** Various Temperatures vs Time, Variable Flow

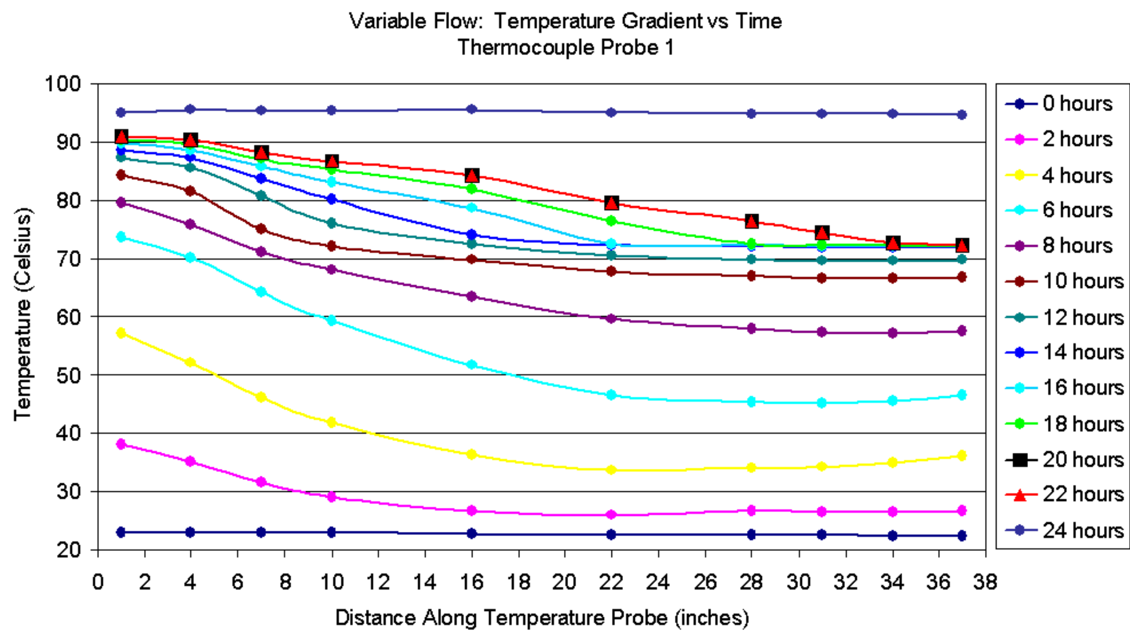


**Figure 4.26:** Temperature Gradient vs Time, Probe 1, Variable Flow

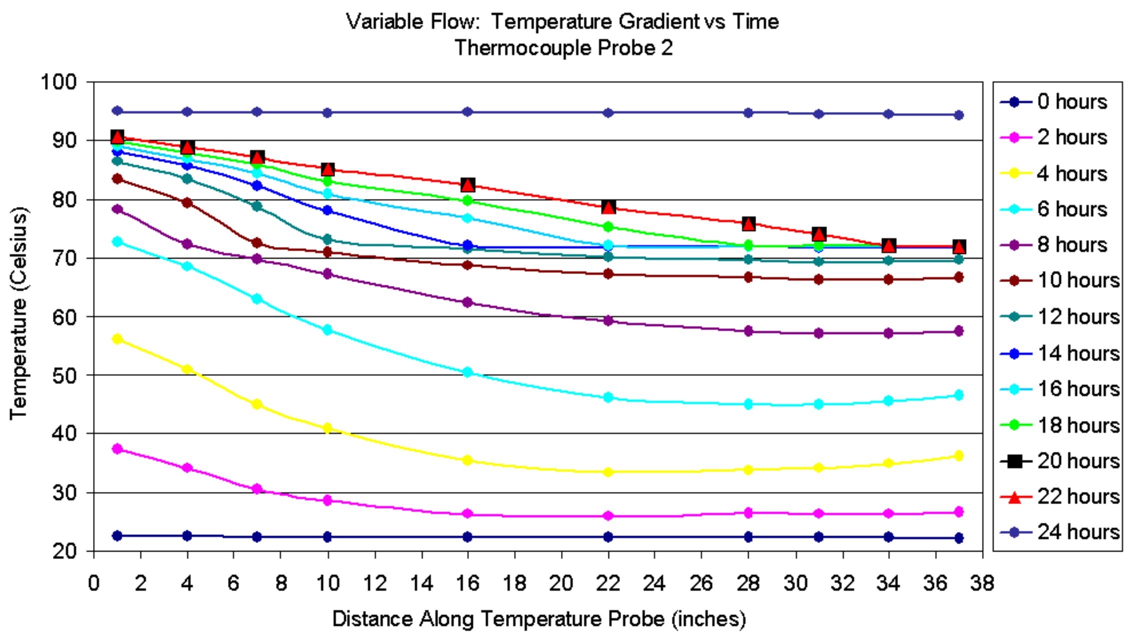


**Figure 4.27:** Temperature Gradient vs Time, Probe 1, Variable Flow

# CHAPTER 5

# FLOW RATE CORRELATION EXPERIMENTS

## *5.1 Purpose*

During the four sets of prototype performance tests, the flow rate through the flow loop was not directly measured. The main objective of these experiments is to establish a correlation between the coolant flow rate through the flow loop and the voltage supplied to the pump, which was carefully monitored and recorded for every prototype performance test. One secondary objective of these experiments includes the investigation of the effect of temperature on flow rate. Another consists of establishing a correlation between power supplied to the pump versus flow rate.

## *5.2 Approach*

Since the pressure drop through the flow loop does not change during tests, the flow rate depends directly on the revolutions per minute (RPM) of the gear pump. By nature of its construction and design, a gear pump delivers a known volume of liquid per revolution of its gears, assuming no slip. This means that for a given pressure drop, flow rate depends on the RPM of the pump gears. The RPM of these gears depends directly on the RPM of the DC motor used to magnetically drive the pump. The DC motor RPM, in turn, depends directly on the DC voltage provided to the motor. Therefore, there is a linear relationship between flow rate through the flow loop and voltage supplied to the pump motor. This means a correlation of flow rate versus voltage supplied to the pump provides a means to calculate coolant flow rate through the flow loop to a reasonable degree of accuracy.

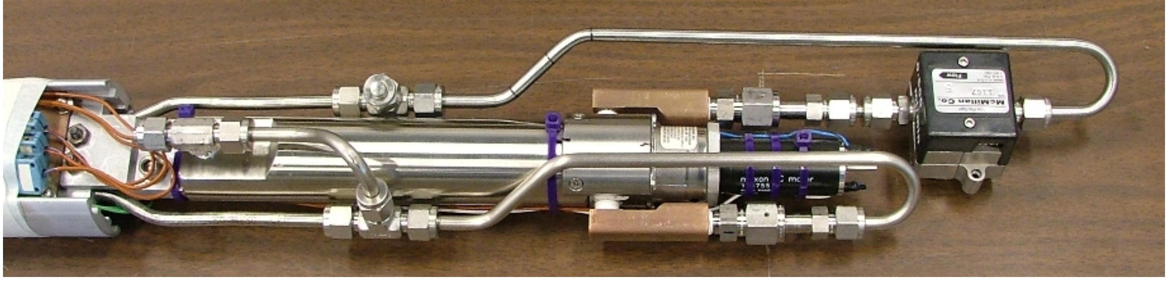

**Figure 5.1:** Flow Sensor Added to Closed Flow Loop of Prototype

## *5.3 Apparatus and Procedure*

A turbine style flow meter with negligible pressure drop was added to the prototype flow loop. Made by *McMillan Co.* this flow meter measures flow rates between 50 and 500 mL/min, features and accuracy of ± 1% full scale, built-in temperature compensation, stainless steel compression fittings, and comes with a NIST (National Institute of Standards and Technology) traceable calibration certificate. The short length of tubing that connects the cold plate to the inlet side of the pump was removed, and replaced with two lengths of stainless steel tubing and the flow sensor. Figure 5.1 shows the black flow sensor added to the closed flow loop near the pump inlet.

Next, the flow loop was evacuated and filled with water as described in the previous chapter. Then, the data acquisition system was switched on and the flow rate was monitored and recorded every 5 seconds for 10 minutes at a given pump voltage setting. This was repeated for pump voltage settings of 3 Volts to 14 Volts and back to 3 Volts in 1 Volt increments. Finally, this procedure was repeated at temperatures of 30 °C and 40 °C using the *Despatch* oven. The temperature of the oven was maintained below 50 °C, the maximum temperature rating of the flow sensor, to prevent damage.

## 5.4 Data Acquisition

### 5.4.1 Hardware

Nearly identical to the prototype performance experiments, the data acquisition (DAQ) hardware used for these experiments consists of the *Agilent* 34970A data acquisition/switch unit, the *Agilent* E3631A DC power supply, two *Agilent* 34901A armature multiplexer plug-in cards, two standard GPIB (general purpose interface bus) cables, a GPIB PCI (peripheral component interconnect) card, and a *Dell* desktop computer. For these tests, the DC power supply delivers no power to the thermal test chips, pump power via the +25V output, and powers the flow sensor via the -25V output. A schematic of the hardware connections for this experiment as shown in Figure 5.2.

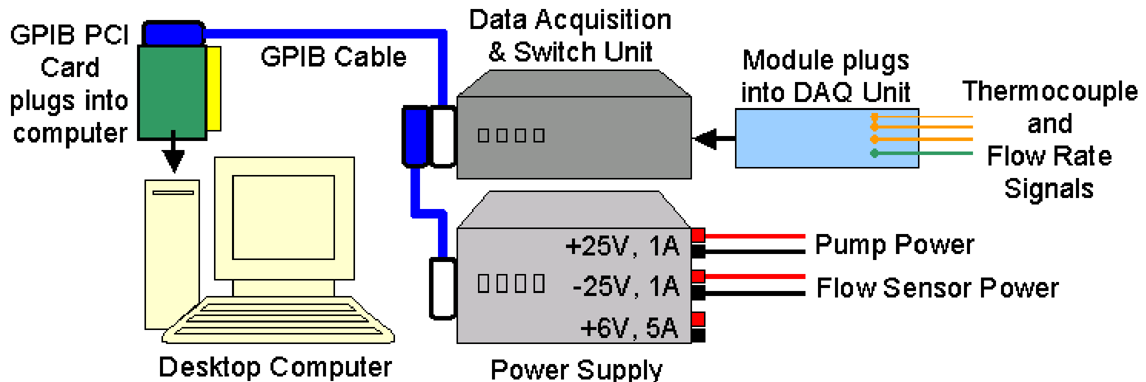


**Figure 5.2:** Schematic of DAQ Hardware for Flow Rate Correlation

### 5.4.2 Software

A derivative of the *Main Temp Logger* LabVIEW™ program was used for data acquisition, called *Flow Rate vs Voltage Logger*. This program is equivalent to *Main Temp Logger* in all respects except that the *Pump Power Control* subVI was replaced with a subVI called *F vs V Pump Control*. This new pump control sub-program

automatically adjusts the voltage to the pump from 3 Volts to 14 Volts to 3 Volts in increments of 1 Volt, waiting for ten minutes at each voltage setting for the flow rate to be recorded. This frees the user from having to manually adjust the voltage to the pump every ten minutes. Appendix C gives block diagrams for *Flow Rate vs Voltage Logger*, and *F vs V Pump Control*.

## 5.5 Results and Discussion

The *Flow Rate vs Voltage Logger* LabVIEW program continuously monitored and recorded temperature and flow rate readings at five second intervals for the ascending and descending pump voltage settings, resulting in well over a hundred flow rate readings per voltage setting on the pump. At each pump voltage setting from 3 Volts to 14 Volts to 3 Volts, the mean and standard deviation of flow rate were calculated. Chauvenet's criterion, as described by Holman, was then applied to each data set. This criteria provides a statistical means to exclude anomalous data points caused by air bubbles in the test section [15]. These air bubbles, produced by cavitation at the pump inlet, caused the flow meter's turbine to either stall or spin freely, resulting in irregular flow rate readings.

To apply Chauvenet's criterion, one first calculates the mean, $x_m$, and standard deviation, $\sigma$, for the data set. Next, the deviation of each reading from the mean, $d_i$, is calculated using

$$d_i = x_i - x_m \tag{5.1}$$

where $x_i$ is the $i^{th}$ reading in the data set. Then, the ratio $d_i/\sigma$ is calculated for each reading. According to Chauvenet's criterion, for 50 total readings, a reading may be excluded if $|d_i/\sigma| > 2.57$. For 100 total readings, a reading may be excluded if $|d_i/\sigma| > 2.81$. For 300 total readings, a reading may be excluded if $|d_i/\sigma| > 3.14$. In this manner, anomalous flow rate readings were excluded, and a new mean and standard deviation were calculated.

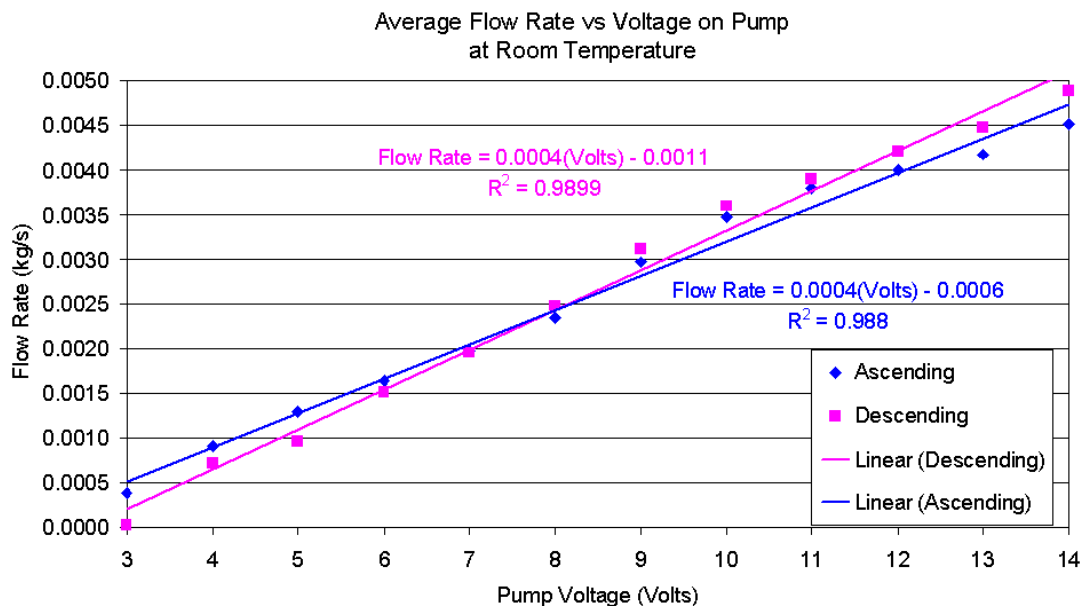


**Figure 5.3:** Average Flow Rate vs Pump Voltage at Room Temperature

Figure 5.3 gives the average flow rate through the flow loop versus pump voltage at room temperature. Figure 5.4 gives a similar plot at 30 °C. Average flow rate versus pump voltage at 40 °C is given by Figure 5.5. As expected, a linear relationship exists between the flow rate through the flow loop and the voltage supplied to the pump. Over the temperature range tested, the correlation between flow rate and pump voltage does not change appreciably. Figure 5.6 shows the variation of pump power consumption with respect to flow rate. This correlation can be used to estimate the heat added to the vacuum flask by the pump for a given flow rate.

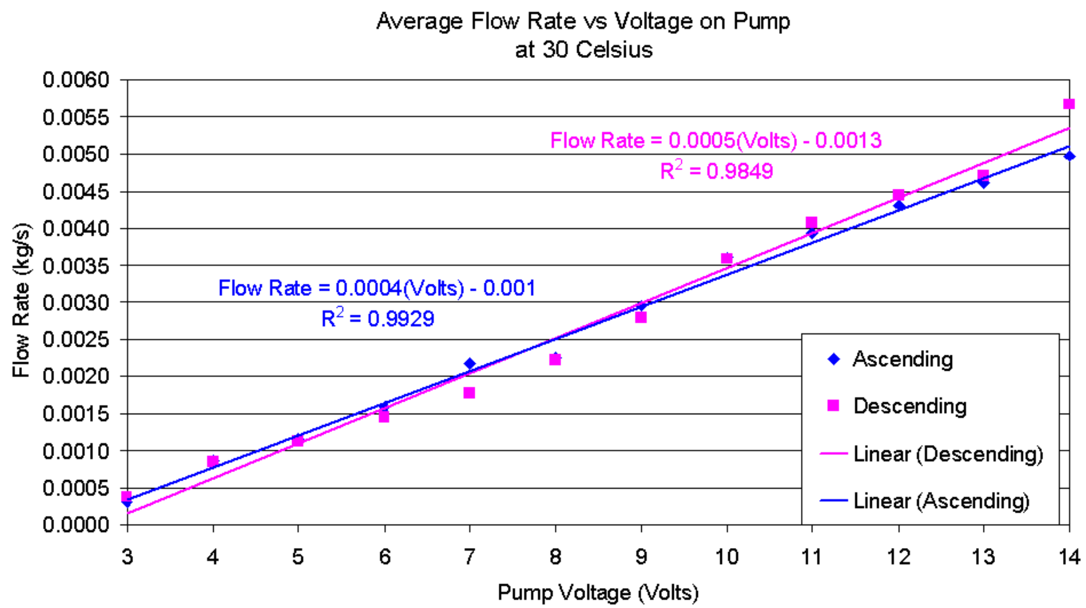


**Figure 5.4:** Average Flow Rate vs Pump Voltage at 30 Celsius

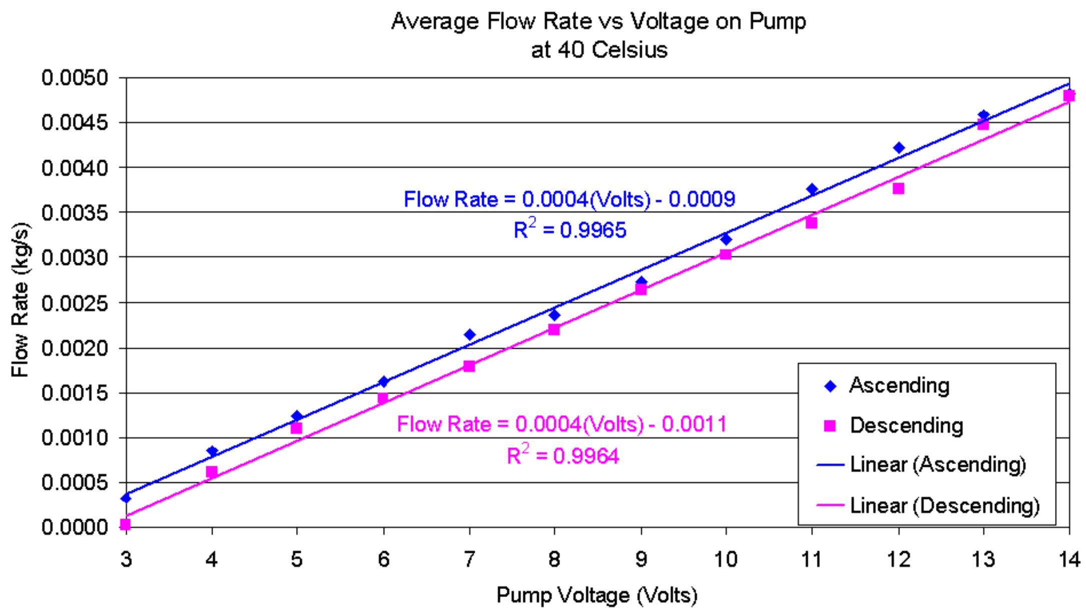


**Figure 5.5:** Average Flow Rate vs Pump Voltage at 40 Celsius

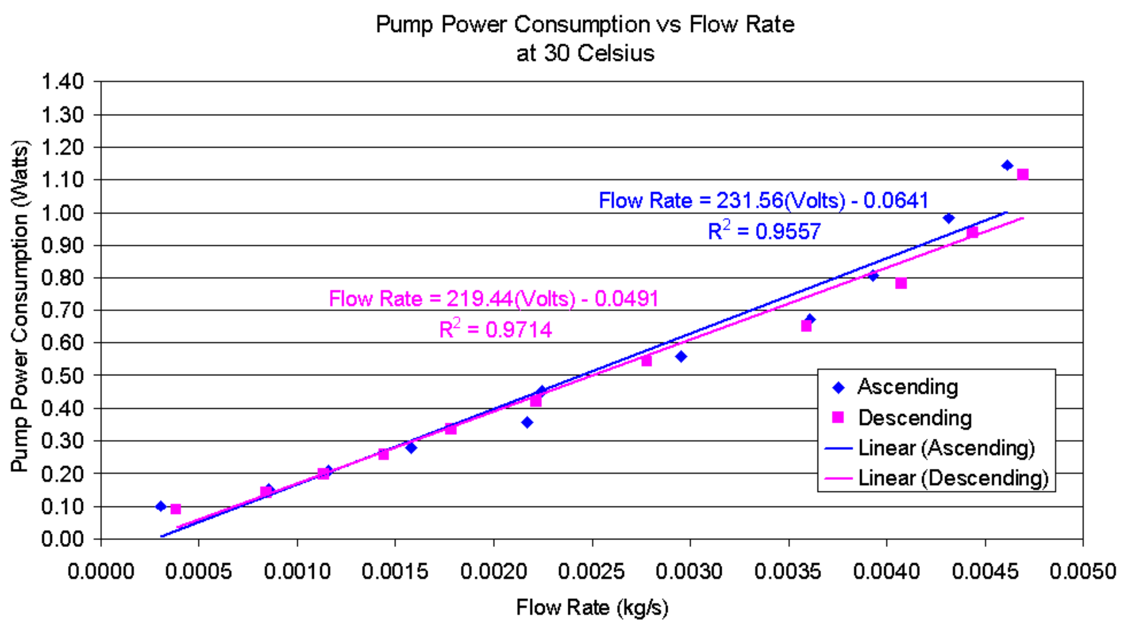


**Figure 5.6:** Pump Power Consumption vs Flow Rate at 30 Celsius

# CHAPTER 6

# VACUUM FLASK THERMAL PERFORMANCE EXPERIMENTS

## *6.1 Purpose*

The objective of these experiments is to assess the thermal insulation performance of the vacuum flask. Specifically, the main goal of these experiments is to determine the overall heat transfer coefficient for the vacuum flask, $U$, measured in W/m$^2$·K. Another goal is to compare the experimental value for $U$ to the value quoted by the vacuum flask manufacturer, *Vacuum Barrier Corp.* The overall heat transfer coefficient, $U$, takes into account heat transfer via conduction, convection, and radiation through the vacuum flask. An accurate accounting of the total heat transferred through the vacuum flask from a high temperature environment is critical to the modelling and design of the thermal management system, and future vacuum flask applications.

## *6.2 Approach*

The general approach of these experiments involves filling the vacuum flask with boiling water, and recording water temperature over time. Since no insulator is perfect, some thermal energy inevitably escapes through the vacuum flask into the room temperature environment, slowly reducing the temperature of the water. The lumped capacitance method describes this transient process with reasonable accuracy. Using this method, an energy balance around a water filled vacuum flask gives

$$T\left(t\right) = \left(T_o - T_\infty\right) e^{\left(-\frac{UA}{mc_p}t\right)} + T_\infty \tag{6.1}$$

where $T(t)$ is the temperature of the water inside the vacuum flask at any time, $t$, $T_o$ is the initial temperature of the water within the flask, $T_\infty$ is the ambient temperature outside the flask, $A$ is the flask internal surface area, $m$ is the total mass of water inside the flask, $c_p$ is the specific heat of water, and $U$ is the overall heat transfer coefficient through the vacuum flask [16]. Equating an exponential best-fit line of the measured water temperature versus time to Equation 6.1, one can determine the overall heat transfer coefficient, $U$, for the vacuum flask.

This approach assumes the temperature of the water inside the vacuum flask is spatially uniform, and is valid to a reasonable degree of accuracy if the following condition is satisfied

$$Bi = \frac{UL_c}{k} < 0.1 \tag{6.2}$$

where $Bi$ is the Biot number, $U$ is the overall heat transfer coefficient, $L_c$ is the characteristic length of the system, equal to the radius of the vacuum flask, and $k$ is the thermal conductivity of the medium, water in this case [16]. In the radial direction of the vacuum flask, $Bi << 1$, allowing one to neglect radial temperature gradients without significant loss in accuracy. In the axial direction of the vacuum flask, it is expected experiments will show negligible temperature gradients over time, validating the use of the lumped capacitance method to a reasonable degree of accuracy.

## *6.3 Apparatus and Procedure*

First, a laboratory hot plate was used to boil about twelve quarts of tap water in a stock pot. Next, the vacuum flask was tipped onto a roller stand to easily fill the vacuum flask with water. However, the long length and narrow opening of the vacuum flask made it difficult to pour water directly from the stock pot into the vacuum flask. Instead, an inexpensive high flow rate drill pump, driven by a hand drill, transferred the boiling water to the vacuum flask. Once the vacuum flask was nearly full of water, data acquisition began. Figure 6.1 shows the hot plate and

**Figure 6.1:** Hot Plate, Stock Pot, Hand Drill, and Drill Pump

stock pot used to boil the water, and the drill pump/hand drill used to rapidly pump boiling water into the vacuum flask. Figure 6.2 illustrates the vacuum flask in tipped position.

Then, a custom thermocouple probe was quickly and carefully inserted into the vacuum flask, followed by the PEEK (polyetheretherketone) end cap, which insulates the flask opening. The next section describes the thermocouple probe in more detail. To ensure an equal volume of water between experimental runs, the thermocouple probe and end cap displaced enough water to cause small amounts to spill from the flask opening. Next, the vacuum flask, end cap, and contents were raised vertically, and secured to a strut stand with a large hose clamp. The strut stand consists of a steel post base and 4.13 cm (1 5/8") strut, permanently attached to the laboratory desk using angle brackets and wood screws. A 7.62 cm (3") rubber pipe fitting prevents damage to the vacuum flask by the hose clamp, and a 7.62 cm (3") rubber

**Figure 6.2:** Vacuum Flask Tipped onto Roller Stand

end cap protects the bottom end of the vacuum flask while keeping it from slipping along the floor. Figure 6.3 gives an overview of the experimental setup, and shows the setup during data acquisition.

Next, a data acquisition system logged twelve thermocouple readings for over twenty-four hours. Section 6.5 gives a full description of both the hardware and software used to acquire these data. Once data acquisition ceased, the thermocouple probe and end cap were removed from the vacuum flask and allowed to dry. Finally, water from the vacuum flask was drained into a lab sink, and the empty vacuum flask was returned to the strut post. In this vertical position, the vacuum flask cooled for twenty-four hours, and any trace amounts of water remaining in the flask evaporated. Table 6.1 itemizes the apparatus of these experiments, and includes a detailed description, such as manufacturer, model number, serial number, or part number. Table 6.2 summarizes the procedures used during each experiment.

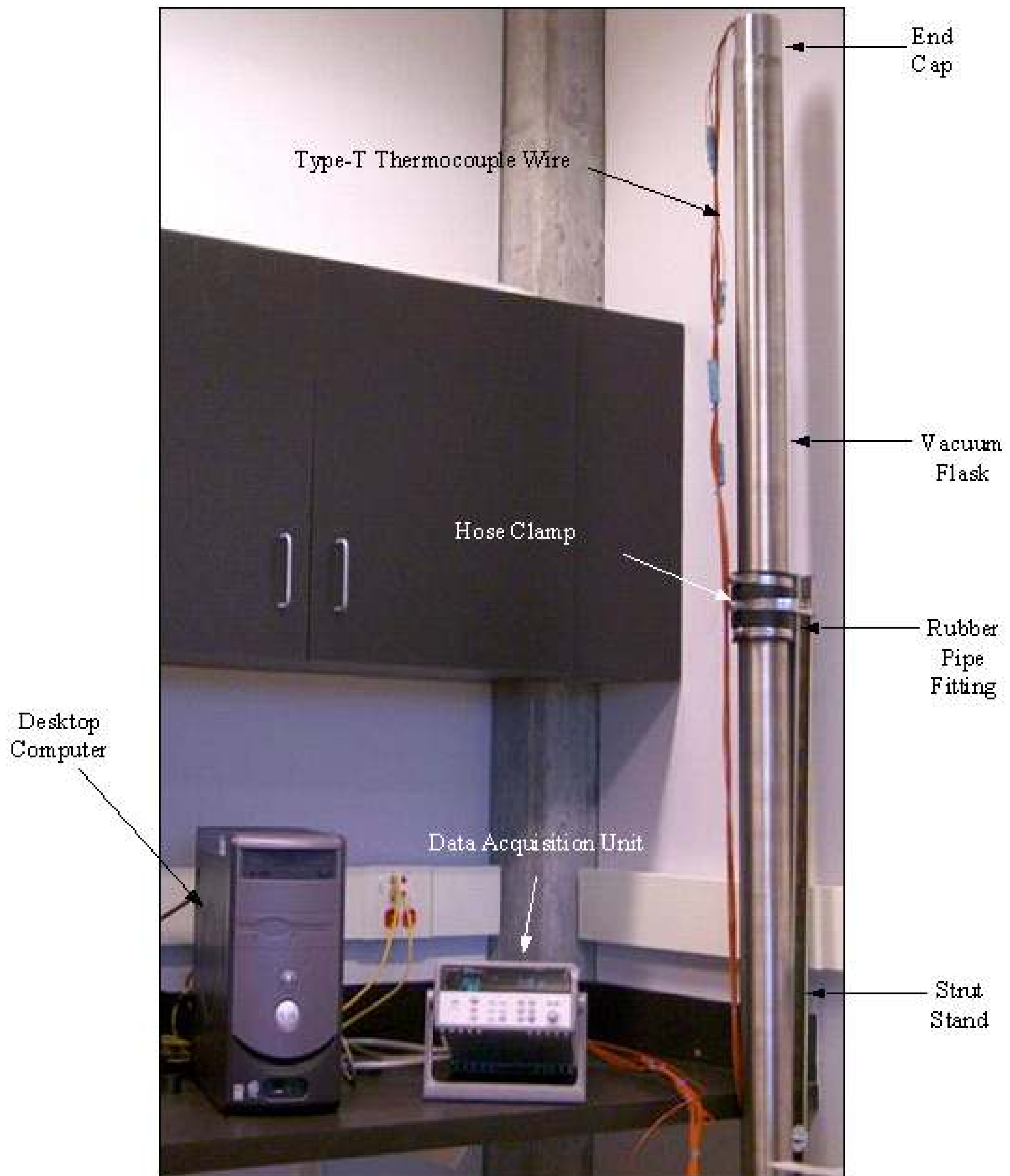


**Figure 6.3:** Overview of Setup for Vacuum Flask Performance Experiments

**Table 6.1:** Apparatus Used in Vacuum Flask Thermal Performance Experiments

| ITEM | DESCRIPTION |
|---|---|
| Vacuum flask | Vacuum Barrier Corp., S/N D-101 |
| Vacuum flask end cap | Manufactured by Halliburton from PEEK |
| Thermocouples | Omega, Type-T, Part# 5TC-TT-T-24-36 |
| Thermocouple connectors | Omega, Part# HMP-T-MF |
| Wooden dowels | 3/8" diam X 48" long |
| Radial spacers | Custom machined from aluminum |
| Stock pot | Calphalon, 12 qt. capacity, Model 812-12QT |
| Hot plate | Barnstead, Model HP46825, S/N 1070030293064 |
| Drill pump | Flotec, Model FPDMP215A |
| Hand drill | Black & Decker, S/N 9541-F |
| Roller stand | Habor Freight Tools, Item# 40067 |
| 3" Rubber fitting | Fernco, Inc., SBCCI-7289, BOCA-79-23 |
| 3" Rubber end cap | Fernco, Inc., SBCCI-8368, BOCA-82-57 |
| 1 5/8" Strut | Superstrut, Model A-1200-HS |
| Post base | B-Line, Part# B279SQ |
| Data acquisition unit | Agilent, Model 34970A, S/N MY41022085 |
| Armature multiplexer | Agilent, Model 34901A, S/N MY41005850 |
| Desktop computer | Dell, Dimension 2400, S/N HJ9JH31 |

**Table 6.2:** Procedure for Vacuum Flask Thermal Performance Experiments

1. Boil water in stock pot using hot plate.
2. Tip flask to approximately 30 degrees, supporting it with a roller stand.
3. Pump boiling water from stock pot into vacuum flask using drill pump.
4. Fill vacuum flask to brim with water.
5. Start data acquisition.
6. Insert thermocouple probe into vacuum flask.
7. Cap Vacuum flask with PEEK end cap.
8. Stand vacuum flask vertically and clamp it to strut post.
9. Log thermocouple readings for 24 hours.
10. Stop data acquisition.
11. Remove cap and thermocouple probe from vacuum flask.
12. Pour water from vacuum flask into sink.
13. Stand vacuum flask vertically and clamp it to strut post.
14. Let vacuum flask cool and dry for 24 hours.

## *6.4 Thermocouple Probe*

A simple, yet rugged custom thermocouple probe was constructed to monitor the axial temperature distribution within the vacuum flask. This probe consists mainly of two 0.953 cm (3/8") diameter by 1.04 m (41") long wooden dowels, two custom fabricated aluminum radial spacers, and twelve, duplex insulated, type-T *Omega* thermocouples. Made from special limits of error wire, these thermocouples are accurate to ± 0.5 °C. High temperature type-T thermocouple connectors join the relatively short thermocouples to longer lengths of type-T thermocouple wire, also made from special limits of error wire.

The aluminum radial spacers, each about 7.49 cm (2.95") in diameter, center the thermocouple probe within the 7.62 cm (3") ID vacuum flask. Two high temperature O-rings on either side of these spacers prevent them from sliding along the wooden dowels. These radial spacers also contain four 1.27 cm (1/2") holes to allow water to pass easily through them. All thermocouple wires exit the vacuum flask through a 0.953 cm (3/8")diameter hole in the center of the PEEK end cap, and are directly wired to the data acquisition unit. Standard cable ties secure the thermocouples, thermocouple wires and connectors to the wooden dowels.

The main structural material for the thermocouple probe consists of wood for three main reasons. First, the poor thermal conductivity of wood reduces heat transfer in the axial direction via the thermocouple probe itself. Second, wood is an inexpensive, readily available material. Third, the wooden dowels take up negligible volume within the vacuum flask, which justifies the lumped capacitance assumption that the vacuum flask contains only water. Figure 6.4 shows an overview of the thermocouple probe, the spacing of the thermocouples along the probe, and close-up views of the aluminum radial spacers and PEEK end cap. Closely spaced thermocouples at both ends of the thermocouple probe give additional information in areas of expected high temperature gradient. Figure 6.5 shows a close-up view of the thermocouple probe,

with thermocouples T1-T12 spaced as shown. T12 is the closest thermocouple to the vacuum flask mouth.

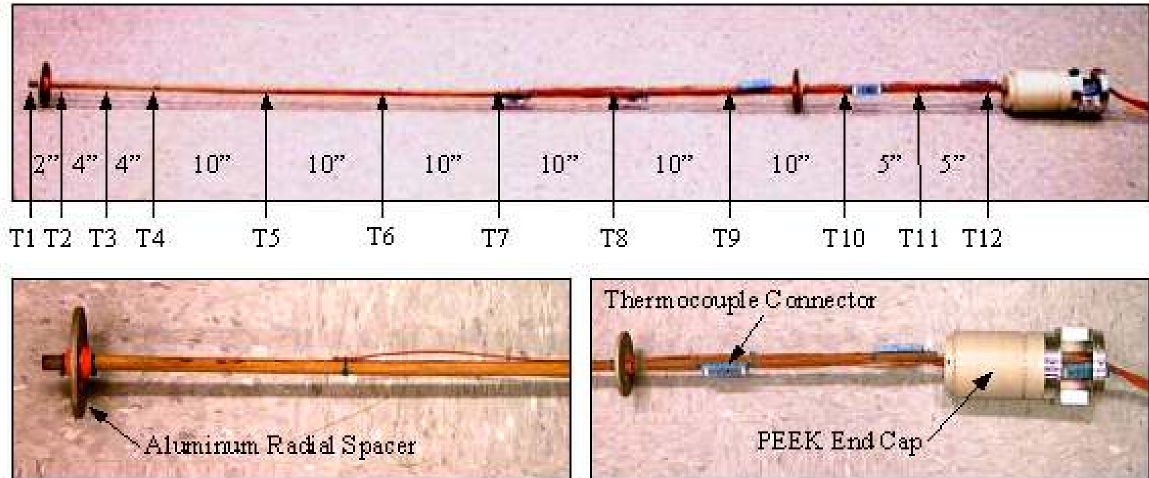


**Figure 6.4:** Custom Thermocouple Probe and Thermocouple Spacing

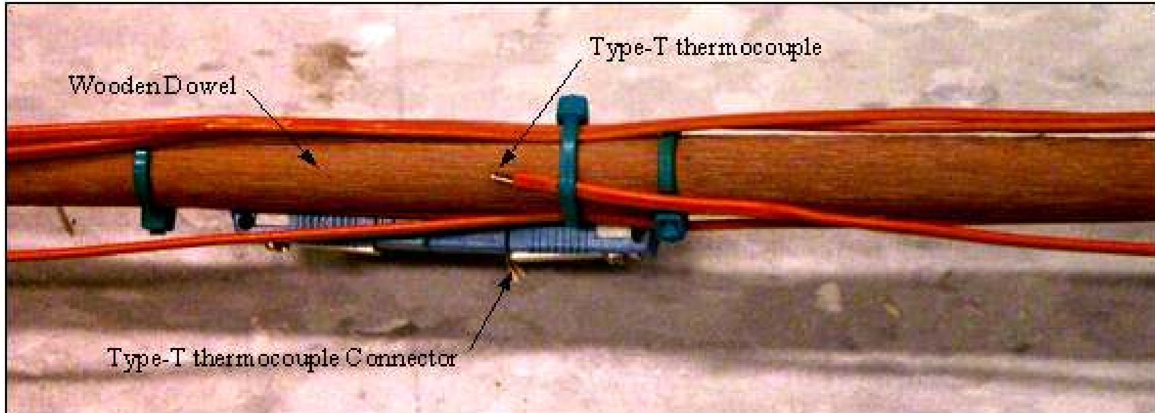


**Figure 6.5:** Close-up of Thermocouple Probe

## *6.5 Data Acquisition*

### 6.5.1 Hardware

The data acquisition hardware used for these experiments consists of an *Agilent* 34970A data acquisition/switch unit, an *Agilent* 34901A armature multiplexer

plug-in card, a standard GPIB (general purpose interface bus) cable, GPIB PCI (peripheral component interconnect) card, and a *Dell* desktop computer. All twelve thermocouples of the thermocouple probe and one for room temperature were directly wired to screw terminals 101 - 113 on the 34901A multiplexer module. The 34970A data acquisition/switch unit communicates with the desktop computer via the GPIB cable/interface, and scans all thirteen thermocouples at ten second intervals for twenty-four hours. Figure 6.6 shows the physical connections for the data acquisition hardware of this experiment in schematic form.

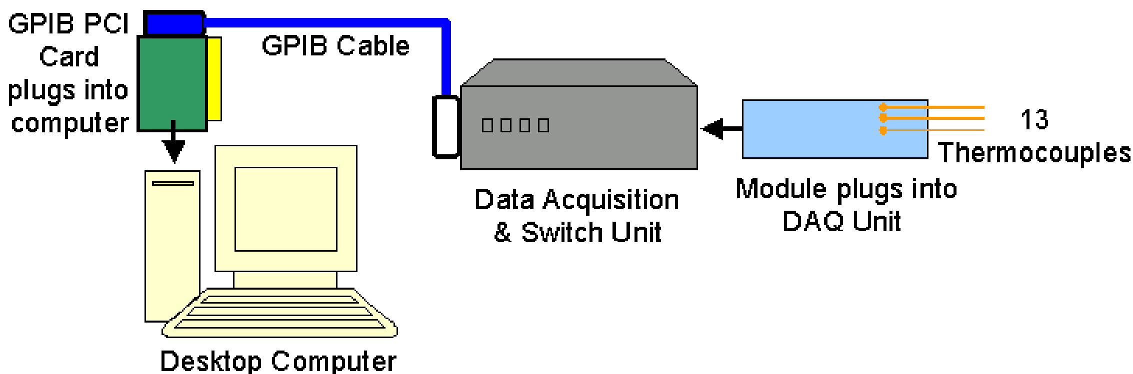


**Figure 6.6:** Schematic of Data Acquisition Hardware Used to Test Vacuum Flask

### 6.5.2 Software

*Agilent Benchlink Data Logger* software, a Windows® based program, comes packaged with the 34970A data acquisition/switch unit. *Benchlink* features a friendly user interface that resembles a spreadsheet for test configuration. It was used to acquire and record incoming water temperature measurements from the data acquisition/switch unit at ten second intervals for twenty-four hours, and to perform real-time display of these data. The software excels when applied to experiments that require only data logging and display, such as for the vacuum flask thermal performance experiments. However, *Benchlink* lacks the programming flexibility and

functionality needed to implement a control system. Hence all other experiments described in this thesis used LabVIEW™ 7 Express software from *National Instruments* for data acquisition and control.

## 6.6 Results and Discussion

The vacuum flask thermal performance experiments were repeated five times. The data for the first experiment are labelled *Run A*, the second *Run B*, and so on through *Run E*. This section includes representative data plots for *Run A* and *Run B*, and Appendix B presents the remaining data for *Run C* through *Run E* in graphical form.

Figure 6.7 gives the temperature variation in the axial direction of the vacuum flask at several time intervals for *Run A*. The 80 inch mark corresponds to the open end of the vacuum flask. As expected, the temperature gradient within the vacuum flask at any given time remains relatively flat for the duration of the experiment.

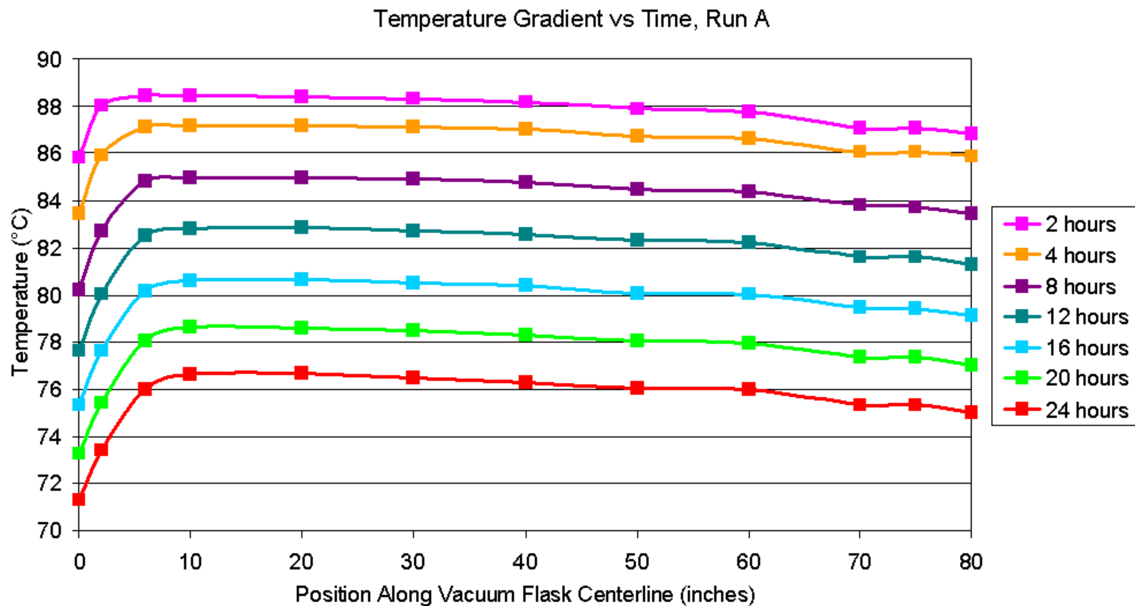


**Figure 6.7:** Axial Temperature Gradient in Vacuum Flask vs Time, *Run A*

Figure 6.8 presents a similar distribution for *Run B*. These results validate the use of the lumped capacitance method to determine the overall heat transfer coefficient for the vacuum flask, $U$, without significant loss in accuracy.

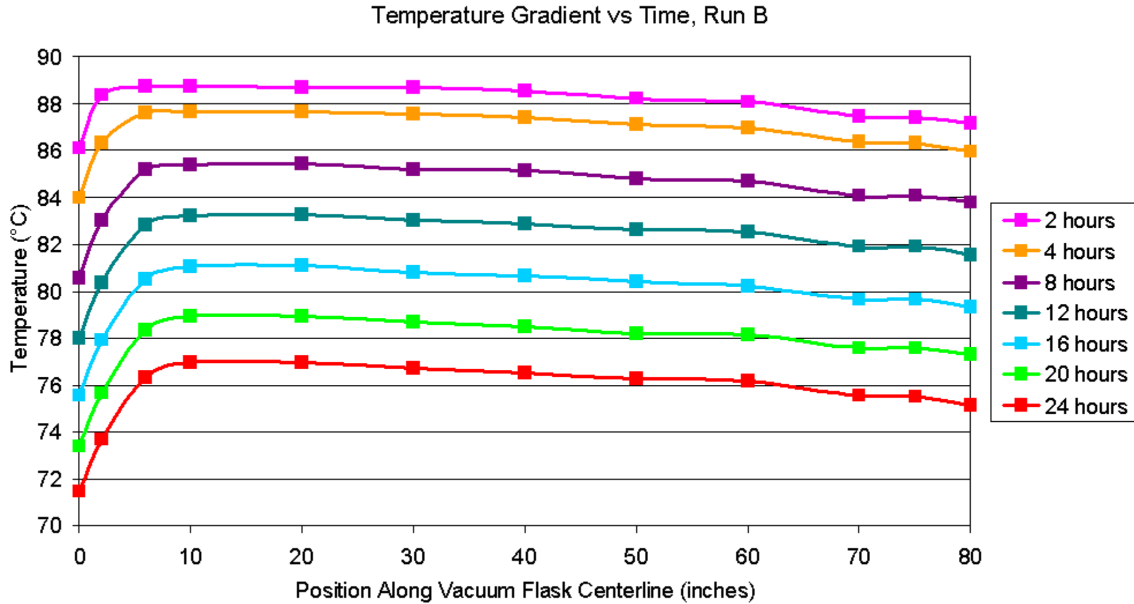


**Figure 6.8:** Axial Temperature Gradient in Vacuum Flask vs Time, *Run B*

Figure 6.9 shows the change in average water temperature within the vacuum flask versus time for *Run A*. The average temperature within the flask dropped about 15 °C over 24 hours. An exponential best-fit line, shown in magenta, matches these data with a correlation coefficient of 0.9993, approaching the maximum value of one. Initially at room temperature, the stainless steel vacuum flask rapidly heats up as it fills with boiling water. The water and stainless steel vacuum flask quickly reach a new quasi-equilibrium temperature several degrees below the boiling point of water, which explains the initial temperature of 90 °C. Similar results for *Run B* are shown in Figure 6.10.

Using the initial temperature within the vacuum flask, the exponential best-fit equation for the average temperature versus time, and Equation 6.1, one can solve

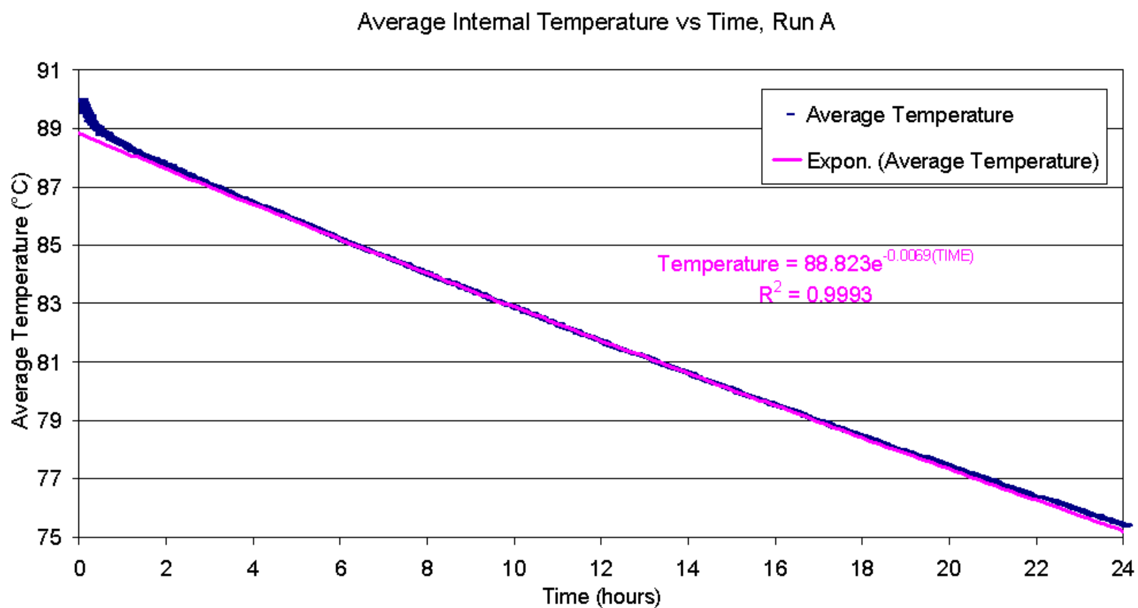


**Figure 6.9:** Average Internal Vacuum Flask Temperature vs Time, *Run A*

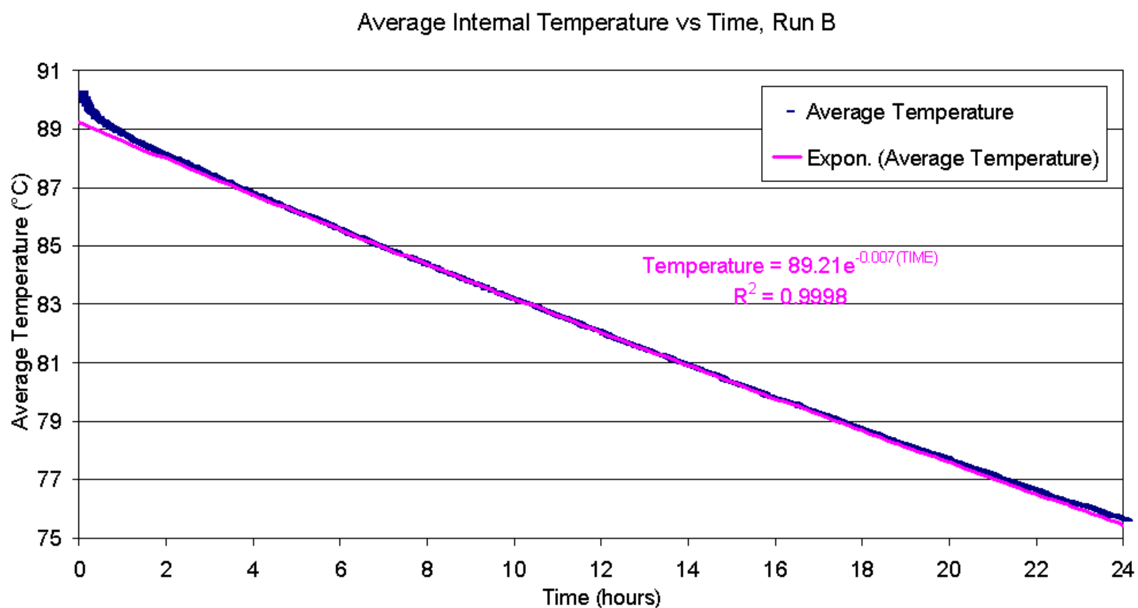


**Figure 6.10:** Average Internal Vacuum Flask Temperature vs Time, *Run B*

for the overall heat transfer coefficient of the vacuum flask. Table 6.3 summarizes this calculation for all five runs, includes calculations of uncertainty, and gives the correlation coefficient of the exponential best-fit line for each run. The average vacuum flask heat transfer coefficient, $U$, for all five runs equals 0.198 $W/m^2{\cdot}K \pm$ 0.00707 $W/m^2{\cdot}K$. This agrees well with the value quoted by the vacuum flask manufacturer, $U = 0.2$ $W/m^2{\cdot}K$. Appendix D describes the uncertainty analysis in detail.

**Table 6.3:** Results from Vacuum Flask Thermal Performance Experiments

| Run | $U$, $W/m^2{\cdot}K$ | Uncertainty $\pm$ $W/m^2{\cdot}K$ | Uncertainty $\pm$ % | Correlation Coefficient |
|---|---|---|---|---|
| A | 0.196 | 0.00706 | 3.60% | 0.9993 |
| B | 0.197 | 0.00699 | 3.54% | 0.9998 |
| C | 0.197 | 0.00712 | 3.62% | 0.9998 |
| D | 0.199 | 0.00706 | 3.55% | 0.9998 |
| E | 0.199 | 0.00712 | 3.57% | 0.9998 |
| Average: | 0.198 | 0.00707 | 3.58% | 0.9997 |

# CHAPTER 7

# TUBE-SIDE HEAT TRANSFER EXPERIMENTS

## *7.1 Purpose*

The objective of these experiments is to determine whether HiTRAN® matrix elements provide enhanced heat transfer compared to a plain tube, and if so, to quantify the enhancement. One can determine a performance difference by comparing the heat transfer coefficients, $h$, for tubing with and without HiTRAN® matrix elements. For an added basis of comparison, the heat transfer literature provides theoretical heat transfer coefficients for a plain tube under specific boundary and flow conditions [16]. An accurate determination of the heat transfer coefficient for tubing with HiTRAN® matrix elements allows one to optimize the size of the heat exchanger assembly, and provides crucial data for modelling efforts.

## *7.2 Approach*

Making measurements of forced-convection heat transfer coefficients within a tube requires careful control of the experimental conditions. Holman describes a method and experimental setup to determine forced-convection heat transfer coefficients for various fluids [15]. The current experiments employ a similar experimental setup as prescribed by Holman, but are slightly modified to make use of equipment that was most readily available. Figure 7.1 gives a schematic of the apparatus used to determine the forced-convection heat transfer coefficients in smooth tubes with and without HiTRAN® matrix elements.

Assuming negligible losses through the insulation, an energy balance around the

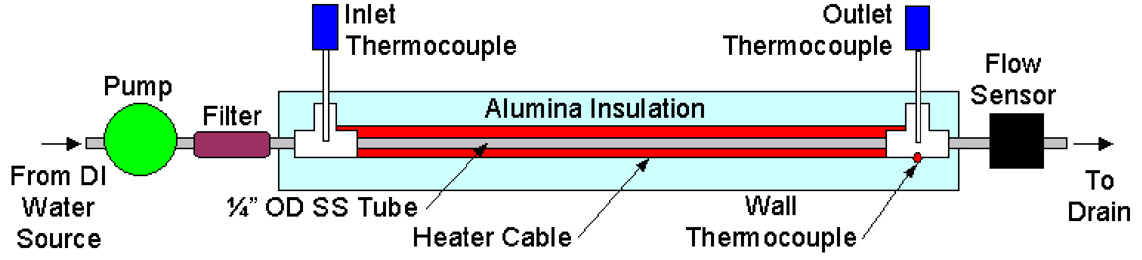


**Figure 7.1:** Schematic of Setup used in Tube-Side Heat Transfer Experiments

tube yields

$$q = \dot{m}c_p\left(T_{m,o} - T_{m,i}\right) \tag{7.1}$$

where $q$ is the rate of heat transferred to the water, $\dot{m}$ equals the flow rate of water through the tube, $c_p$ is the specific heat of water, $T_{m,o}$ is the mean water temperature at the tube outlet, and $T_{m,i}$ represents the mean water temperature at the tube inlet. Equation 7.1 is a general expression that applies regardless of the flow rate or thermal conditions along the tube surface. For flow in a circular tube, the following expression gives the Reynolds number

$$Re = \frac{4\dot{m}}{\pi D\mu} \tag{7.2}$$

where $Re$ is the Reynolds number, $\dot{m}$ equals the flow rate of water through the tube, $D = 0.004826$ m is the inner diameter of the tube, and $\mu = 9.59\times10^{-4}$ N·s/m$^2$ is the dynamic viscosity of water. The maximum flow rate through the tube during these experiments equals 250 mL/min, or $\dot{m} = 0.00416$ kg/s. Plugging this value into Equation 7.2, $Re = 1144$. This is well below the onset of turbulence, which occurs at $Re \approx 2300$. Therefore, water flow is laminar for these experiments.

Assuming the heater cable provides a uniform heat flux on the tube surface, and that water flow within the tube is laminar and fully-developed, then the local convection heat transfer coefficient within the tube is constant, and Newton's Law of Cooling applies at any axial position, including the tube outlet

$$q = hA\left(T_{s,o} - T_{m,o}\right) \tag{7.3}$$

where $q$ is the rate of heat transferred to the tube, $T_{m,o}$ is the mean water temperature at the tube outlet, $T_{s,o}$ represents the outlet tube surface temperature, $A$ is the total inside surface area of the tube, and $h$ is the convective heat transfer coefficient [16]. Equating Equation 7.1 to Equation 7.3 and solving for $h$ gives

$$h = \frac{\dot{m}c_p\left(T_{m,o} - T_{m,i}\right)}{A\left(T_{s,o} - T_{m,o}\right)} \tag{7.4}$$

Therefore, by measuring the water flow rate, $\dot{m}$, the mean inlet water temperature, $T_{m,i}$, the mean outlet water temperature, $T_{m,o}$, and the tube surface temperature at the outlet, $T_{s,o}$, one can determine the convective heat transfer coefficient, $h$, for the case of a tube with HiTRAN® matrix elements, and a plain tube configuration.

## *7.3 Apparatus and Procedure*

The main test section consists of a meter long seamless tube, tightly wrapped with heater cable and several layers of alumina insulation. Duct tape surrounds the entire test section to minimize contact with the alumina fibers of the insulation. Thermocouple probes monitor the mean inlet and outlet temperatures. A pump draws deionized water from a nalgene container and pumps it through an in-line filter prior to entering the test section. The water heats up as it passes through the test section, and exits into a flow sensor. The flow sensor continuously measures the flow rate of the water before it drains into a twelve quart pot. Figure 7.2 gives an overview of the experimental setup.

The 0.635 cm (1/4") OD tube consists of 304 stainless steel, and has a 0.711 mm (0.028") wall thickness. In the first set of tests, the stainless steel tube also contained a meter long HiTRAN® matrix element. For the second set of tests, the element was removed, leaving just the plain tube. Two stainless steel tee fittings swage to both ends of the test section. These fittings allow the introduction of thermocouple probes to measure the inlet and outlet temperature of the water as it flows through the test section. Each 15.24 cm (6") thermocouple probe consists of

**Figure 7.2:** Overview of Setup for Tube-Side Heat Transfer Experiments

a type-T thermocouple embedded within a 0.318 cm (1/8") diameter stainless steel sheath. After passing through a 0.318 cm (1/8") hole drilled through the center of a 1/8-MNPT brass plug, high temperature epoxy seals and secures the thermocouple probes in place. Wrapped with Teflon tape, the brass plugs provide the necessary fluidic seal at the branch of each tee. The tip of each thermocouple probe protrudes well into the water stream to ensure accurate temperature measurement.

The heater cable used to heat the test section consists of highly flexible resistive wire insulated with high temperature silicone, and plugged into a standard 120 Volt wall outlet. The unit includes a dial-type power controller, and provides up to 750 Watts of heating. For all tests, the power was set to about 5% of the maximum output. The *Micropump* gear pump, borrowed from the prototype of the thermal management system, was used to pump deionized water through the test section. The gear pump provides negligible pulsation at low flow rates. Figure 7.3 illustrates the upstream end of the test section, including the pump, heater cable controller, and inlet thermocouple probe.

The *McMillan Co.* turbine-style flow meter described in Chapter 5 was used to measure the flow rate through the test section. The flow meter inlet attaches to the test section using *Swagelok* compression fittings, and a drain hose attaches to the flow

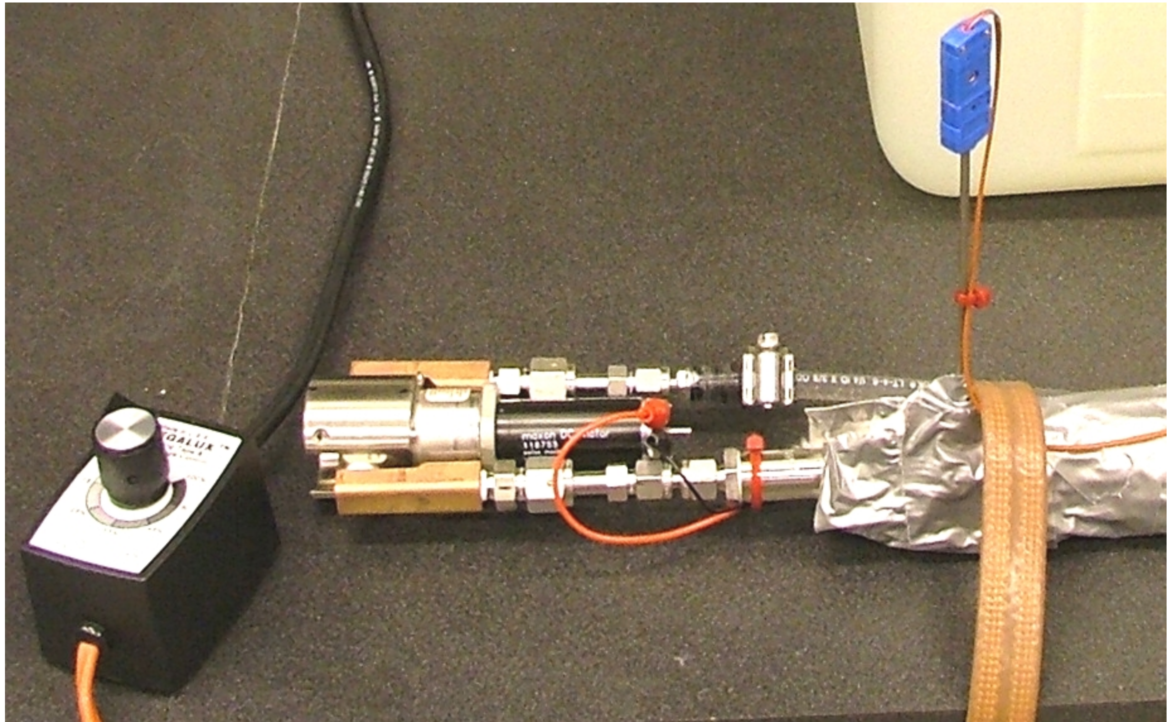

**Figure 7.3:** Close-up of Pump, Inlet Thermocouple, and Heater Controller

meter outlet to direct spent, heated water into a stock pot. A two micrometer filter upstream from the test section prevents particulates from fouling the flow meter, and considerably dampens the flow, which reduces pulsation within the test section and flow meter. Figure 7.4 shows the downstream end of the test section, including the black flow sensor, and outlet thermocouple probe.

The test case with HiTRAN® matrix elements began by applying power to the flow sensor, and activating the data acquisition and control system. Next, the heater cable was plugged into the wall outlet and switched on. The pump was activated to a high flow rate to purge any air bubbles in the test section and feed line. Then, the flow rate through the test section was varied from 50 to 250 mL/min by adjusting voltage to the pump from 5 to 15 Volts in 1 Volt increments. For each pump voltage setting between 5 Volts and 15 Volts, the system was first allowed to reach steady state, and then ten to five minutes of temperature and flow rate readings were

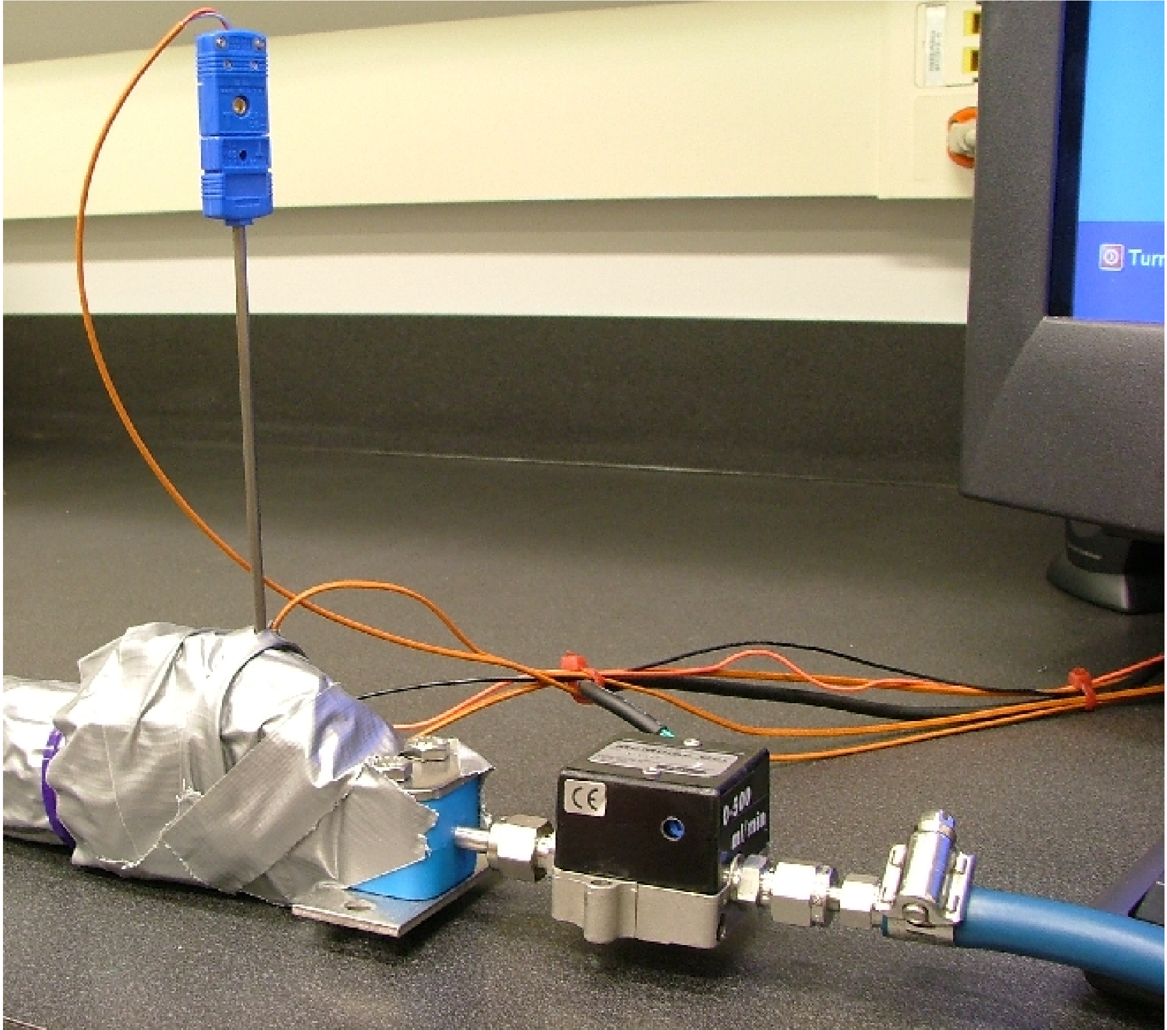


**Figure 7.4:** Close-up of Flow Sensor, and Outlet Thermocouple Probe

logged. Deionized water was added to the source container as needed to maintain nearly full fluid levels. After logging data for the 15 Volt pump voltage setting, data acquisition ceased. Finally, the HiTRAN® matrix element was removed from the stainless steel tube, and the process was repeated for the plain tube case. Table 7.1 itemizes the apparatus of these experiments, and includes a detailed description, such as manufacturer, model number, serial number, or part number. Table 7.2 gives the procedures used during each experiment, both with and without HiTRAN® matrix elements.

**Table 7.1:** Apparatus Used in Tube-Side Heat Transfer Experiments

| ITEM | DESCRIPTION |
|---|---|
| 1/4" HiTRAN insert | Cal Gavin, Co., stainless steel, 1 meter long |
| 304 Stainless tube | 1/4" OD, 1 meter long, 0.028" wall thickness |
| 316 Stainless tee fittings | Swagelok, Part# SS-400-3TTF |
| Nalgene container | 5 gallon capacity, Cat# 2240 |
| Heater Cable | Omega, S/N# 45037/1, Part# HTWC101-010 |
| Alumina Insulation | McMaster-Carr, Part# 9379K93 |
| Feed Hose | Swagelok, 3/8" OD, Vinyl, Part# LT-4-6 |
| Drain Hose | Swagelok, 1/4" push-on, Part# PB-4 |
| Duct Tape | Nashua 398 |
| Flow sensor | McMillan Co., Model 104-5, S/N 1107-5 |
| 2 Micron filter | Swagelok, Part# SS-4F-2 |
| Thermocouple probes | Omega, Type-T, Part# TMQSS-125G-6 |
| Thermocouples | Omega, Type-T, Part# 5TC-TT-T-24-36 |
| Thermocouple connectors | Omega, Type-T, Part# HMP-T-MF |
| Stock pot | Calphalon, 12 qt. capacity, Model 812-12QT |
| Data acquisition unit | Agilent, Model 34970A, S/N MY41022085 |
| Armature multiplexer | Agilent, Model 34901A, S/N MY41005850 |
| DC Power Supply | Agilent, Model E3631A, S/N MY40021108 |
| PCI GPIB Interface | Agilent, Model 82350B |
| Desktop computer | Dell, Dimension 2400, S/N HJ9JH31 |

**Table 7.2:** Procedure for Tube-Side Heat Transfer Experiments

1. Start power to flow sensor.
2. Start data acquisition.
3. Turn on heater cable.
4. Start pump.
5. Bleed any air bubbles from entire tubing run.
6. Allow system to reach steady state.
7. Log temperature & flow data for 15 to 20 minutes.
8. Repeat steps 6 & 7 for each voltage setting on the pump.
9. Fill deionized water container as necessary.
10. Stop data acquisition.

## 7.4 *Data Acquisition*

### 7.4.1 Hardware

The data acquisition (DAQ) hardware used for these experiments consists of an *Agilent* 34970A data acquisition/switch unit, an *Agilent* E3631A DC power supply, an *Agilent* 34901A armature multiplexer plug-in card, two standard GPIB (general purpose interface bus) cables, a GPIB PCI (peripheral component interconnect) card, and a *Dell* desktop computer. The three thermocouples and flow meter voltage signal wires were directly wired to screw terminals 101 - 104 on the 34901A multiplexer module, which plugs into the data acquisition/switch unit. The DC power supply features three outputs: +6 Volts, 5 Amps; +25 Volts, 1 Amp; and -25 Volts, 1 Amp. The -25 Volt output powered the flow sensor, and the +25 Volt output was used to power the pump. Both the data acquisition/switch unit and the power supply communicate with the desktop computer via GPIB. Figure 7.5 gives a schematic that shows the physical connections for the data acquisition hardware of this experiment.

### 7.4.2 Software

A custom data acquisition and control program, called *Hitran*, was written for the these experiments using LabVIEW™ 7 Express software from *National Instruments*. This program communicates with the *Agilent* 34970A data acquisition/switch unit to monitor and acquire all measurements. The program also controls the *Agilent* E3631A DC power supply via GPIB, which allows direct adjustment of the pump voltage from the user interface rather than manually from the power supply. The user interface provides real-time numerical and graphical displays of all data, including temperature readings, flow rate readings, and the volts, current, and power set to the pump, and elapsed time. Appendix C contains the block diagram, or underlying code for the *Hitran* LabVIEW™ program. Figure 7.6 shows the program user interface for the data acquisition and control program, *Hitran*.

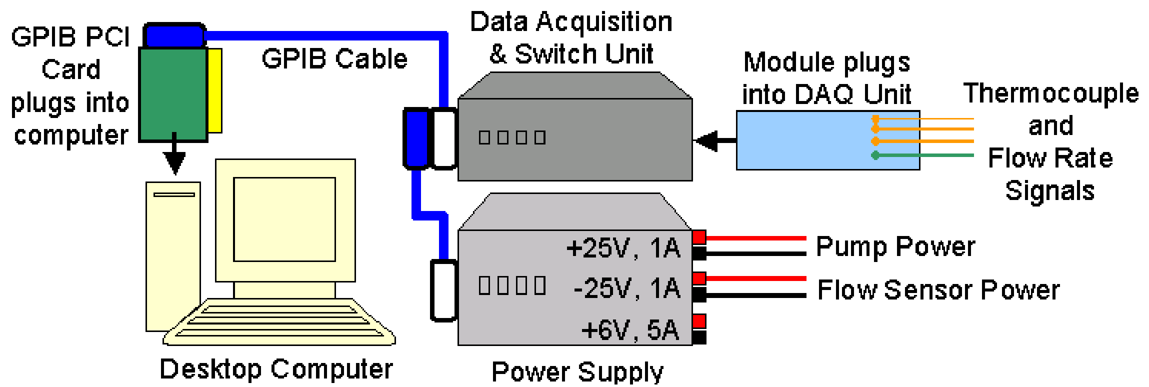


**Figure 7.5:** Schematic of DAQ Hardware for Heat Transfer Experiments

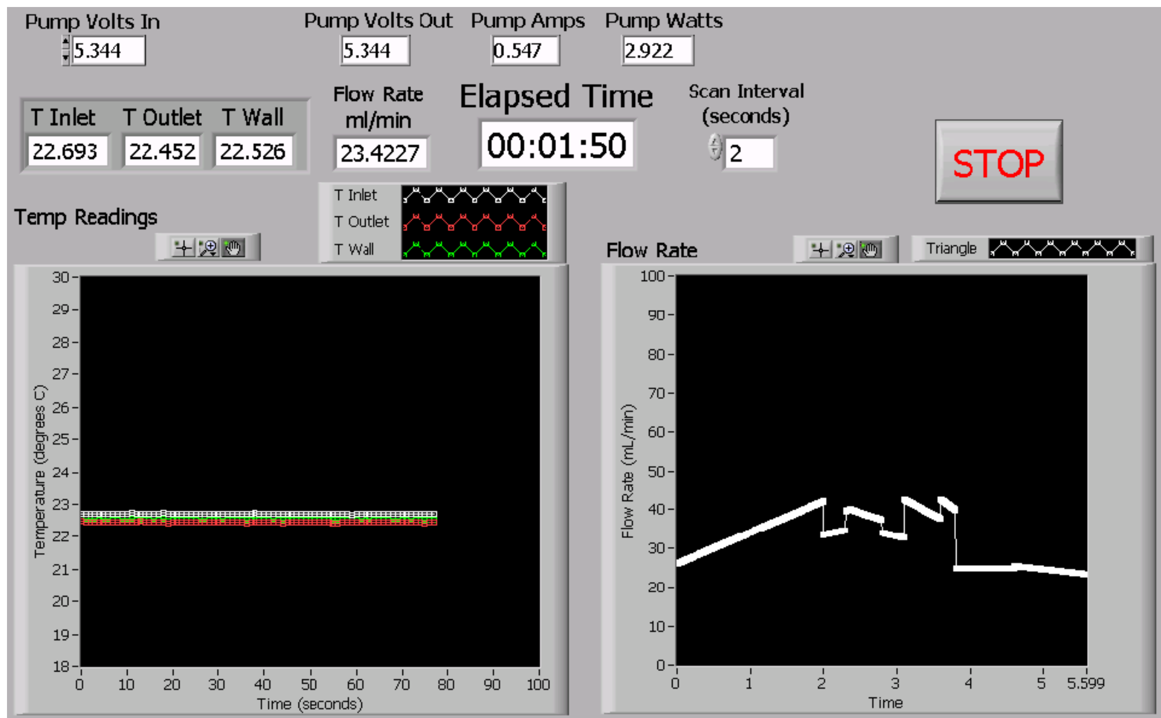


**Figure 7.6:** *Hitran* User Interface

## 7.5 Results and Discussion

Once switched on, the data acquisition program continuously monitored and recorded temperature and flow rate readings at two second intervals for the duration of the test, resulting in well over 6800 readings per channel for the test case with HiTRAN®. For the plain tube case, over 7200 readings per channel were recorded.

At each pump voltage setting from 5 Volts to 15 Volts, the mean and standard deviation of over a hundred readings were calculated after the system reached steady state. Time to steady state was about five minutes for each pump voltage setting. Chauvenet's criterion, as described in Chapter 5, was applied to each data set. This criteria provided a statistical means to exclude anomalous data points caused by air bubbles in the test section. These air bubbles, produced by cavitation at the pump inlet, caused the flow meter's turbine to either stall or spin freely, resulting in irregular flow rate readings.

A new mean and standard deviation were calculated for each measurement at a given pump voltage setting. Finally, the convective heat transfer coefficient, $h$, for both the case of a tube with HiTRAN® and a plain tube was calculated based on average values for inlet temperature, outlet temperature, wall temperature, and flow rate.

The average HiTRAN® heat transfer coefficient over all flow rates equals 648.6 $W/m^2{\cdot}K \pm 86.2\ W/m^2{\cdot}K$. For the plain tube case, the average heat transfer coefficient over all flow rates equals 553.3 $W/m^2{\cdot}K \pm 58.3\ W/m^2{\cdot}K$. This agrees well with the theoretical heat transfer coefficient for a plain tube, calculated with a Nusselt number of 4.36, which equals 542 $W/m^2{\cdot}K$. Chapter 8 contains additional interpretations and recommendations based on these data. Appendix D describes the analysis used in this thesis to estimate experimental uncertainty, and gives a representative example.

Table 7.3 summarizes the HiTRAN® heat transfer coefficient results. Table 7.4 gives similar results for the plain tube case. Both tables include average flow

rate, power to the pump, and heat transfer coefficients with uncertainty for pump voltage settings between 5 Volts and 15 Volts. Figure 7.7 presents these results in graphical form, including error bars. As expected, the heat transfer coefficients do not vary significantly with flow rate for either the case of tubing with HiTRAN® matrix elements, or the plain tube case.

**Table 7.3:** Heat Transfer Coefficient Results for Tube with HiTRAN®

| Voltage on Pump | Power to Pump | Average Flow Rate | $h$, | Uncertainty | Uncertainty |
|---|---|---|---|---|---|
| Volts | Watts | kg/s × $10^3$ (mL/min) | W/m²·K | ± W/m²·K | ± % |
| 5.0 | 0.407 | 0.79 (47.6) | 655.8 | 87.4 | 13.3% |
| 6.0 | 0.545 | 0.99 (59.6) | 640.4 | 85.1 | 13.2% |
| 7.0 | 0.704 | 1.36 (81.7) | 646.9 | 85.9 | 13.2% |
| 8.0 | 0.896 | 1.77 (106.5) | 653.4 | 86.8 | 13.2% |
| 9.0 | 1.068 | 2.11 (127.1) | 648.5 | 86.3 | 13.3% |
| 10.0 | 1.312 | 2.35 (141.1) | 649.5 | 86.3 | 13.3% |
| 11.0 | 1.552 | 2.76 (166.0) | 653.0 | 86.9 | 13.3% |
| 12.0 | 1.806 | 3.08 (185.0) | 650.9 | 86.6 | 13.3% |
| 13.0 | 2.062 | 3.44 (206.8) | 645.8 | 85.6 | 13.2% |
| 14.0 | 2.334 | 3.78 (227.4) | 645.2 | 85.9 | 13.3% |
| 15.0 | 2.628 | 4.10 (246.8) | 645.7 | 85.9 | 13.3% |
| | | Average: | 648.6 | 86.2 | 13.3% |

**Table 7.4:** Heat Transfer Coefficient Results for Plain Tube

| Voltage on Pump | Power to Pump | Average Flow Rate | $h$, | Uncertainty | Uncertainty |
|---|---|---|---|---|---|
| Volts | Watts | kg/s × $10^3$ (mL/min) | W/m$^2$·K | ± W/m$^2$·K | ± % |
| 5.0 | 0.350 | 0.92 (55.3) | 518.6 | 54.4 | 10.5% |
| 6.0 | 0.466 | 1.06 (63.5) | 527.9 | 55.6 | 10.5% |
| 7.0 | 0.607 | 1.50 (90.1) | 536.2 | 56.3 | 10.5% |
| 8.0 | 0.768 | 1.76 (105.8) | 549.8 | 58.0 | 10.5% |
| 9.0 | 0.965 | 2.09 (125.5) | 565.8 | 59.7 | 10.5% |
| 10.0 | 1.176 | 2.38 (143.3) | 567.8 | 60.2 | 10.5% |
| 11.0 | 1.415 | 2.70 (162.5) | 566.6 | 59.6 | 10.5% |
| 12.0 | 1.677 | 3.11 (187.3) | 569.7 | 60.1 | 10.5% |
| 13.0 | 1.926 | 3.45 (207.4) | 535.3 | 56.2 | 10.5% |
| 14.0 | 2.188 | 3.77 (226.8) | 568.8 | 60.1 | 10.5% |
| 15.0 | 2.487 | 4.16 (250.0) | 569.0 | 60.3 | 10.6% |
| | | Average: | 553.3 | 58.3 | 10.5% |

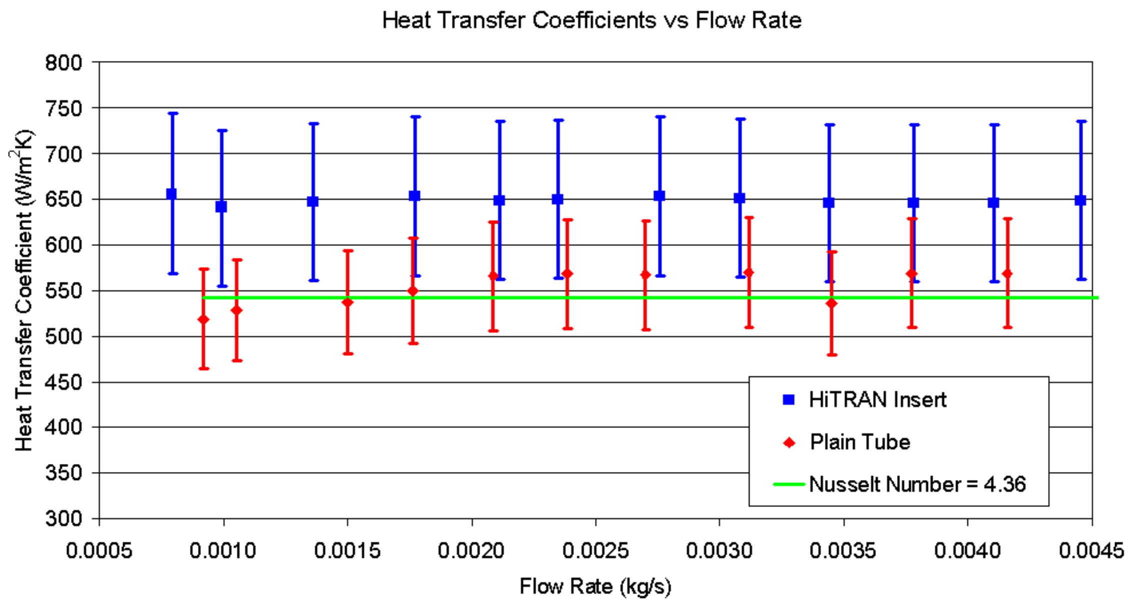


**Figure 7.7:** Results for Heat Transfer Coefficient vs Flow Rate

# CHAPTER 8

# SUMMARY AND CONCLUSIONS

A full-scale prototype thermal management system for cooling well-logging electronics in a 200 °C environment was designed, built, and tested. The prototype consists mainly of a vacuum flask, phase change material (PCM), and a pumped liquid flow loop. The vacuum flask insulates the electronics and bulk of the thermal management system from the high ambient temperature. The PCM stores the heat generated by the electronic components as it heats up and melts. The pumped liquid flow loop consists mainly of a gear pump, an aluminum cold plate, a stainless steel fluid expansion cylinder, and a stainless steel coiled heat exchanger surrounded by the PCM. This closed, recirculating flow loop provides an efficient thermal path between the electronic components and the PCM. Attached to the electronic components via thermal interface material, the cold plate transfers heat dissipated by the components to the coolant, deionized water. The pump circulates the coolant to the coiled, double-helix heat exchanger. The heat exchanger, which takes up only 4% of the available volume within the PCM container, efficiently transfers heat from the cooling fluid to the PCM. Within the heat exchanger and cold plate, a tube-side heat transfer device enhances heat transfer to and from the cooling fluid.

Several main and ancillary experiments were carried out to evaluate the performance of the prototype thermal management system. The main experiments consist of four sets of tests. These include two baseline tests, four tests in which the thermal test chips dissipate 18 Watts at various flow rates, four tests in which the coolant circulates at 0.00114 kg/s (69 mL/min) at various chip power dissipations, and one test

with a total chip power of 18 Watts in which a proportional control system varies the flow rate through the flow loop. In the main experiments, kapton resistive heaters embedded in quad-flat-packages thermally and mechanically simulate the well-logging electronic components, two stainless steel thermocouple probes monitor the temperature of the PCM, and a custom forced convection oven heats the prototype to 200 °C. The ancillary, or supporting experiments include experiments to develop a correlation between coolant flow rate and voltage supplied to the coolant pump, several vacuum flask thermal insulation performance experiments, and experiments to determine whether HiTRAN® matrix elements provide enhanced tube-side heat transfer compared to a plain tube, and if so, to quantify the enhancement.

Baseline tests of the prototype provide a basis of comparison for all other tests, and resemble a common industry approach to thermal management of electronics in wireline logging tools. In the first baseline test, the highest chip temperature exceeds 95 °C in 4 hours, 2 minutes, and in the second baseline test, 3 hours, 50 minutes. With the pump off, the high temperature gradient between the thermal test chips and PCM indicates a high thermal resistance exists between the two. Some heat reaches the PCM from the thermal test chips and vacuum flask mouth via conduction, but not enough to initiate melting of the PCM.

In all four experiments at a constant chip power of 18 Watts, and various constant flow rates, the prototype thermal management system maintains the highest chip case temperature below 95 °C for at least 20 hours, 32 minutes. This represents more than a factor of five improvement over the baseline tests. Beyond 95 °C, a control system varies flow rate, extending the time the chip case temperatures remain below 100 °C to 25 hours, 6 minutes in the best case. Results also indicate an optimal coolant flow rate exists that maximizes the time the chips remain below 95 °C. For the optimal coolant flow rate of 0.00114 kg/s (69 mL/min), the highest chip case temperature remains below 95 °C for 23 hours, 43 minutes. This flow rate most

likely corresponds to the highest efficiency of the pump motor for the particular pressure drop through the flow loop, thereby minimizing extra heat introduced into the system via the pump. If higher flow rates are required by future iterations of this thermal management system, then the pump motor should be selected such that it is most efficient at the optimal flow rate. A gear pump inductively coupled to a high temperature motor outside the vacuum flask would reduce the heat input by the pump even further.

The four experiments carried out at constant flow rate, and various test chip power dissipations suggest an exponential relationship exists between the total time the chips remain below 95 °C, and total chip power dissipation. This correlation could be used to estimate the total downhole time for other chip power dissipations using the thermal management system. These data also provide a means through which other researchers in this work can validate their computer modelling efforts of the thermal management system.

In the variable flow experiments, a proportional LabVIEW™ control program monitors the highest chip case temperature, and adjusts the power to the pump to maintain the temperature around 95 °C. Controlled by this program, the prototype maintained the highest chip case temperature below 100 °C for 24 hours, 20 minutes, which is about 46 minutes less time than running the pump at a constant flow rate of 0.00114 kg/s (69 mL/min). A more finely tuned control program may increase this time. Since an actual field device does not experience the worst-case ambient temperature of 200 °C for a full 24 hours, and may not have a constant chip power dissipation, it could benefit most from a simple control system. However, since the purpose of the control system is to minimize using the pump, and thus minimize additional heat input by the pump motor, a pump inductively coupled to a motor outside the vacuum flask would negate the need for a control system altogether.

Since the flow rate through the flow loop was not directly measured during the

main prototype tests, a set of experiments were performed to correlate flow rate with voltage supplied to the pump, which was measured during the main tests. Results show there is a linear relationship between flow rate through the flow loop and voltage supplied to the pump motor. At the optimal flow rate of 0.00114 kg/s (69 mL/min), this correlation indicates the pump draws about 0.2 Watts of power, most of which is converted to mechanical energy, and a fraction which dissipates as heat, adding to the thermal load on the PCM.

Experiments were carried out to assess the thermal insulation performance of the vacuum flask in terms of an overall heat transfer coefficient for the vacuum flask. The overall heat transfer coefficient, $U$, takes into account heat transfer via conduction, convection, and radiation through the flask, of great value to computer modelling and design of the thermal management system, and future applications of this type of vacuum flask. Averaged over five runs, the vacuum flask heat transfer coefficient, $U$, equals 0.198 W/m$^2$K $\pm$ 0.00707 W/m$^2$K, which agrees well with the value quoted by the vacuum flask manufacturer, $U = 0.2$ W/m$^2$K.

Similar experiments were performed to determine the enhanced heat transfer provided by HiTRAN® matrix elements over a plain tube, in terms of the heat transfer coefficient, $h$. Results from these experiments show that for the case of a 0.635 cm (1/4") OD tube with a wall thickness of 0.711 mm (0.028"), and HiTRAN® matrix elements, $h = 648.6$ W/m$^2$K $\pm$ 86.2 W/m$^2$K. For the plain tube case, $h = 553.3$ W/m$^2$K $\pm$ 58.3 W/m$^2$K, which agrees well with the theoretical heat transfer coefficient for a plain tube, calculated with a Nusselt number of 4.36, which equals 542 W/m$^2$·K. These data show HiTRAN® matrix elements increase the convective heat transfer coefficient over plain tubes by 17% at the cost of about 80 mW of pumping power. Depending on manufacturing costs, future design iterations of the thermal management system could make use of HiTRAN® matrix elements to optimize the size of the PCM heat exchanger, and minimize the overall thermal resistance between

the electronic components and the PCM. Other types of tube-side heat transfer enhancement devices should also be investigated in terms of increase in heat transfer coefficient, increased pumping power, and increased manufacturing cost.

Finally, several practical lessons learned from the design, fabrication, and test of the first prototype will improve future design iterations. First, during the initial prototype test, about 235 grams of PCM leaked through the brass fittings originally used to seal the thermocouple probes and flow loop tubing to the PCM container. At about 90 °C, the differential thermal expansion between the brass fittings and stainless steel tubing provided a leak path through which the PCM escaped. The brass fittings were replaced with stainless steel fittings, and over twelve full length tests were subsequently completed leak free. To reduce the possibility of leaks, future prototypes should contain all welded connections, if possible, or only fittings made from materials that match the flow loop tubing material and PCM container material. Second, after repeated use and thermal cycling, the vacuum flask came out of round. In other words, the inner diameter of the vacuum flask became more oval-shaped than circular, making it increasingly difficult to insert the PCM container into the vacuum flask, which was machined only a few thousandths of an inch smaller in diameter. PCM containers made purely for research purposes should be made with extra clearance, since they will be assembled and disassembled many times. Of course, for actual field units, this may not be necessary. Third, the double-helix design of the coiled heat exchanger presented manufacturing difficulties to the machine shop that made it. Results from the temperature gradient within the PCM suggest that a single coiled heat exchanger with a long return line from the end would have worked just as well. This single coil design is easier to manufacture, and much more common in coiled heat exchangers made from finned tubing. For a less thermally conductive PCM than *Cerrobend*, a finned tubing design might be necessary to ensure a low overall thermal resistance between the electronic components and the PCM.

# APPENDIX A

# PROTOTYPE PERFORMANCE DATA

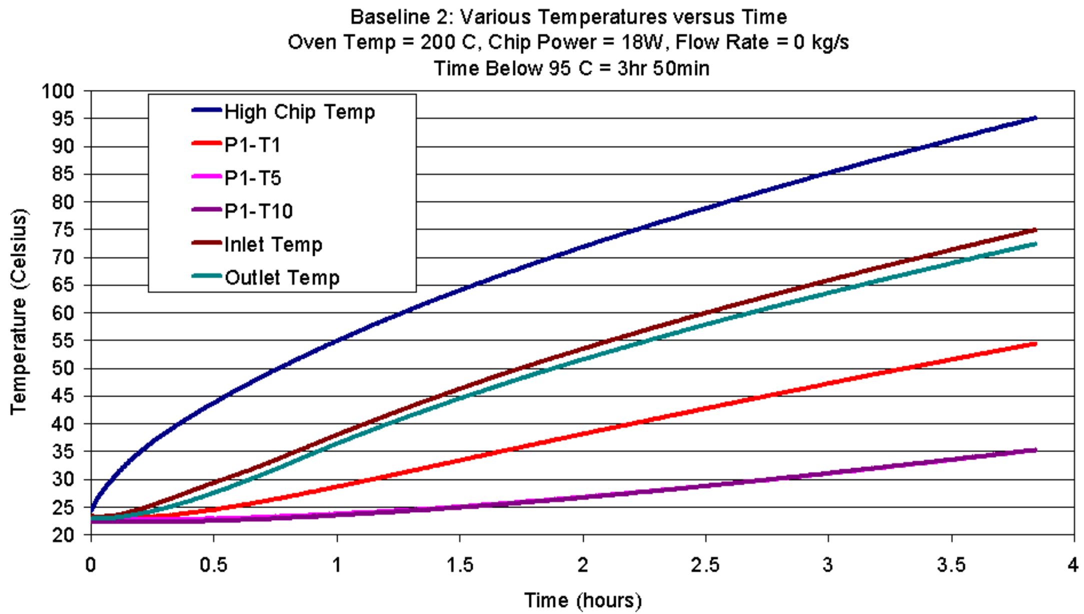


**Figure A.1:** Various Temperatures vs Time, Baseline 2

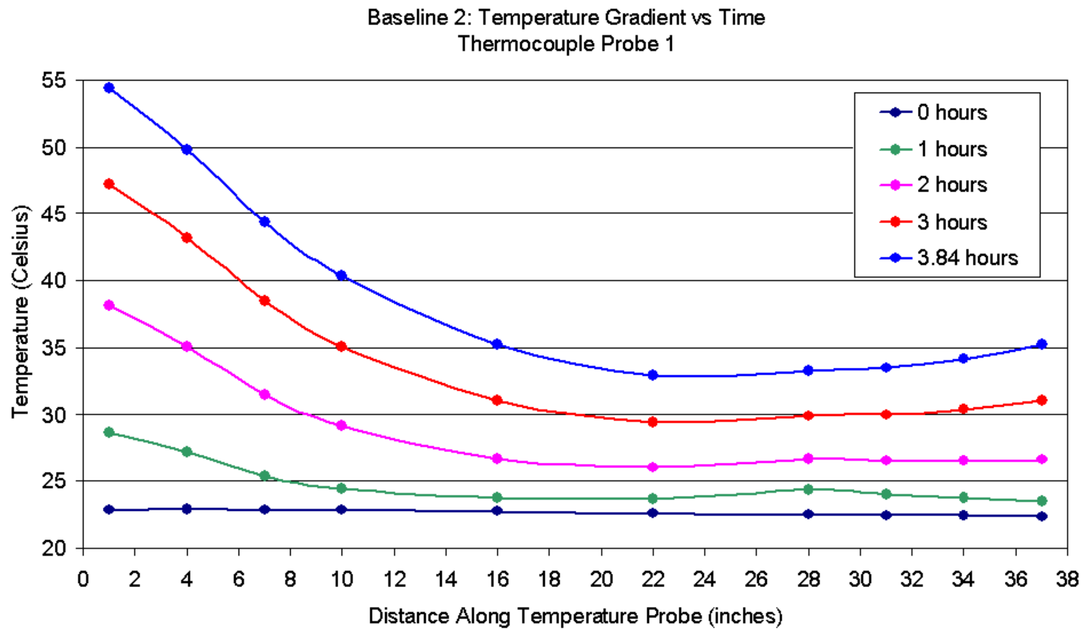


**Figure A.2:** Temperature Gradient vs Time, Probe 1, Baseline 2

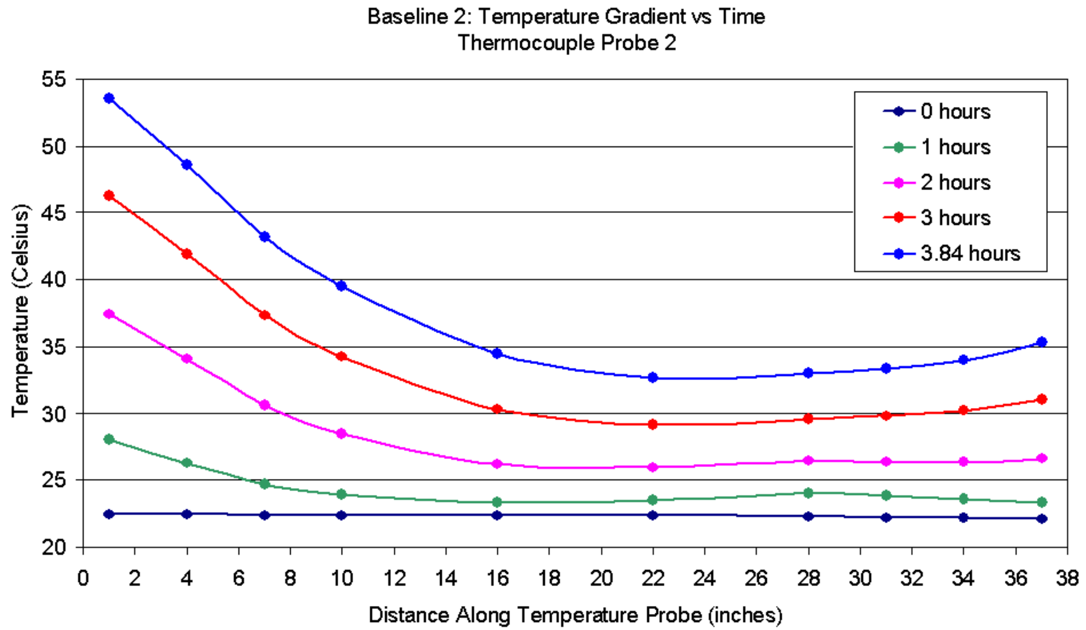


**Figure A.3:** Temperature Gradient vs Time, Probe 2, Baseline 2

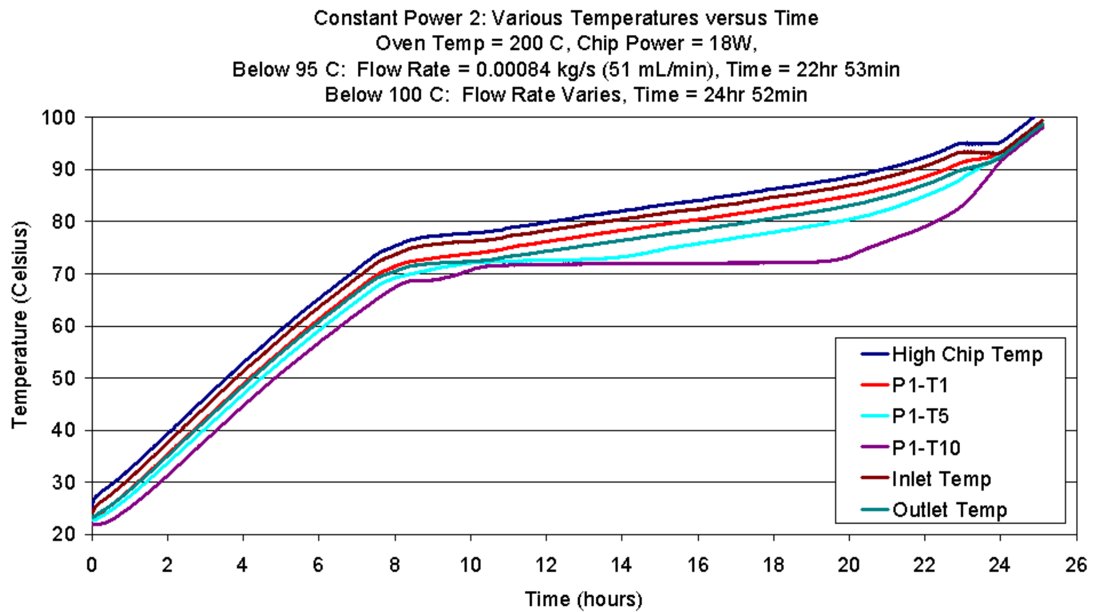


**Figure A.4:** Various Temperatures vs Time, Constant Power 2

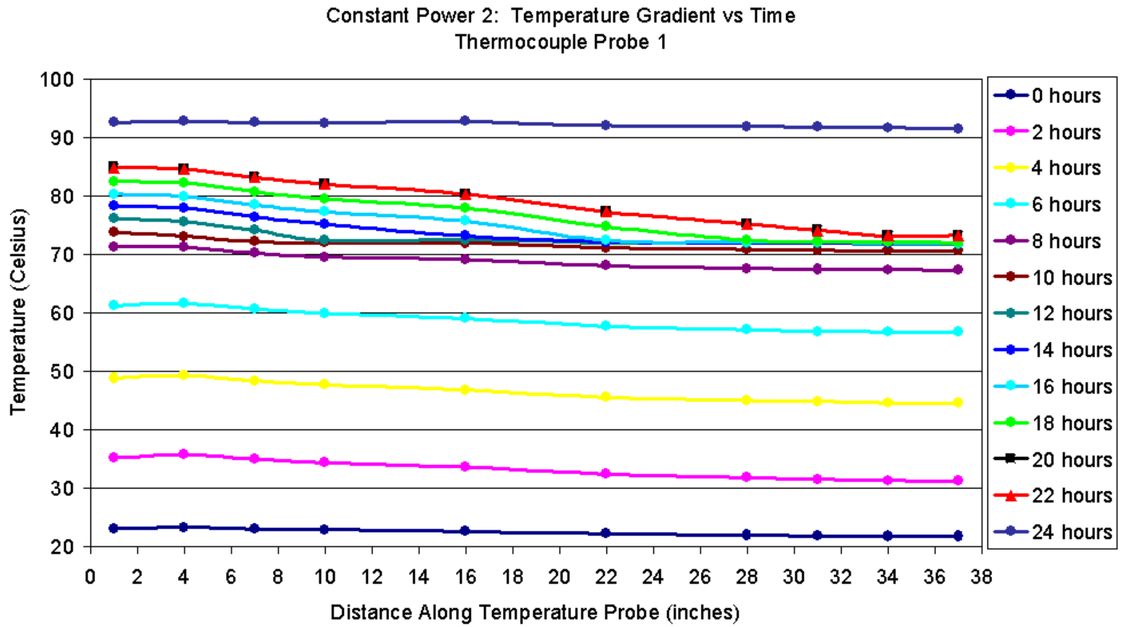


**Figure A.5:** Temperature Gradient vs Time, Probe 1, Constant Power 2

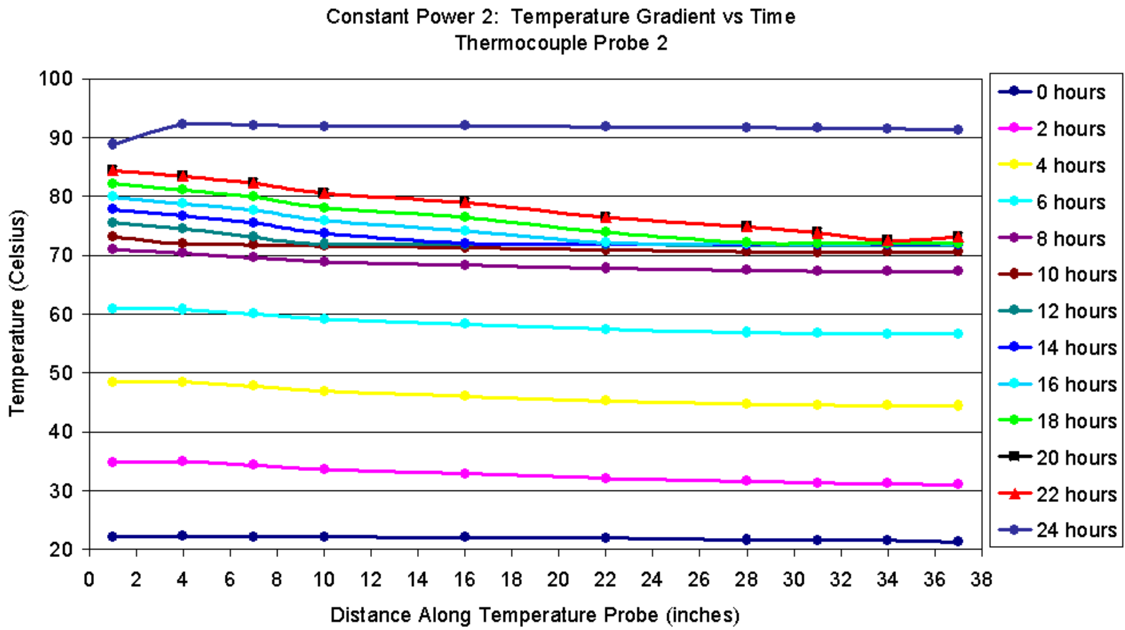


**Figure A.6:** Temperature Gradient vs Time, Probe 2, Constant Power 2

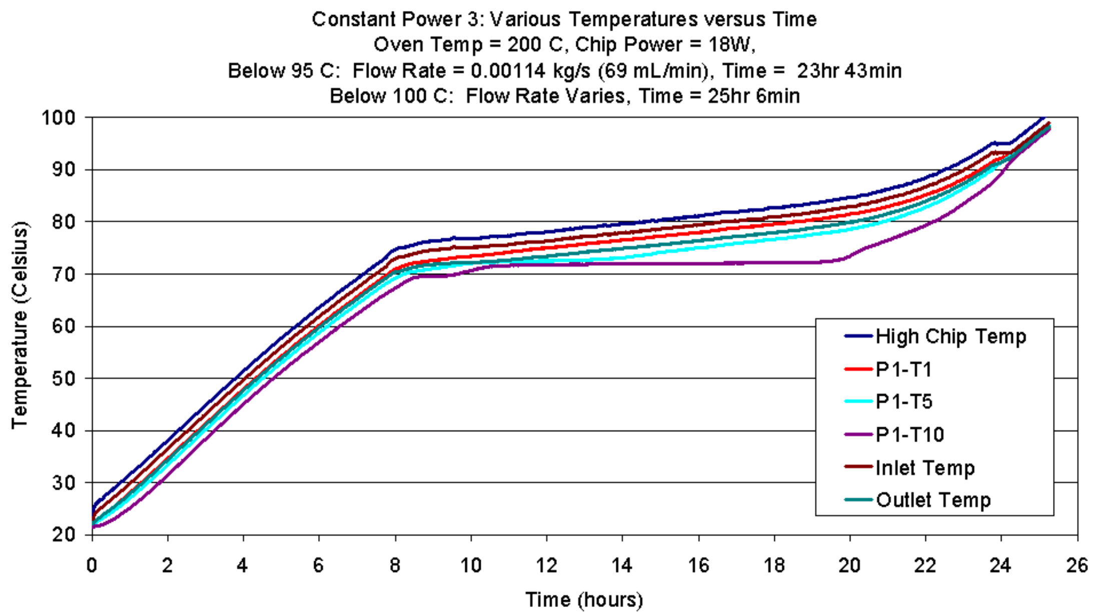


**Figure A.7:** Various Temperatures vs Time, Constant Power 3

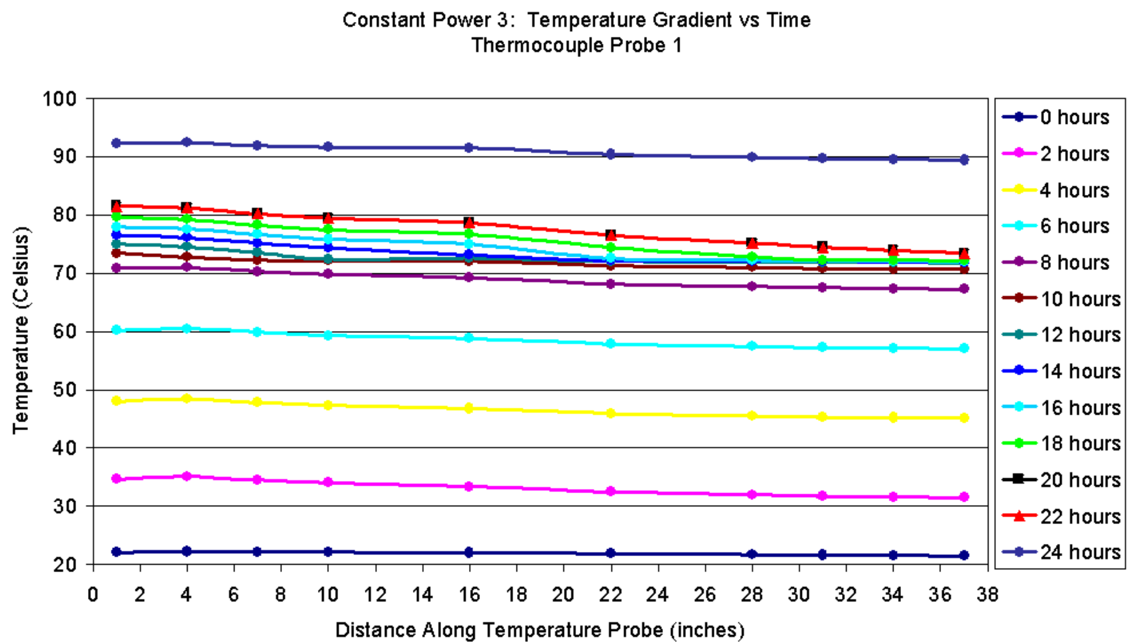


**Figure A.8:** Temperature Gradient vs Time, Probe 1, Constant Power 3

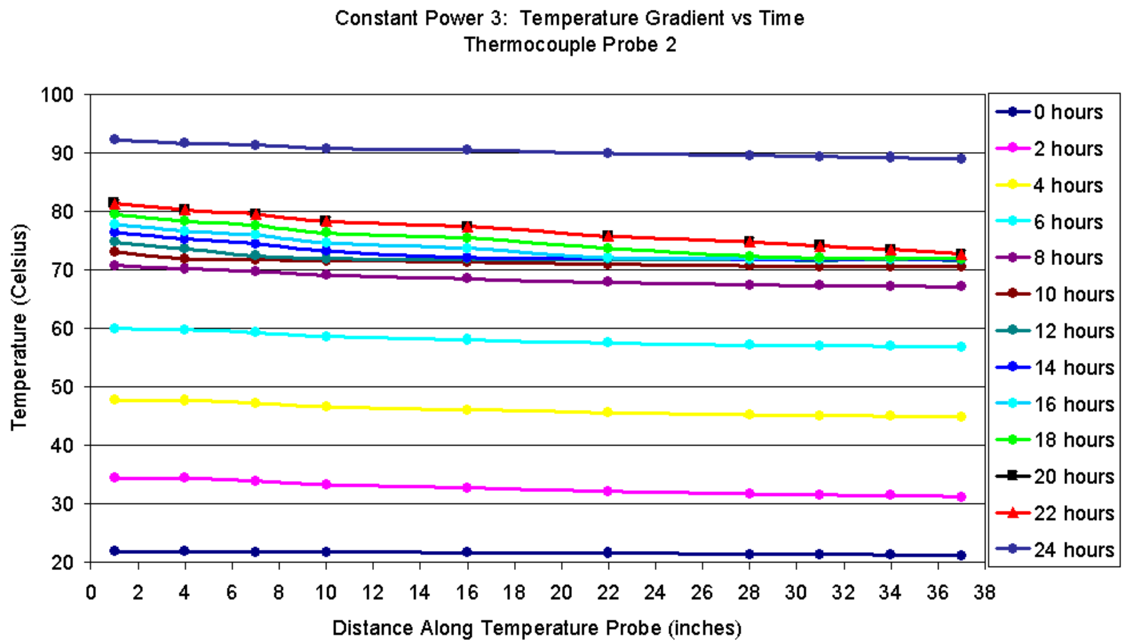


**Figure A.9:** Temperature Gradient vs Time, Probe 2, Constant Power 3

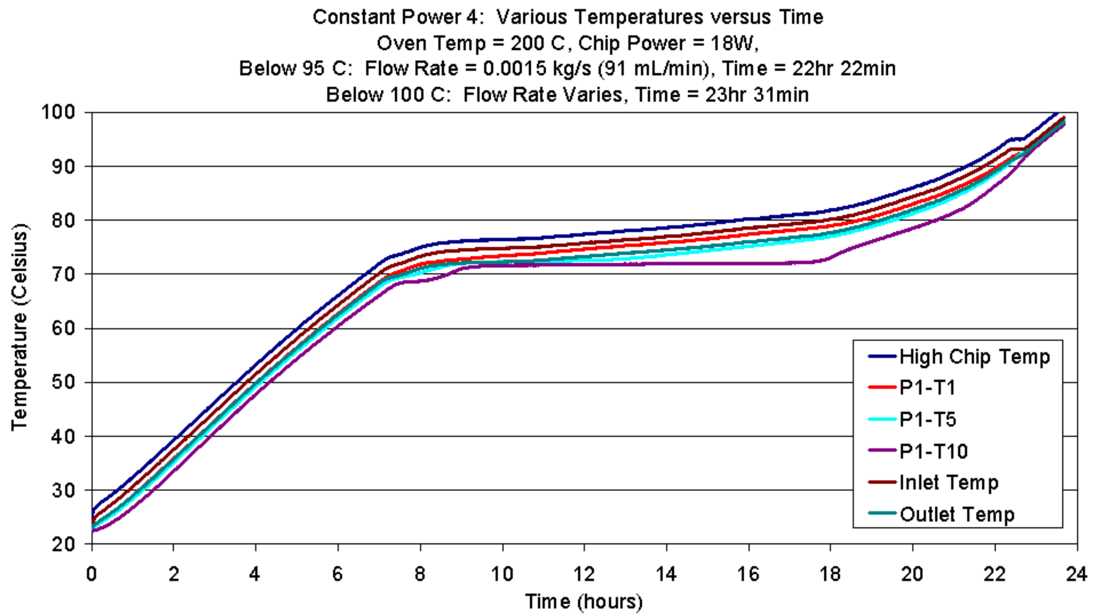


**Figure A.10:** Various Temperatures vs Time, Constant Power 4

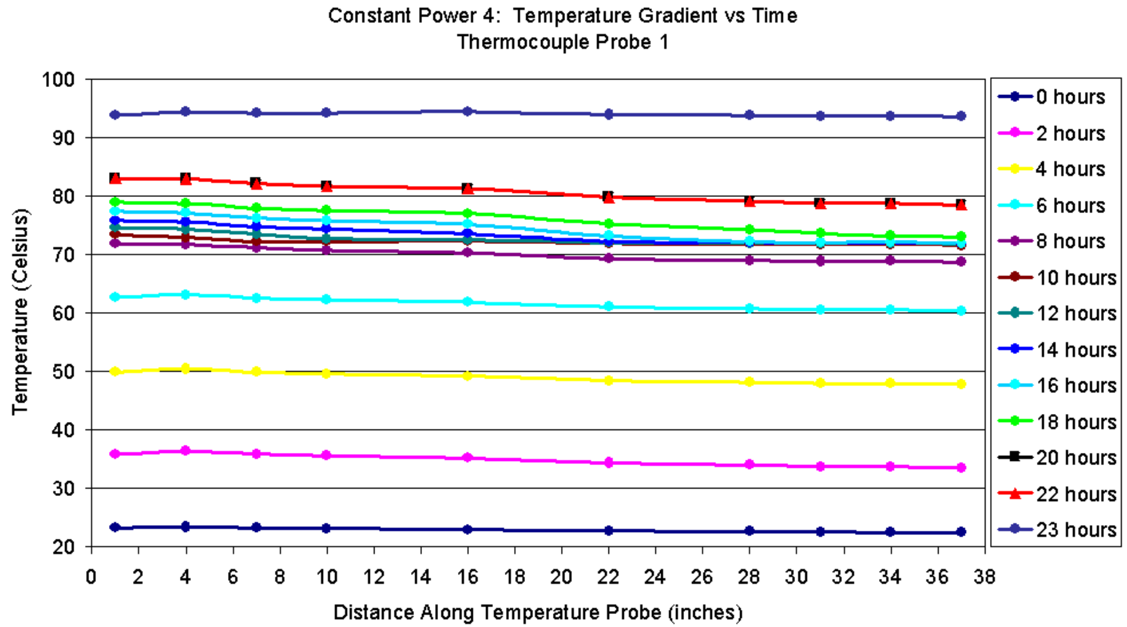


**Figure A.11:** Temperature Gradient vs Time, Probe 1, Constant Power 4

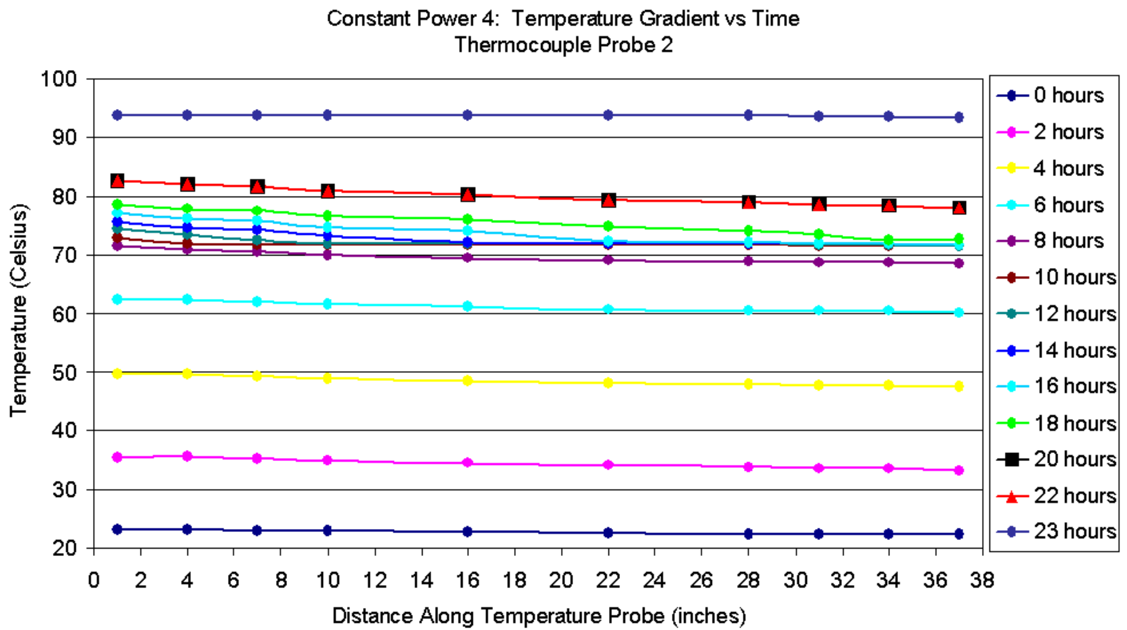


**Figure A.12:** Temperature Gradient vs Time, Probe 2, Constant Power 4

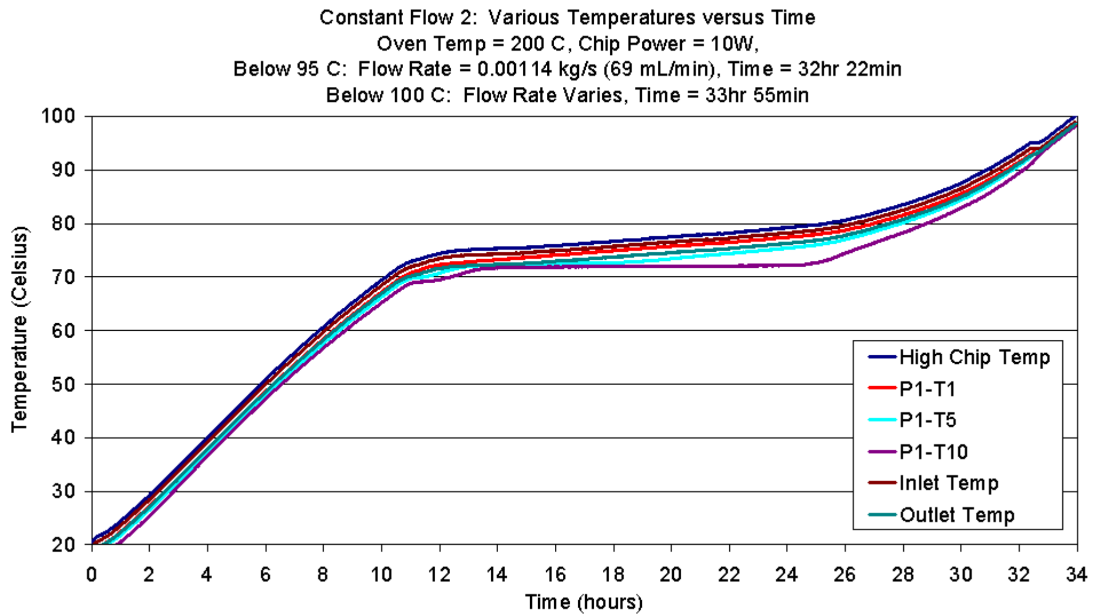


**Figure A.13:** Various Temperatures vs Time, Constant Flow 2

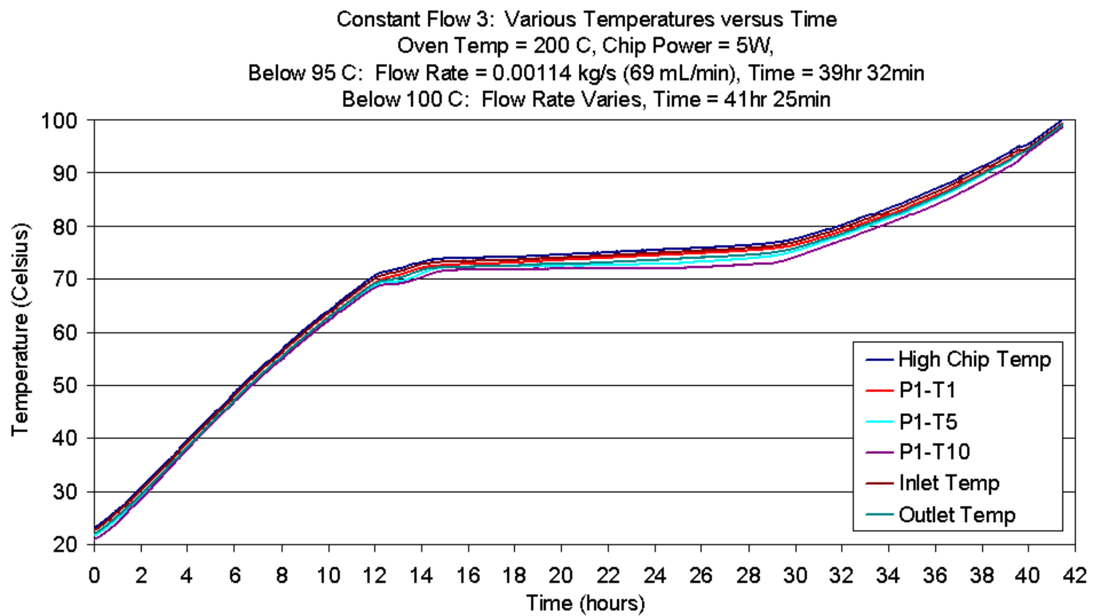


**Figure A.14:** Various Temperatures vs Time, Constant Flow 3

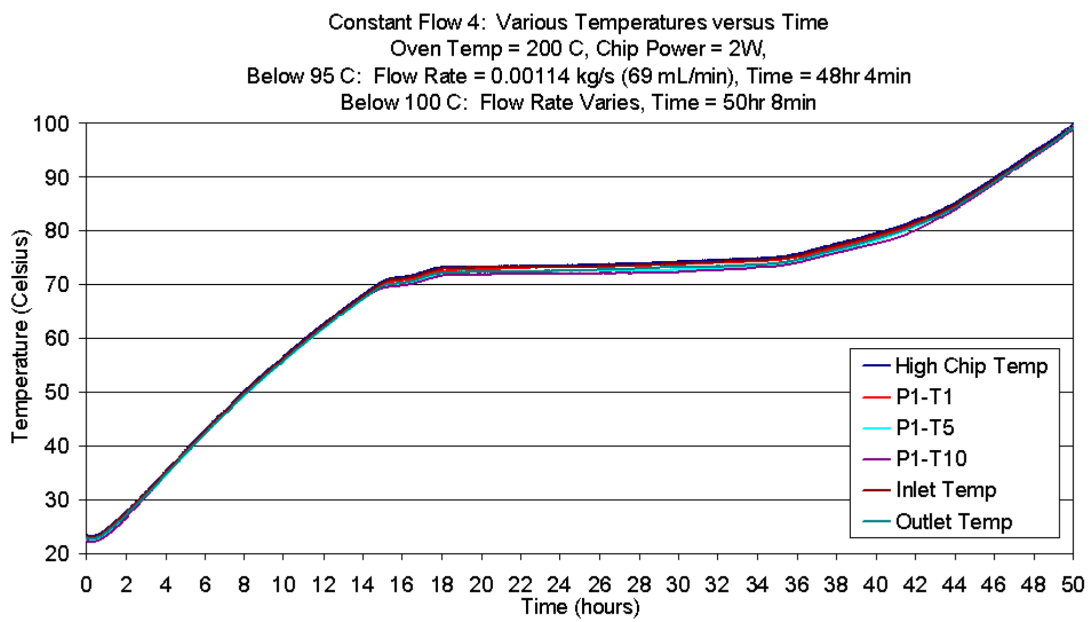


**Figure A.15:** Various Temperatures vs Time, Constant Flow 4

# APPENDIX B

# VACUUM FLASK THERMAL PERFORMANCE DATA

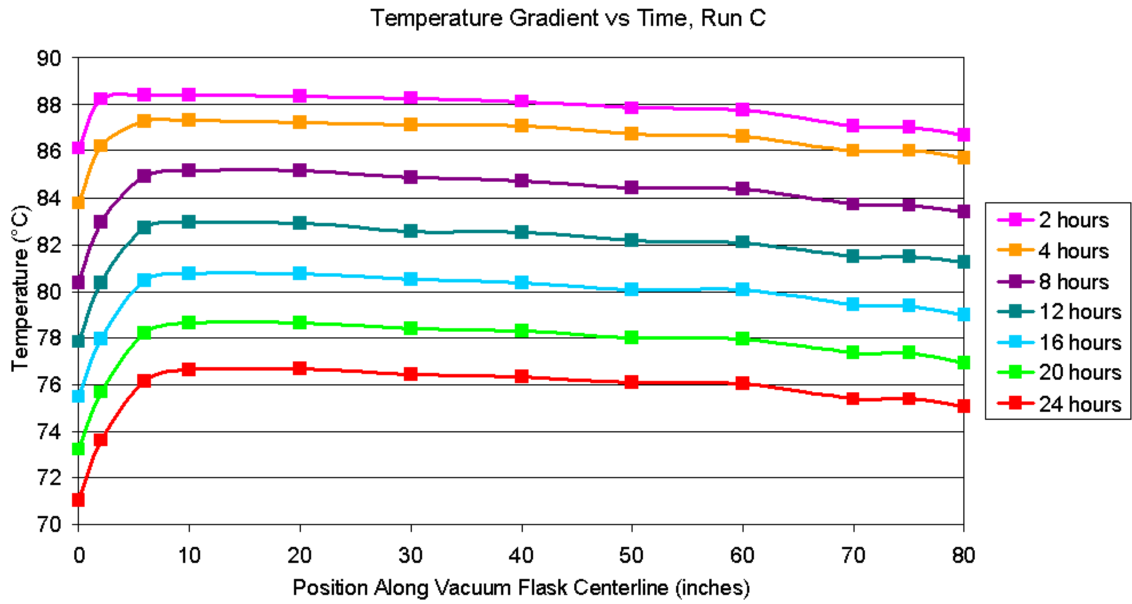


**Figure B.1:** Axial Temperature Gradient in Vacuum Flask vs Time, *Run C*

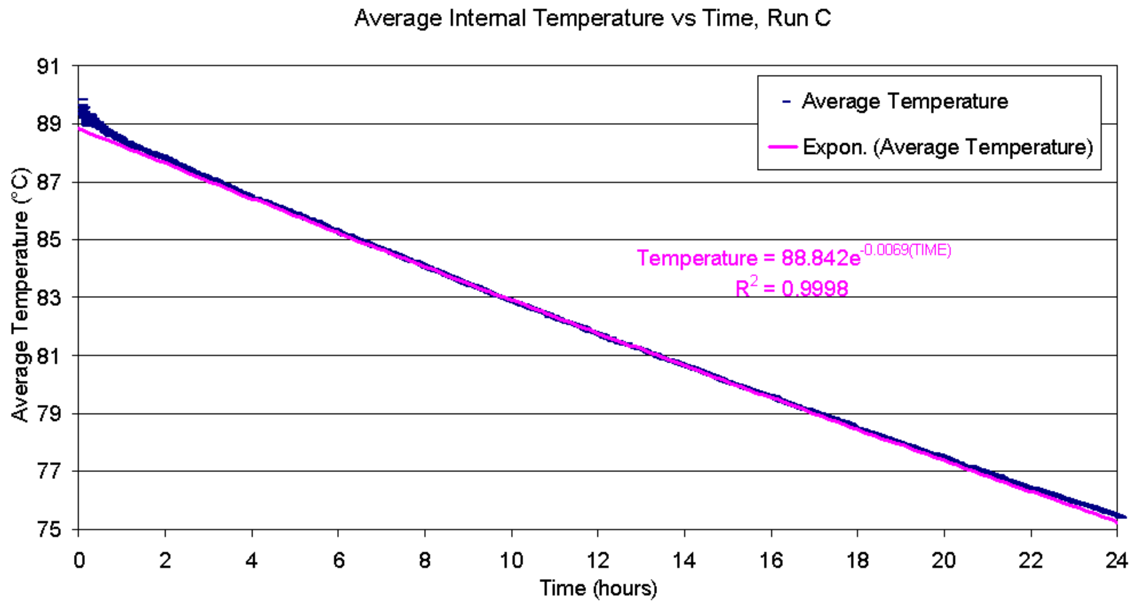


**Figure B.2:** Average Internal Vacuum Flask Temperature vs Time, *Run C*

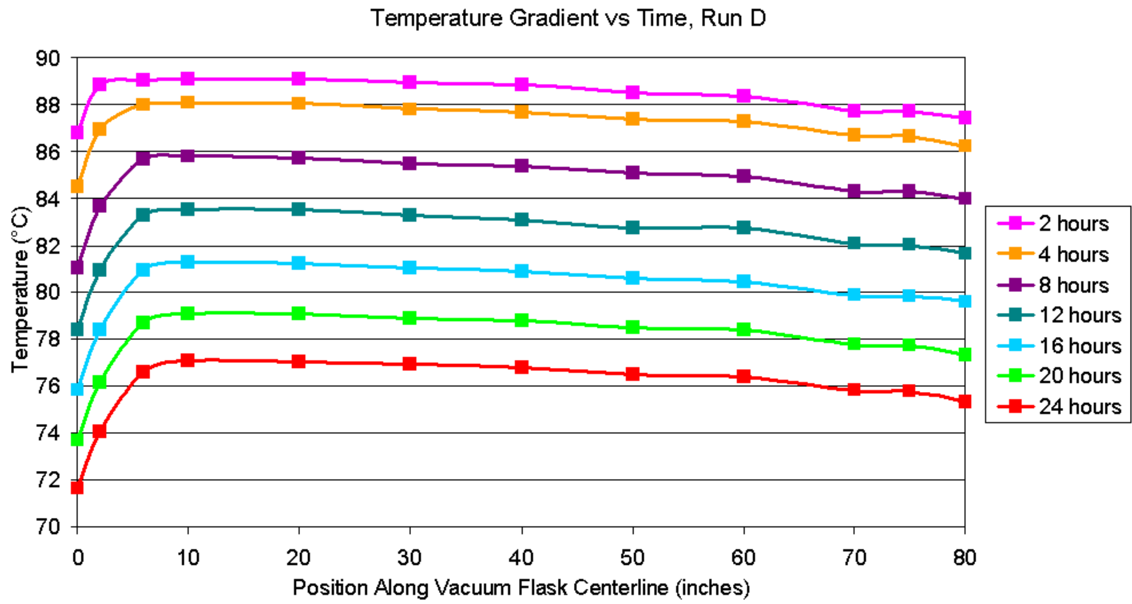


**Figure B.3:** Axial Temperature Gradient in Vacuum Flask vs Time, *Run D*

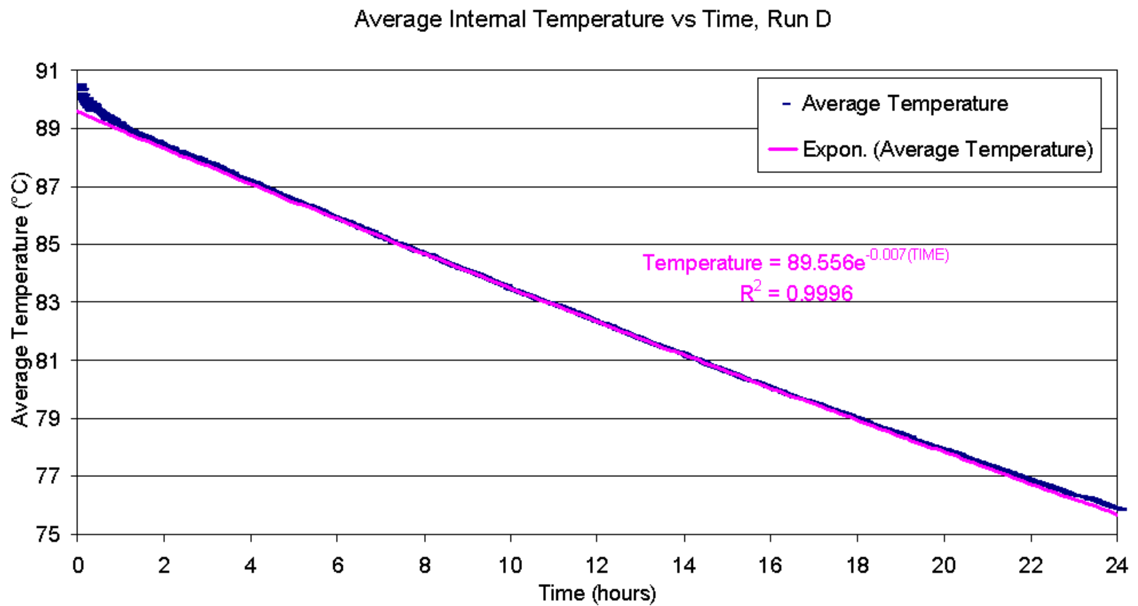


**Figure B.4:** Average Internal Vacuum Flask Temperature vs Time, *Run D*

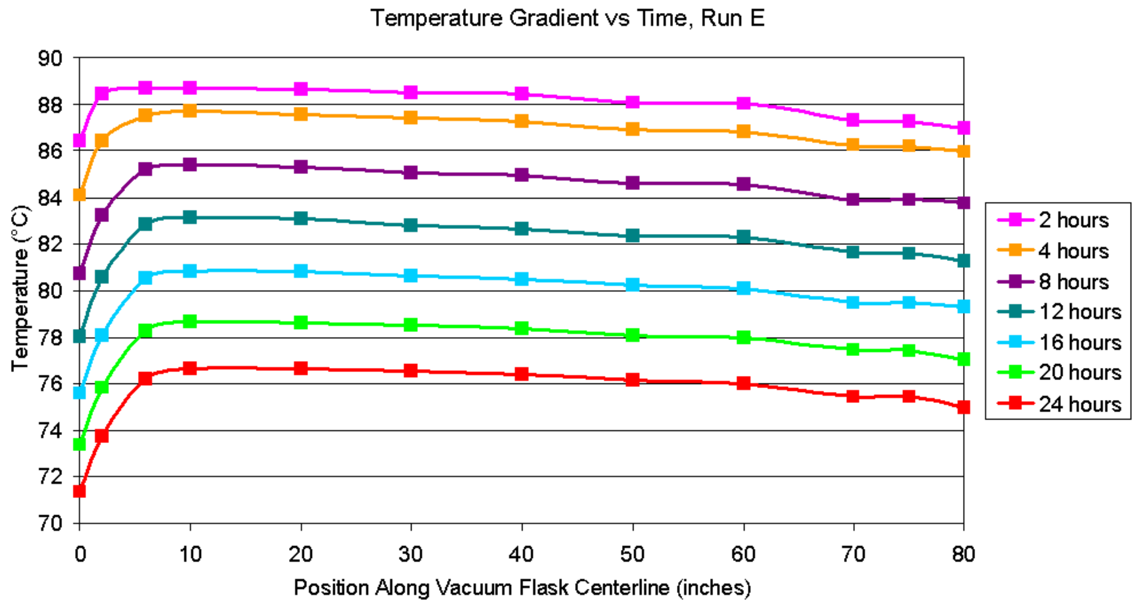


**Figure B.5:** Axial Temperature Gradient in Vacuum Flask vs Time, *Run E*

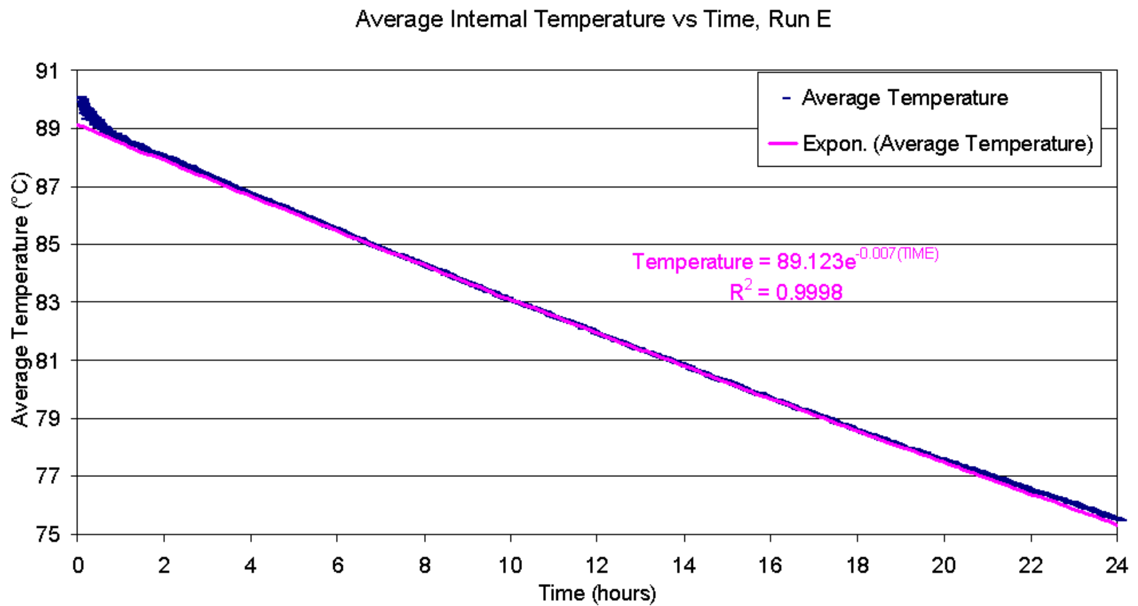


**Figure B.6:** Average Internal Vacuum Flask Temperature vs Time, *Run E*

# APPENDIX C

# LABVIEW$^{TM}$ BLOCK DIAGRAMS

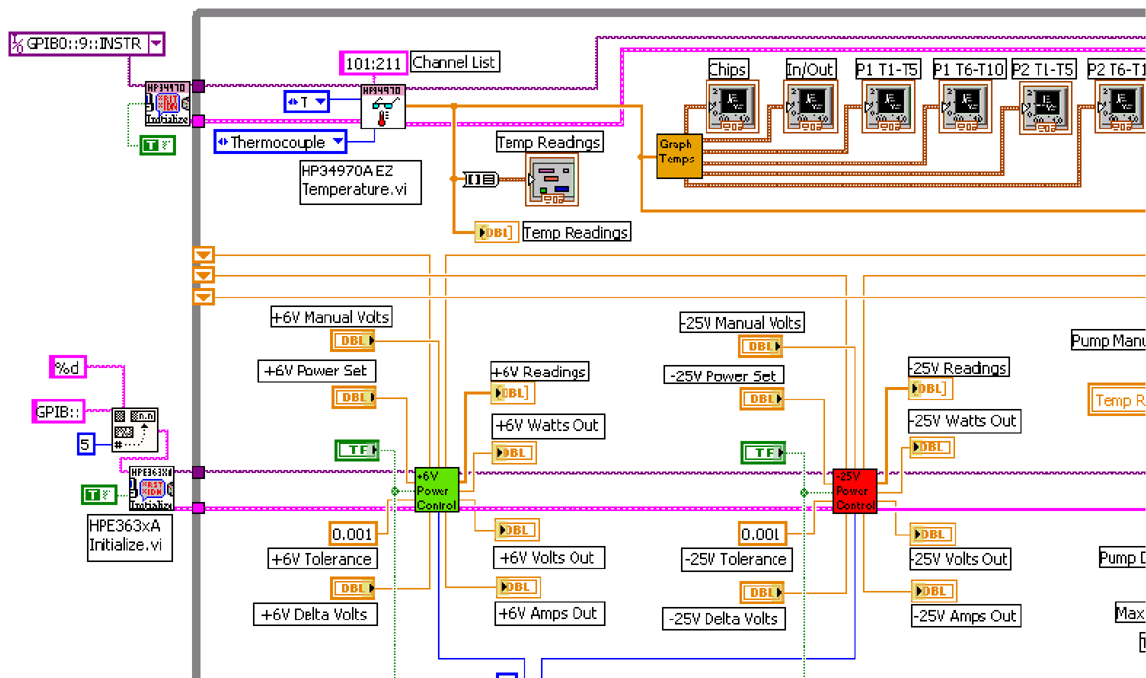


**Figure C.1:** *Main Temp Logger*, Northwest Corner

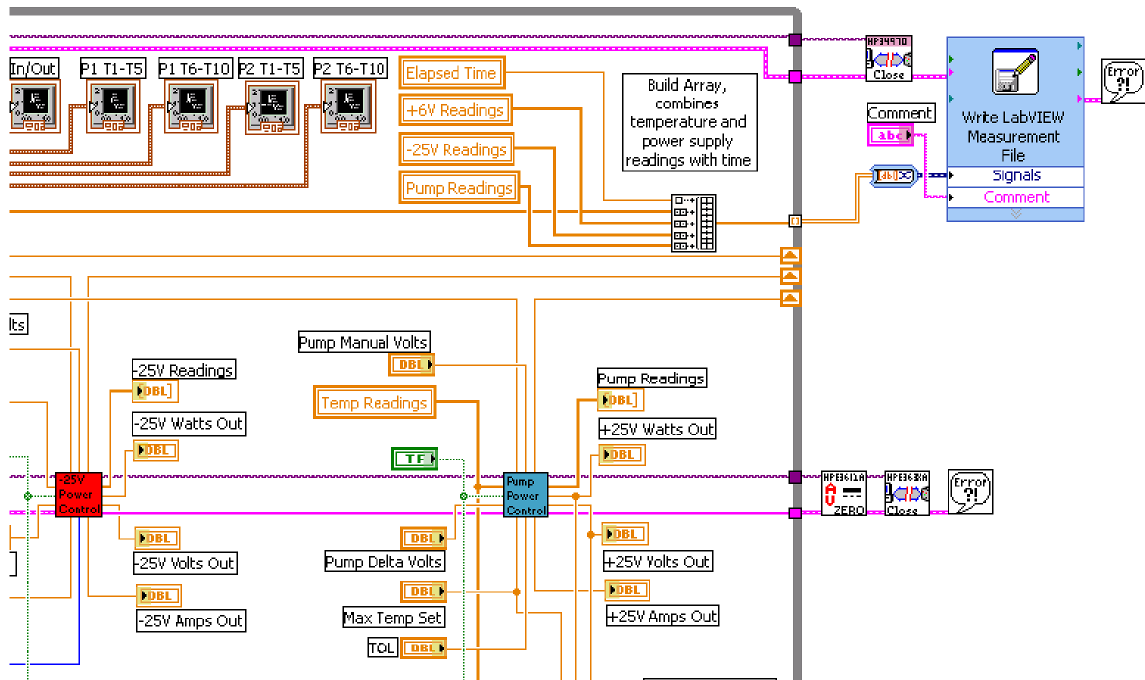


**Figure C.2:** Main Temp Logger, Northeast Corner

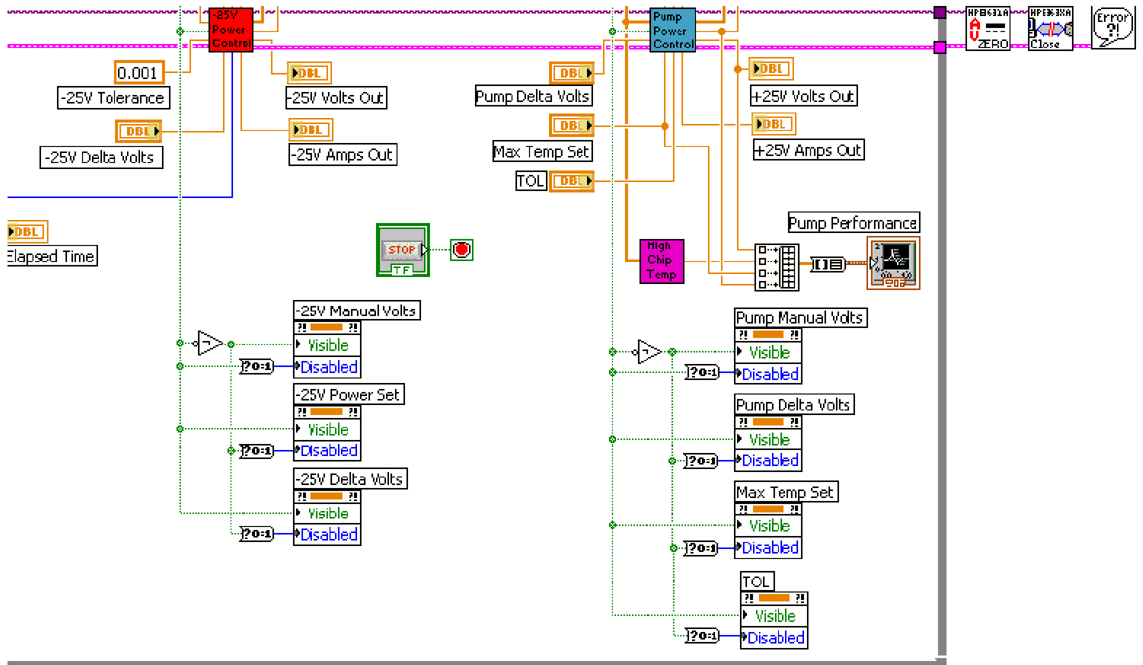


**Figure C.3:** *Main Temp Logger*, Southeast Corner

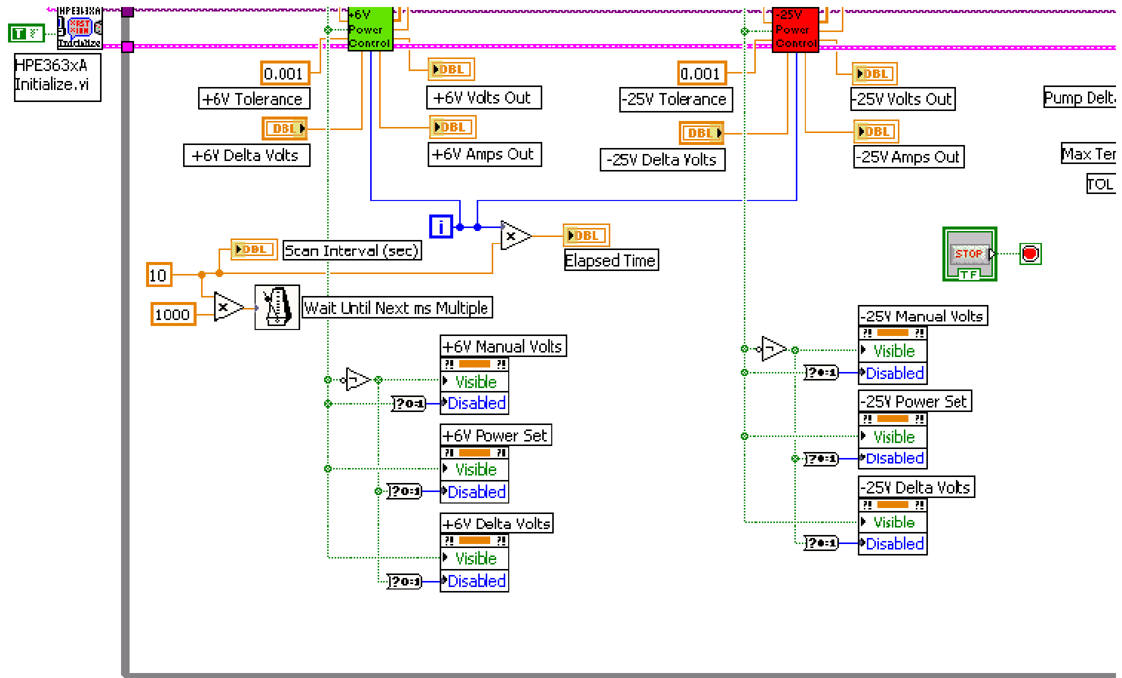


**Figure C.4:** *Main Temp Logger*, Southwest Corner

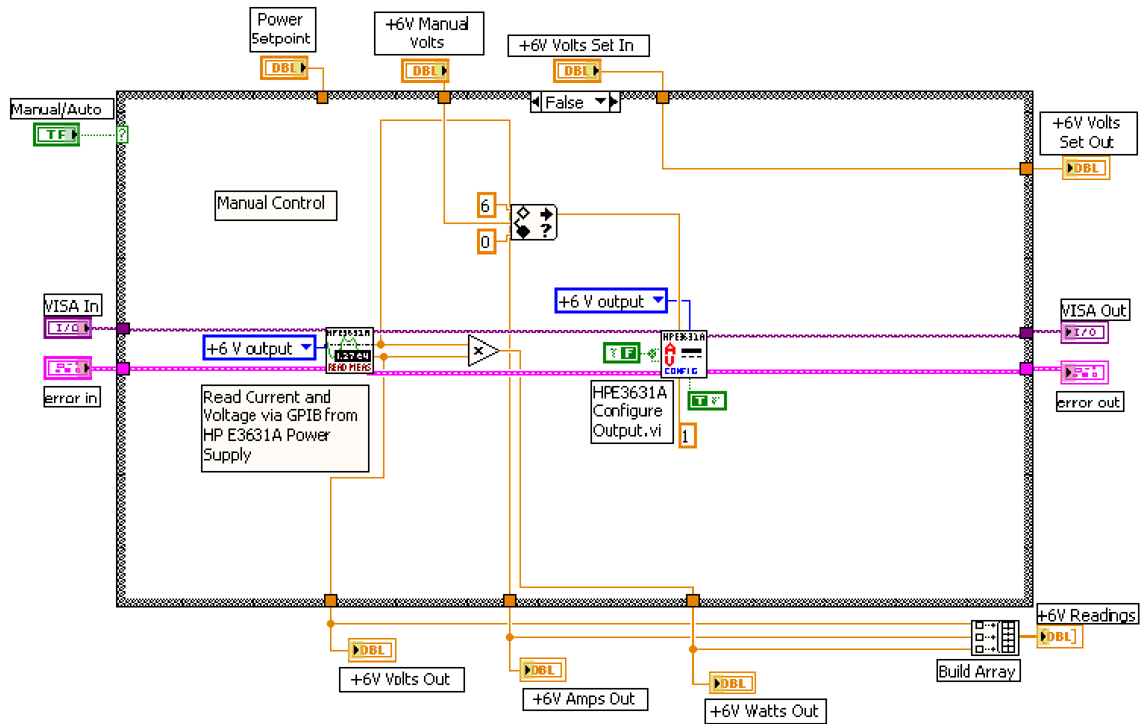


**Figure C.5:** *+6V Power Control*, Manual Mode

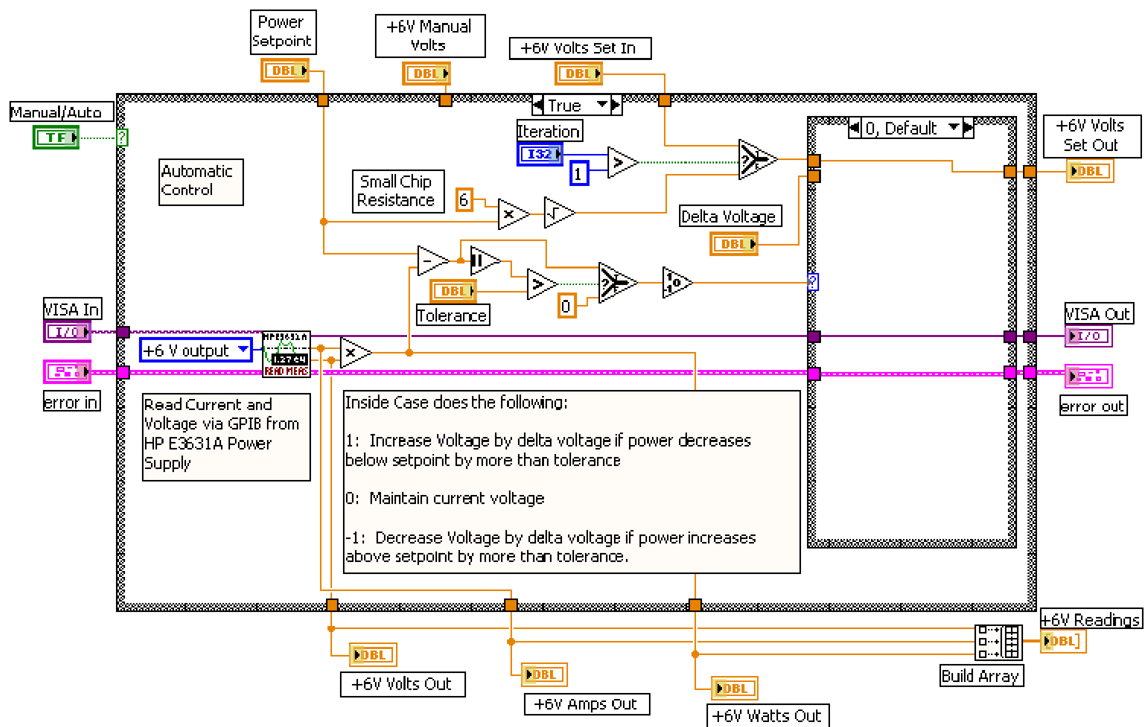


**Figure C.6:** *+6V Power Control*, Automatic Mode, Internal Case 0

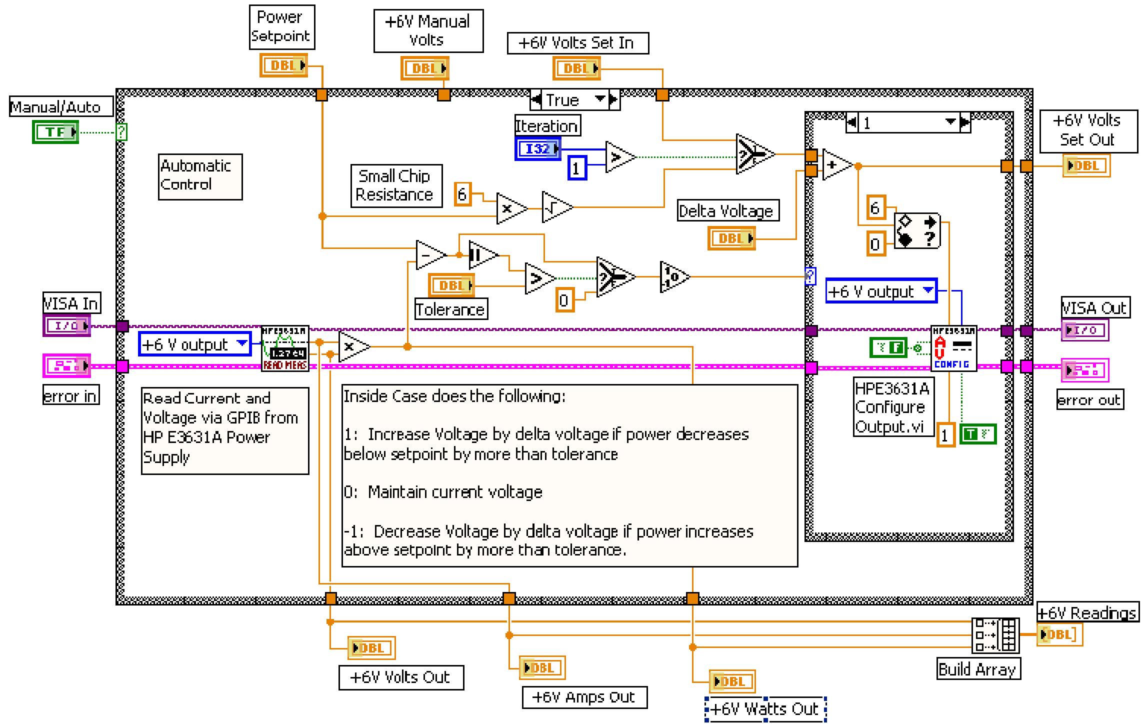


**Figure C.7:** *+6V Power Control*, Automatic Mode, Internal Case 1

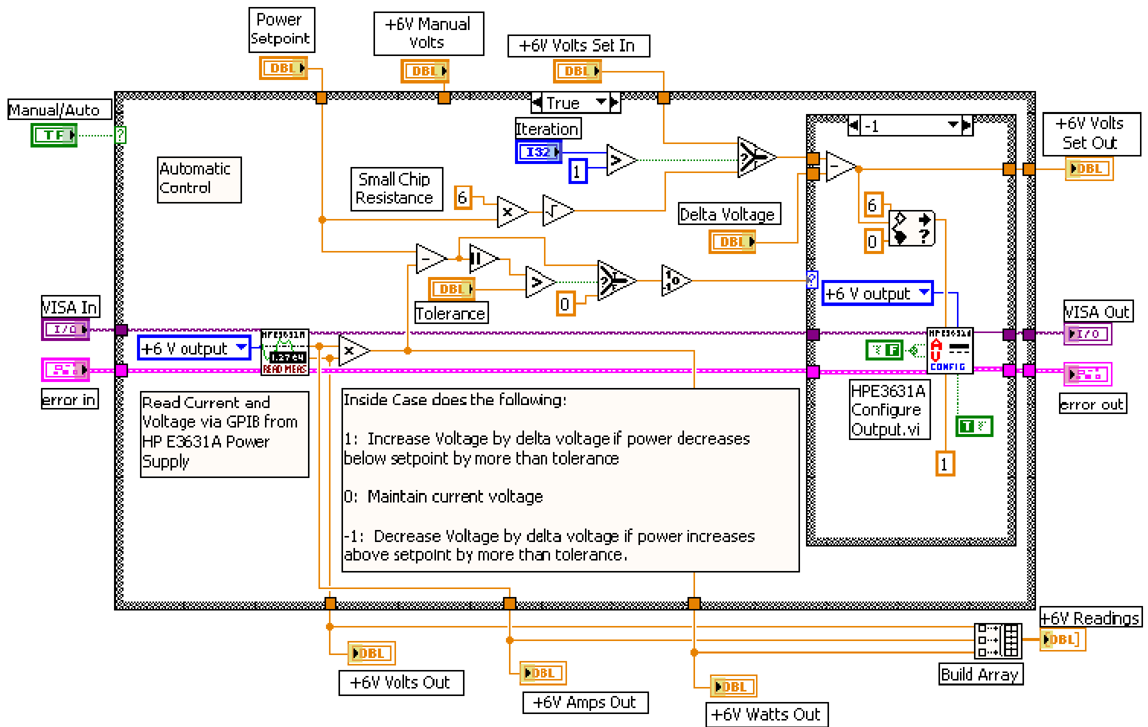


**Figure C.8:** *+6V Power Control*, Automatic Mode, Internal Case -1

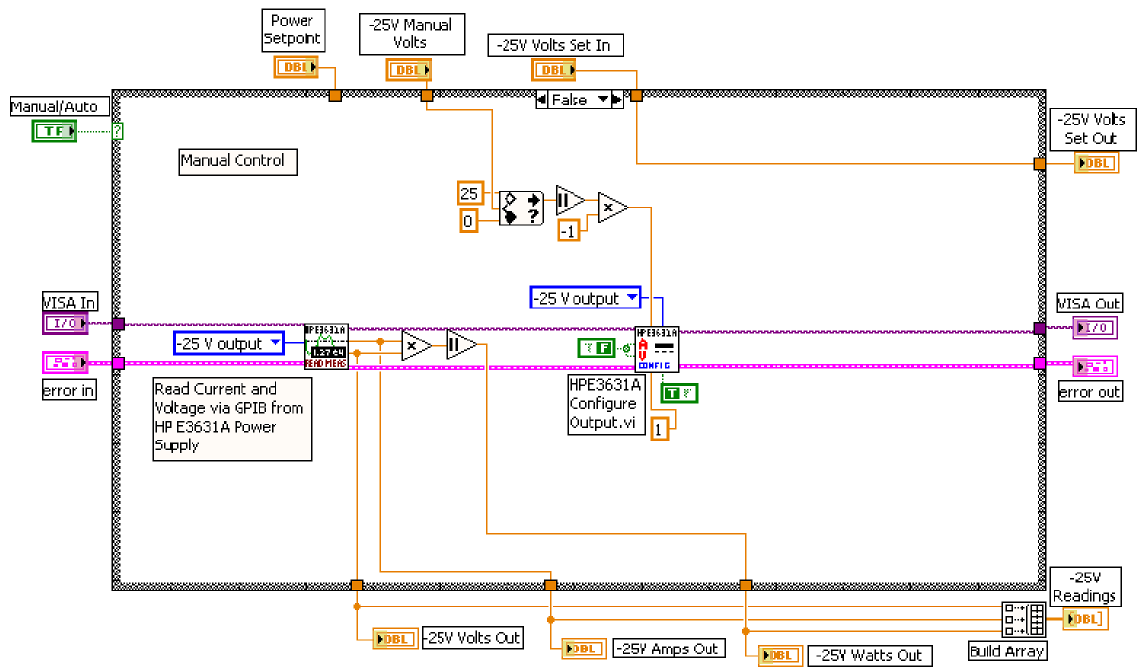


**Figure C.9:** *-25V Power Control*, Manual Mode

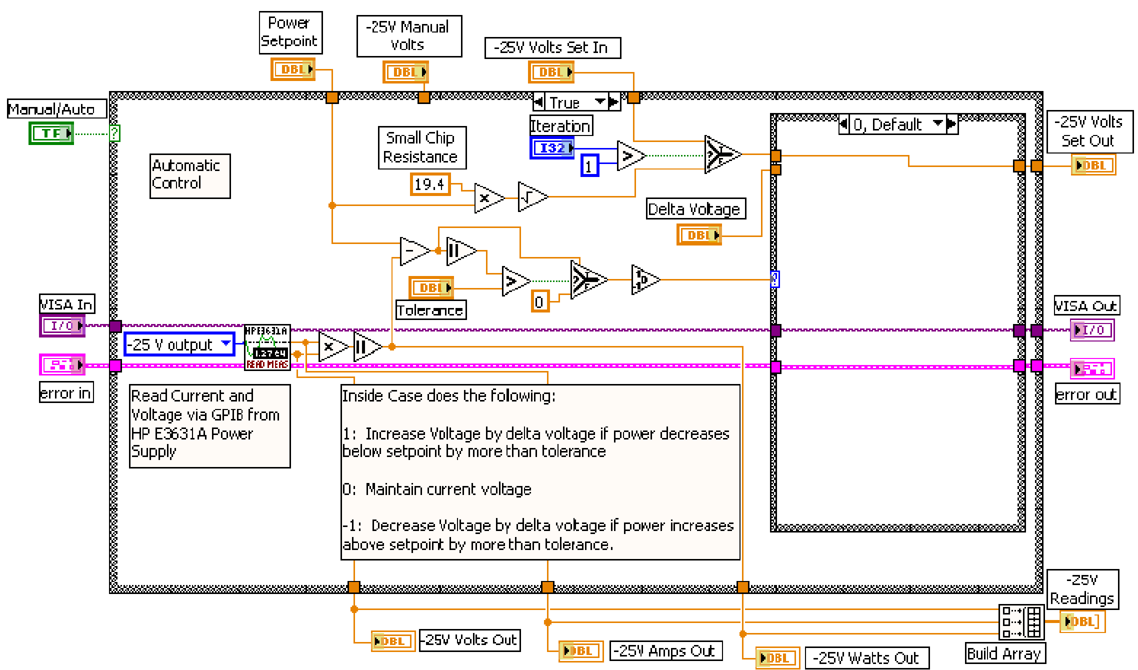


**Figure C.10:** *-25V Power Control*, Automatic Mode, Internal Case 0

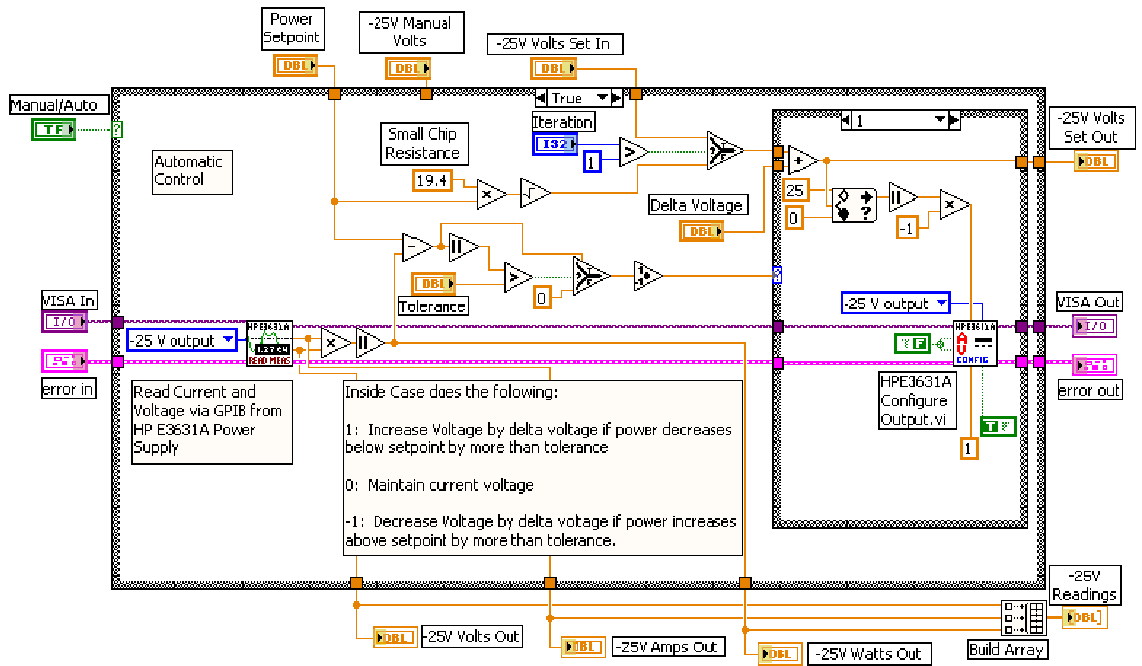


**Figure C.11:** *-25V Power Control*, Automatic Mode, Internal Case 1

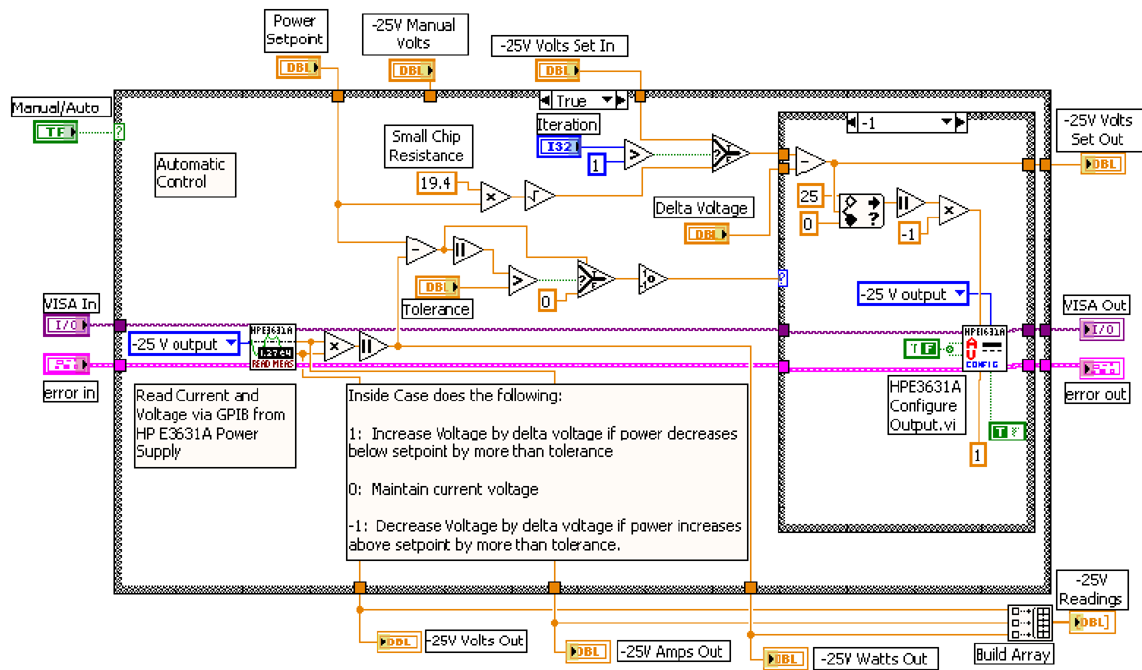


**Figure C.12:** *-25V Power Control*, Automatic Mode, Internal Case -1

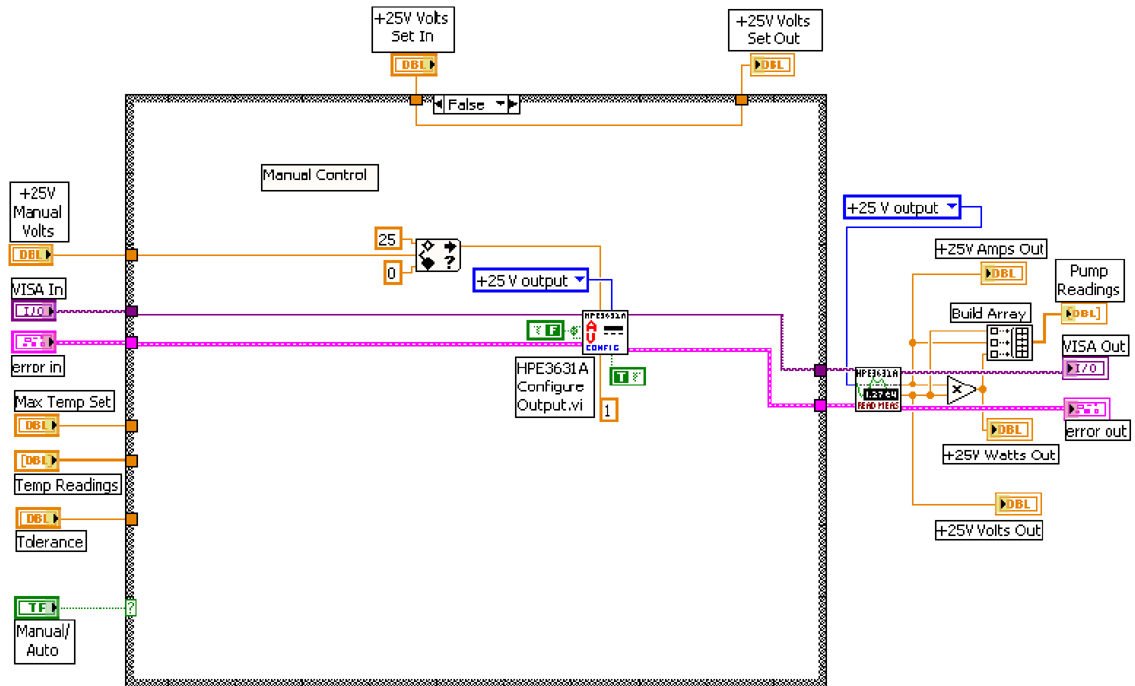


**Figure C.13:** *Pump Power Control*, Manual Mode

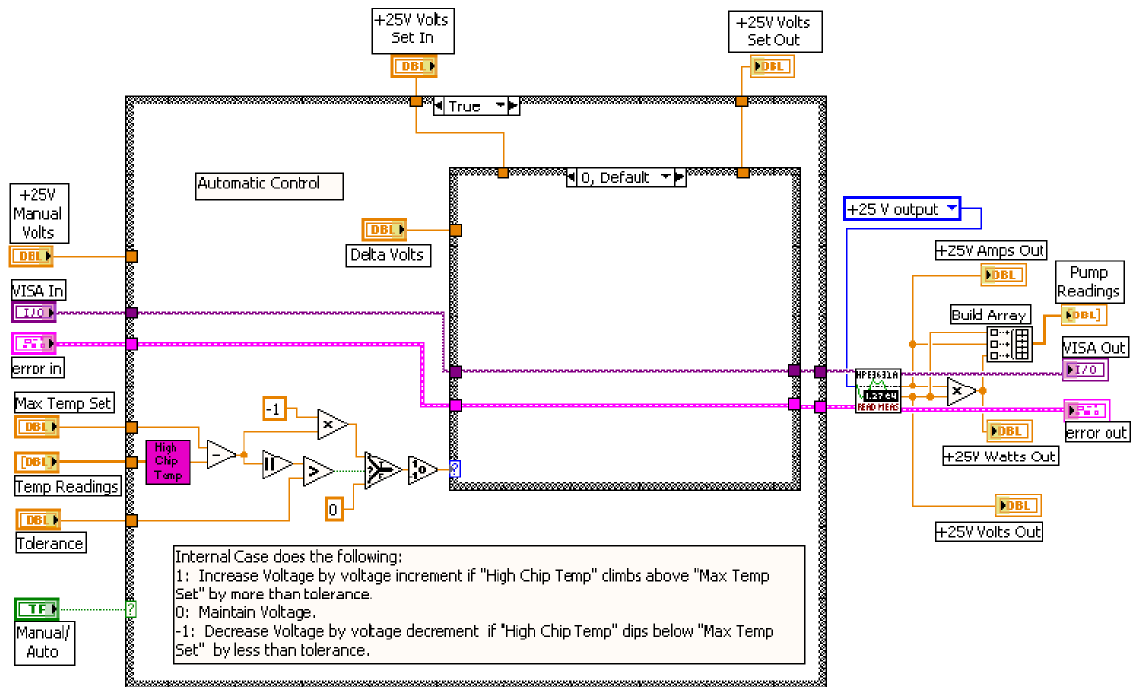


**Figure C.14:** *Pump Power Control*, Automatic Mode, Internal Case 0

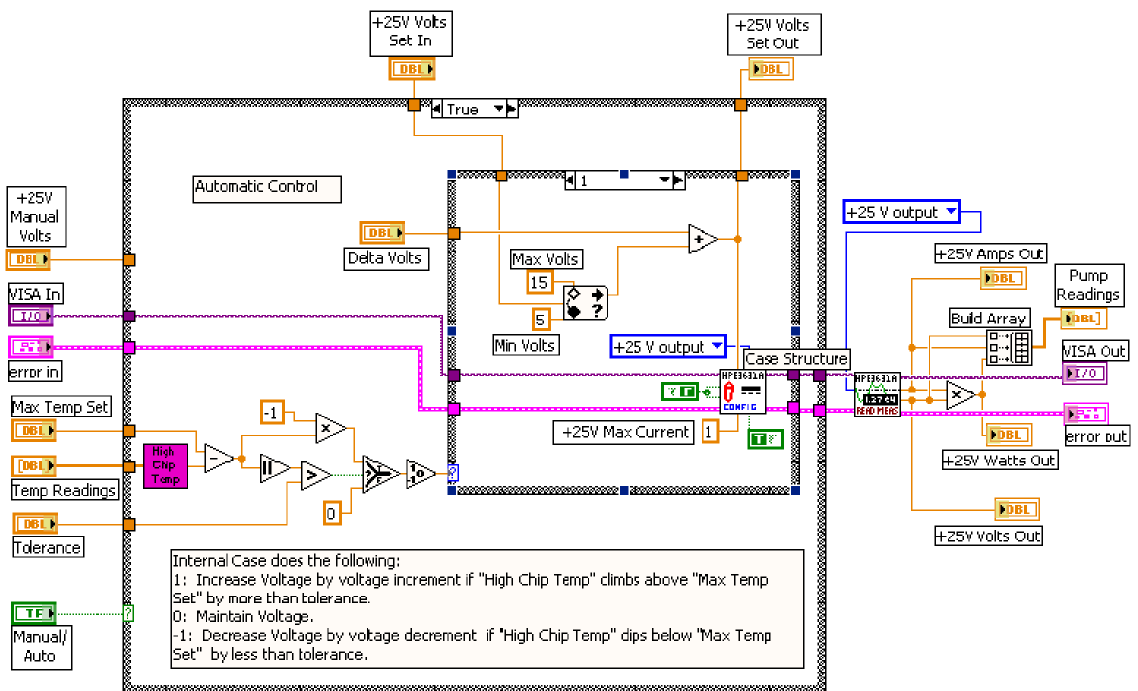


**Figure C.15:** *Pump Power Control*, Automatic Mode, Internal Case 1

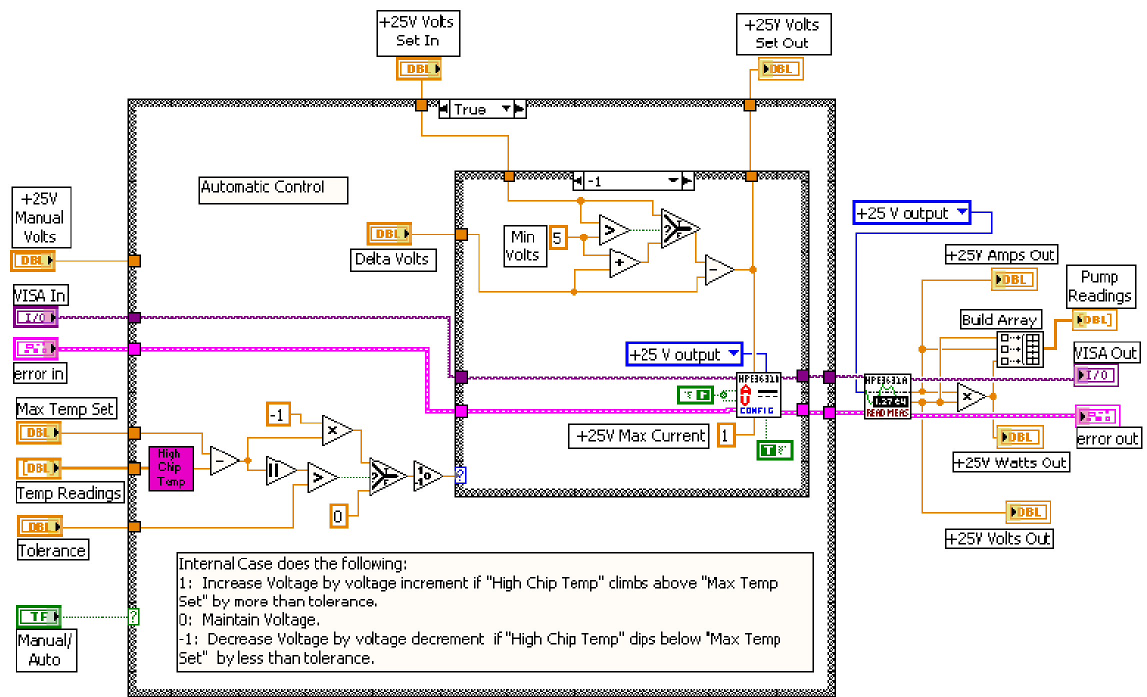


**Figure C.16:** *Pump Power Control*, Automatic Mode, Internal Case -1

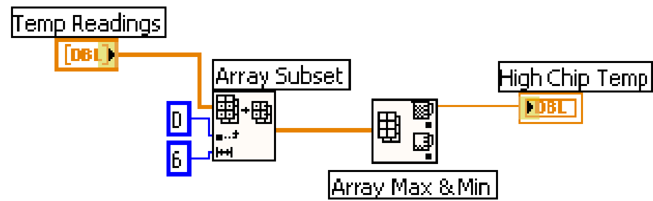


**Figure C.17:** *High Chip Temp* SubVI

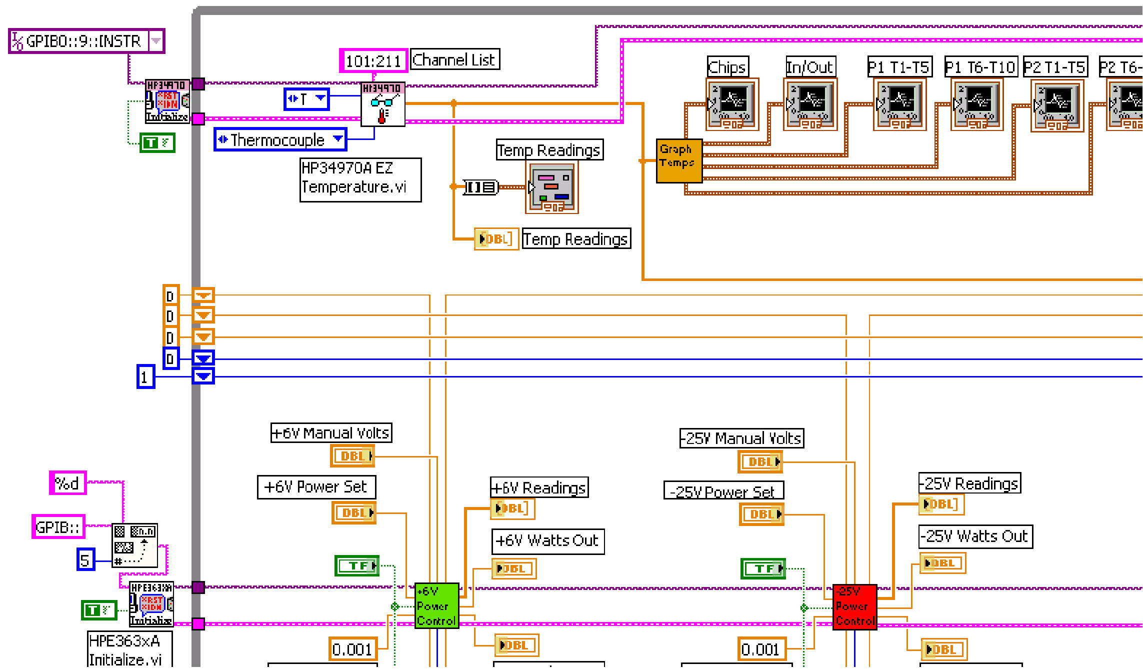


**Figure C.18:** *Flow Rate vs Voltage Logger*, Northwest Corner

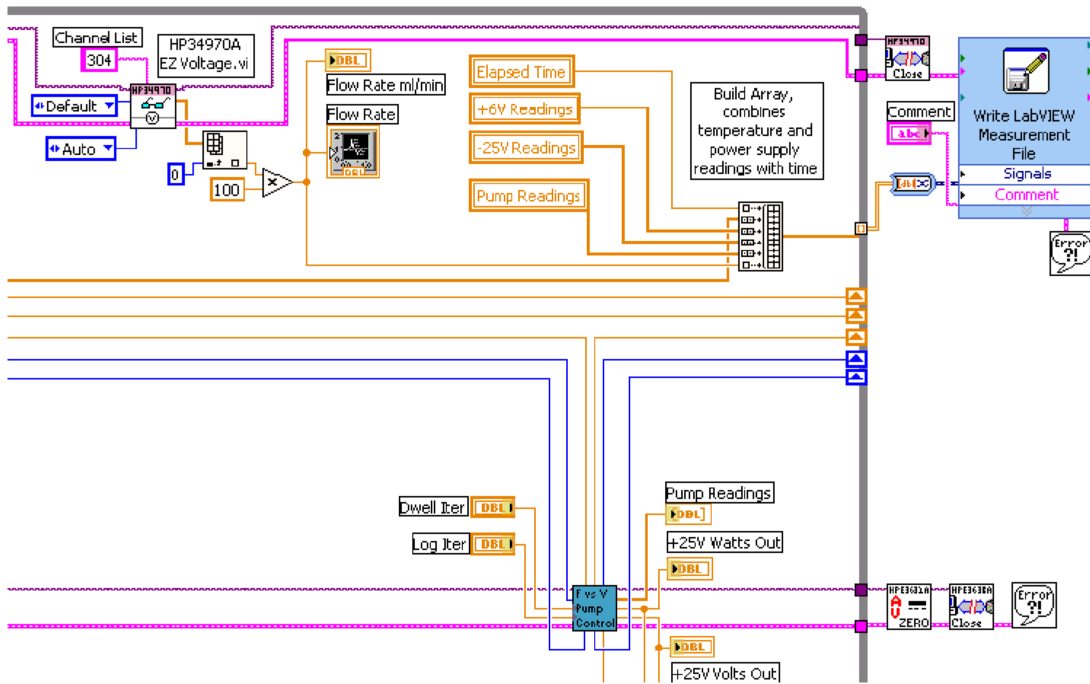


**Figure C.19:** *Flow Rate vs Voltage Logger*, Northeast Corner

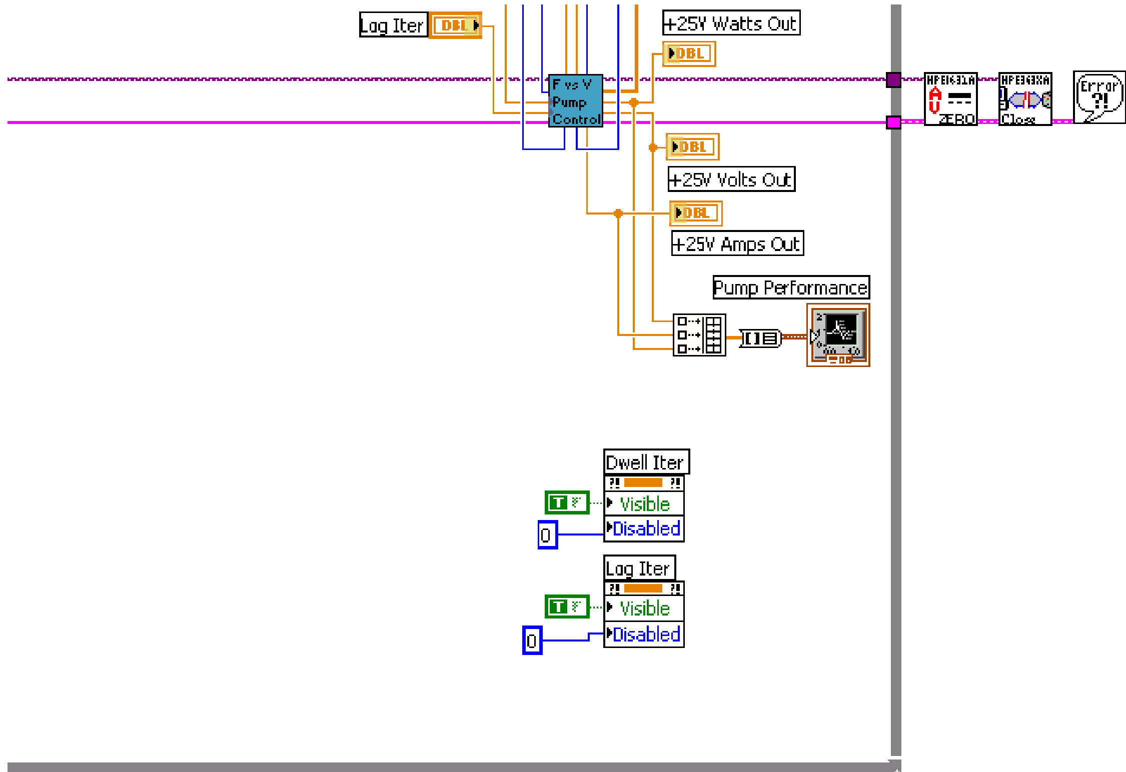


**Figure C.20:** *Flow Rate vs Voltage Logger*, Southeast Corner

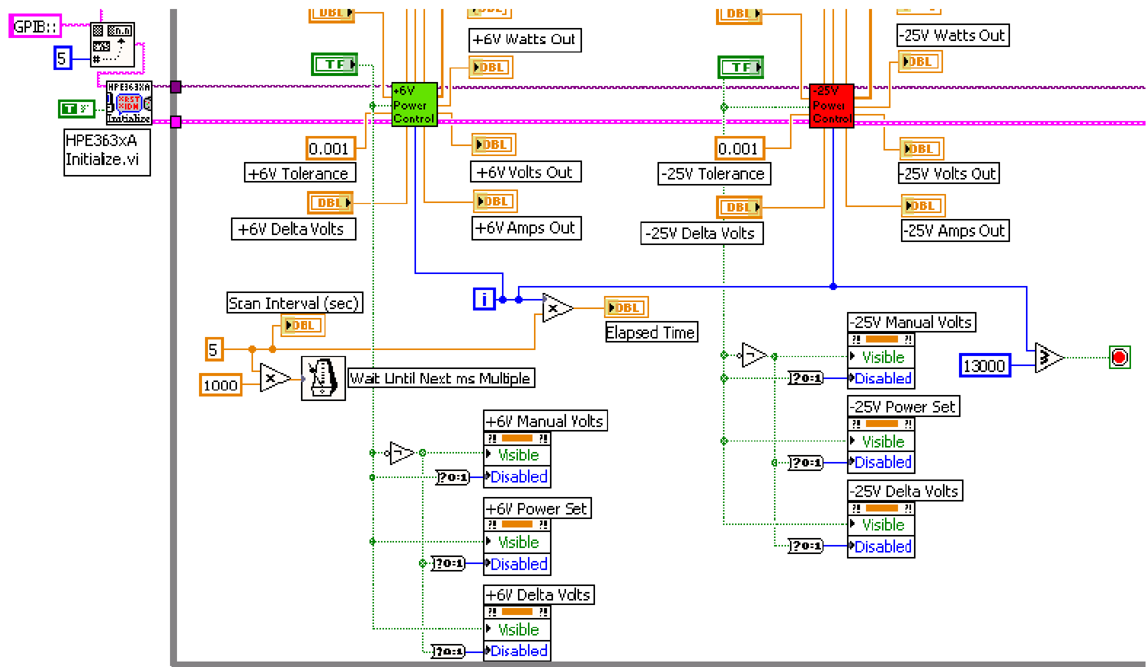


**Figure C.21:** *Flow Rate vs Voltage Logger*, Southwest Corner

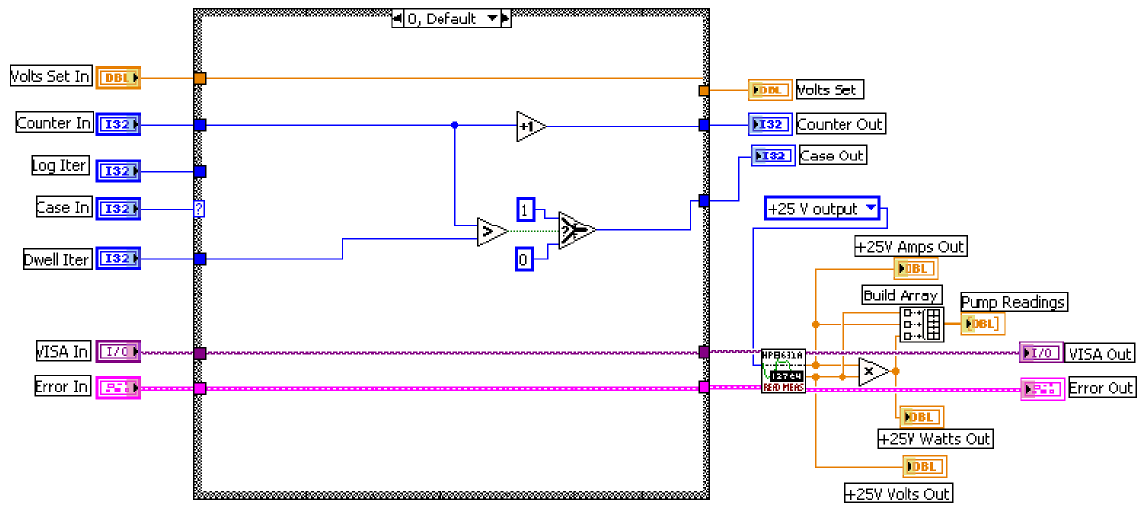


**Figure C.22:** *F vs V Pump Control*, External Case 0

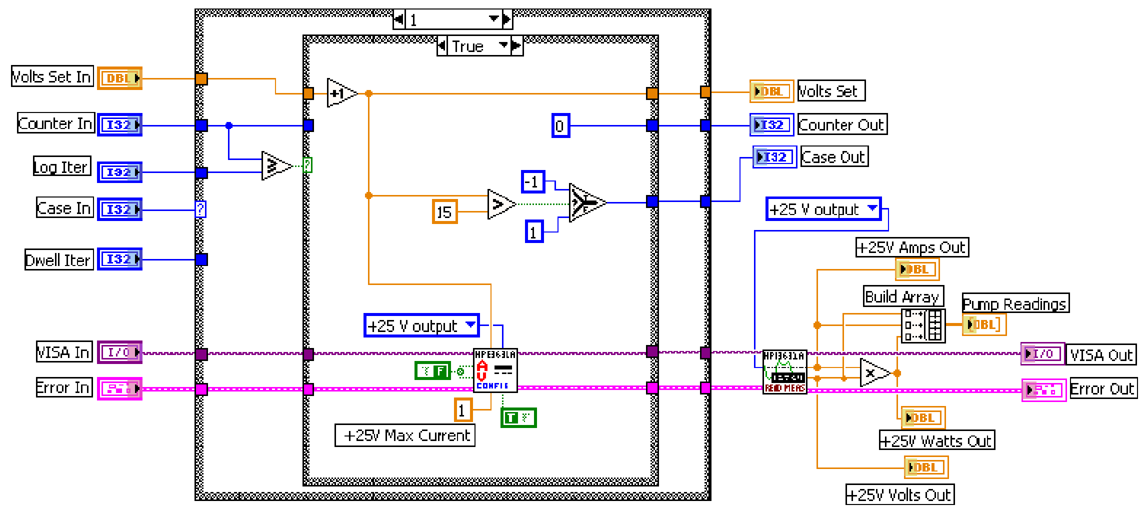


**Figure C.23:** *F vs V Pump Control*, External Case 1, Internal Case True

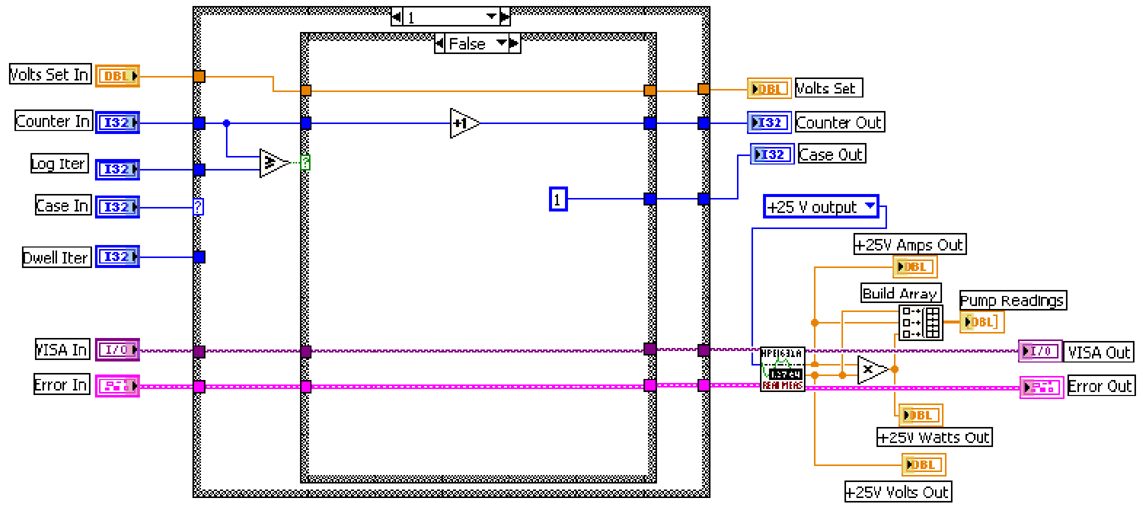


**Figure C.24:** *F vs V Pump Control*, External Case 1, Internal Case False

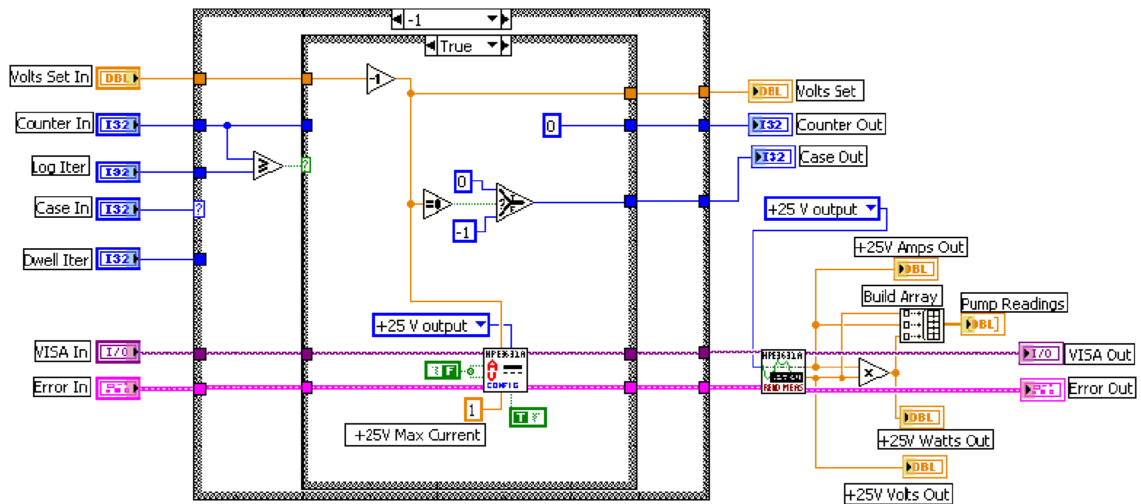


**Figure C.25:** *F vs V Pump Control*, External Case -1, Internal Case True

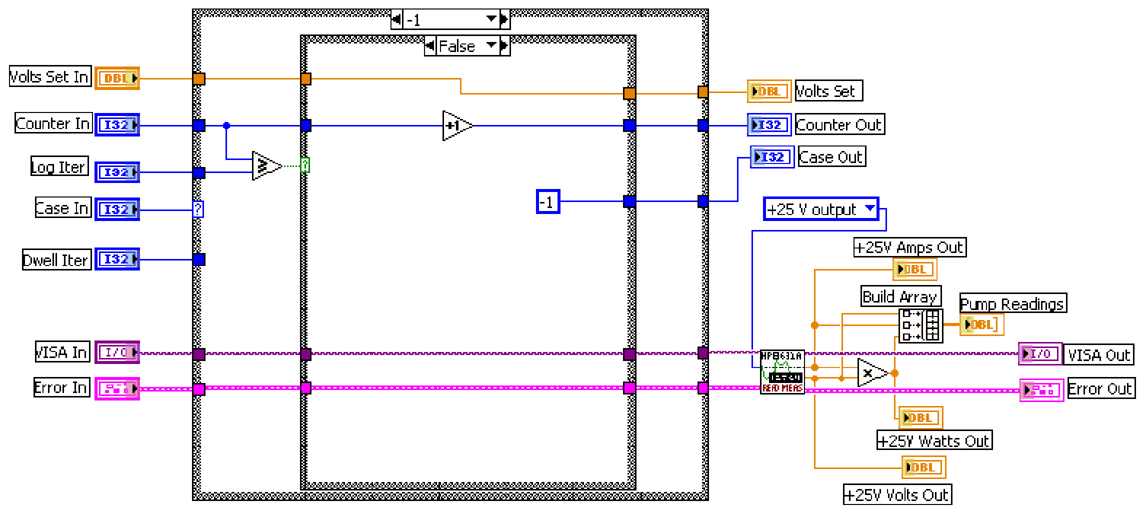


**Figure C.26:** *F vs V Pump Control*, External Case -1, Internal Case False

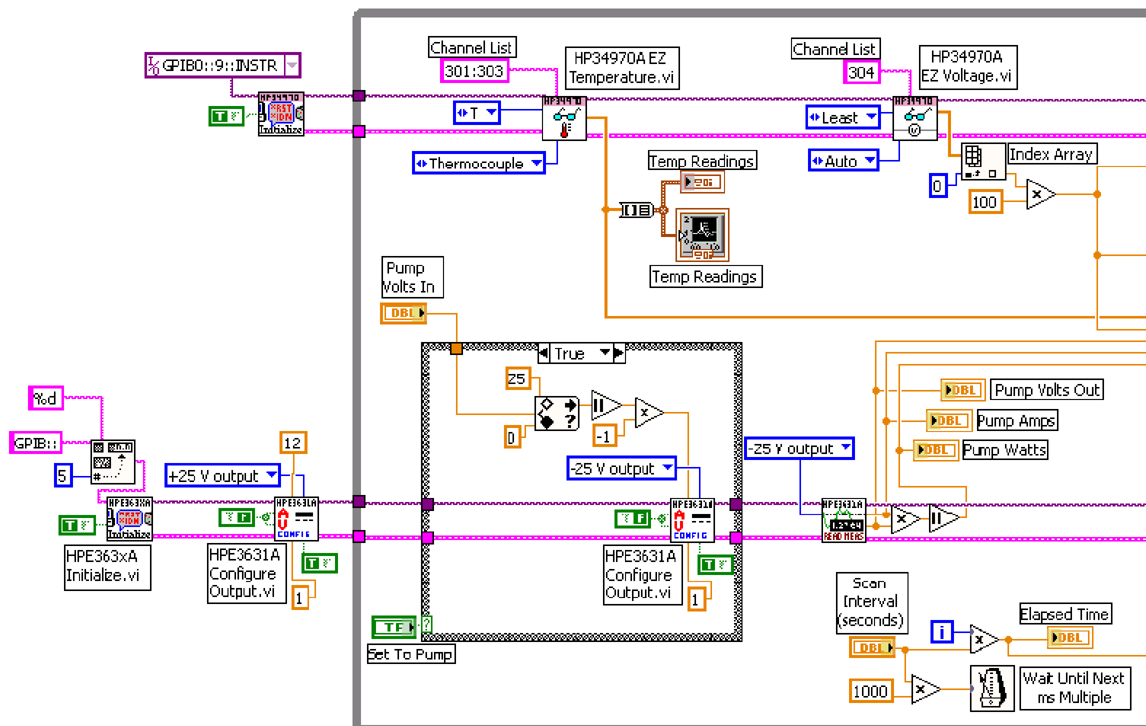


**Figure C.27:** *Hitran*, Left Side, Internal Case True

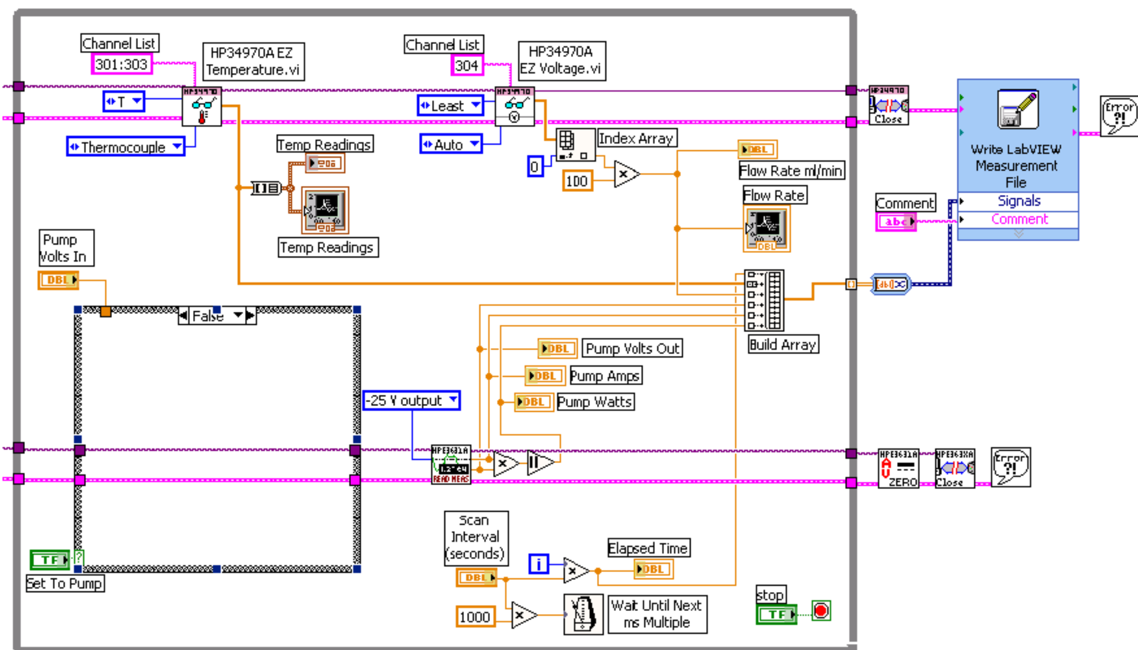


**Figure C.28:** *Hitran*, Left Side, Internal Case False

# APPENDIX D

# UNCERTAINTY ESTIMATES

The uncertainty analyses in this appendix follow the approach prescribed by Holman [15]. Suppose the result $R$ is a function of several independent variables $x_1$, $x_2$, $x_3$, . . . , $x_n$, or

$$R = R(x_{1,}x_2, x_3, ..., x_n) \tag{D.1}$$

Then, the uncertainty in the result, $w_R$, based on the uncertainties in the measured quantities, $w_1$, $w_2$, . . . , $w_n$ is

$$w_R = \left[ \left( \frac{\partial R}{\partial x_1} w_1 \right)^2 + \left( \frac{\partial R}{\partial x_2} w_2 \right)^2 + ... + \left( \frac{\partial R}{\partial x_n} w_n \right)^2 \right]^{\frac{1}{2}} \tag{D.2}$$

The uncertainty in the measured temperature for all experiments described in this thesis have a common temperature measurement error since the same data acquisition system, and type of thermocouples was used for each experiment. The total temperature measurement error is the sum of the error introduced by the data acquisition system, and the thermocouple itself. For the 34970A data acquisition/switch unit *Agilent* quotes a temperature measurement error of ± 1°C for up to 1 year after factory calibration (*Agilent* does not warranty any accuracy specifcations beyond the one year calibration interval). This includes measurement error, switching error, transducer conversion error, and the error of the built-in thermocouple reference junction of the 34901A plug-in module. Therefore, the total temperature measurement error equals ± 1.5 °C (1°C plus 0.5 °C thermocouple error) for all experiments described in this thesis.

The following representative example uses the uncertainty analysis approach above to estimate the uncertainty in the calculation of $U$, the overal heat transfer coefficient for the vacuum flask. Solving Equation 6.1 for $U$, one obtains

$$U = -\frac{mc_p}{At} \ln \left( \frac{T - T_\infty}{T_o - T_\infty} \right) \tag{D.3}$$

Substituting $m = \rho V$, $V = \pi r^2 L$, and $A = 2\pi r\,(L + r)$ into Equation D.3 yields

$$U = -\frac{\rho r L c_p}{2t(L + r)} \ln \left( \frac{T - T_\infty}{T_o - T_\infty} \right) \tag{D.4}$$

where $\rho$ is the density of water (assumed constant), $L$ is the internal vacuum flask length, $r$ is the inner radius of the vacuum flask, $c_p$ is the specific heat of water (assumed constant), $T$ is the average temperature of the water inside the vacuum flask at any time, $t$, $T_o$ is the average initial temperature of the water within the flask, $T_\infty$ is the average ambient temperature outside the flask, and $U$ is the overall heat transfer coefficient through the vacuum flask. Written in terms of measured quantities, Equation D.4 represents the explicit relation used to calculate $U$. This means $U$ is a function of six variables

$$U = U(r, L, t, T, T_o, T_\infty) \tag{D.5}$$

In order to estimate the uncertainty in the calculated result for $U$ based on the uncertainties of the six quantities, one must first estimate the uncertainties in $T, T_o, T_\infty$ because they represent calculated averages. Recall $T$ is the average of the thermocouple readings within the vacuum flask

$$T = \frac{T_1 + T_2 + T_3 + ... + T_n}{n} \tag{D.6}$$

where $n = 12$ in our case. Applying Equation D.2 to Equation D.6 gives

$$w_T = \left[ \left( \frac{\partial T}{\partial T_1} w_{T1} \right)^2 + \left( \frac{\partial T}{\partial T_2} w_{T2} \right)^2 + ... + \left( \frac{\partial T}{\partial T_n} w_{Tn} \right)^2 \right]^{\frac{1}{2}} \tag{D.7}$$

$$w_T = \left[ n \left( \frac{\partial T}{\partial T_n} w_{Tn} \right)^2 \right]^{\frac{1}{2}} \tag{D.8}$$

$$w_T = \left[ n \left( \frac{\partial T}{\partial T_n} \right)^2 w_{Tn}^2 \right]^{\frac{1}{2}} \tag{D.9}$$

$$w_T = \left[ n \left( \frac{1}{n} \right)^2 w_{Tn}^2 \right]^{\frac{1}{2}} \tag{D.10}$$

The quantity $w_{Tn}$ represents the total temperature measurement error and equals $\pm$ 1.5 °C, as previously mentioned. Equation D.10 may now be used to estimate the

uncertainty in $T$

$$w_T = \left[12\left(\frac{1}{12}\right)^2(1.5)^2\right]^{\frac{1}{2}} \tag{D.11}$$
$$w_T = 0.4330 \tag{D.12}$$

Similarly for $T_\infty$, where $n = 8882$

$$w_{T_\infty} = \left[8882\left(\frac{1}{8882}\right)^2(1.5)^2\right]^{\frac{1}{2}} \tag{D.13}$$
$$w_{T_\infty} = 0.0159 \tag{D.14}$$

$T_o$ represents a twice averaged quantity. Applying Equation D.10 with $w_{Tn} = 0.4330$, and $n = 360$

$$w_{T_o} = \left[360\left(\frac{1}{360}\right)^2(.433)^2\right]^{\frac{1}{2}} \tag{D.15}$$
$$w_{T_o} = 0.0228 \tag{D.16}$$

Having found the uncertainties in $T, T_o, T_\infty$, one can apply Equation D.2 to Equation D.4

$$w_U = \left[\begin{array}{c} \left(\frac{\partial U}{\partial r}w_r\right)^2 + \left(\frac{\partial U}{\partial L}w_L\right)^2 + \left(\frac{\partial U}{\partial t}w_t\right)^2 + \\ \left(\frac{\partial U}{\partial T}w_T\right)^2 + \left(\frac{\partial U}{\partial T_0}w_{T_o}\right)^2 + \left(\frac{\partial U}{\partial T_\infty}w_{T_\infty}\right)^2 \end{array}\right]^{\frac{1}{2}} \tag{D.17}$$

where

$$\frac{\partial U}{\partial r} = -\frac{\rho L^2 c_p \ln\left(\frac{T-T_\infty}{T_o-T_\infty}\right)}{2t(L+r)^2} \tag{D.18}$$
$$\frac{\partial U}{\partial L} = -\frac{\rho r^2 c_p \ln\left(\frac{T-T_\infty}{T_o-T_\infty}\right)}{2t(L+r)^2} \tag{D.19}$$
$$\frac{\partial U}{\partial t} = \frac{\rho r L c_p \ln\left(\frac{T-T_\infty}{T_o-T_\infty}\right)}{2t^2(L+r)} \tag{D.20}$$
$$\frac{\partial U}{\partial T} = -\frac{\rho r L c_p}{2(T-T_\infty)(L+r)t} \tag{D.21}$$
$$\frac{\partial U}{\partial T_0} = \frac{\rho r L c_p}{2(T_o-T_\infty)(L+r)t} \tag{D.22}$$
$$\frac{\partial U}{\partial T_\infty} = -\frac{\rho r L c_p (T-T_o)}{2(T_\infty-T_o)(T_\infty-T)(L+r)t} \tag{D.23}$$

Table D.1 gives the values used to estimate the uncertainty in the calculation of the overall heat transfer coefficient, $w_U$ for *Run E*.

**Table D.1:** *Run E* values used in estimate of uncertainty of $U$

| Quantity | Value | Uncertainty, ± | Source |
|---|---|---|---|
| $\rho$ | 970.874 kg/m$^3$ | - | Constant [16] |
| $c_p$ | 4199 J/kg·K | - | Constant [16] |
| $r$ | 0.0381 m | $1.27 \times 10^{-5}$ | Measured |
| $L$ | 2.0772 m | $7.93 \times 10^{-4}$ | Measured |
| $t$ | 86400 s | 0.001 | Measured |
| $T$ | 348.46 K | 0.4330 | Calculated from Measurement |
| $T_o$ | 362.07 K | 0.0228 | Calculated from Measurement |
| $T_\infty$ | 294.68 K | 0.0159 | Calculated from Measurement |

Substituting the table values into the partial derivatives above

$$\frac{\partial U}{\partial r} = 5.135 \quad (D.24)$$

$$\frac{\partial U}{\partial L} = 0.00173 \quad (D.25)$$

$$\frac{\partial U}{\partial t} = -2 \times 10^{-6} \quad (D.26)$$

$$\frac{\partial U}{\partial T} = -0.0164 \quad (D.27)$$

$$\frac{\partial U}{\partial T_0} = 0.0131 \quad (D.28)$$

$$\frac{\partial U}{\partial T_\infty} = 0.00331 \quad (D.29)$$

and substituting into Equation D.17 gives

$$w_U = \left[ \begin{array}{c} (5.135 \cdot 1.27 \times 10^{-5})^2 + (0.00173 \cdot 7.93 \times 10^{-4})^2 + \\ (-2 \times 10^{-6} \cdot 0.001)^2 + (-0.0164 \cdot 0.433)^2 + \\ (0.0131 \cdot 0.0228)^2 + (0.00331 \cdot 0.0159)^2 \end{array} \right]^{\frac{1}{2}} \quad (D.30)$$

$$w_U = 0.007116 \text{ W/m}^2 \cdot \text{K or } 3.57\ \% \quad (D.31)$$

This uncertainty estimate was repeated for *Run A* through *Run D*, and serves as a representative example of all other uncertainty estimates presented herein.

# REFERENCES


[1] Bennett, G. A., *Active Cooling for Downhole Instrumentation: Miniature Thermoacoustic Refrigerator*. PhD dissertation, University of New Mexico, 1991.

[2] Bennett, G. A., "Compact acoustic refrigerator." The United States of America as Represented by the United States Department of Energy, June 1992. U.S. Patent 5,165,243.

[3] Blanton, R. W., "New capabilities in pyroflasks," *Symposium of High-Temperature Well-Logging Instrumentation*, June 1986. Los Alamos National Laboratory Report LA-10745-C.

[4] Boesen, G. F., "Downhole thermoelectric refrigerator." Borg-Warner Corporation, Mar. 1983. U.S. Patent 4,375,157.

[5] Cerro-Alloy:, "Physical data and applications.." CerroMetal Products Co. Bellefonte, Pa, 1995.

[6] Champness, E. and Champness, A. T., "Downhole drilling tool cooling," Feb. 1998. U.S. Patent 5,715,895.

[7] de Kanter, S., "Downhole tool cooling system." Halliburton Company, Oct. 1983. U.S. Patent 4,407,136.

[8] Desbrandes, R., *Encyclopedia of Well Logging*. Houston, Texas: Gulf Publishing Company, 1985.

[9] DiFoggio, R., "Downhole sorption cooling of electronics in wireline logging and monitoring while drilling." Baker Hughes, Inc., Jan. 2002. U.S. Patent 6,341,498.

[10] Dincer, I. and Rosen, M. A., *Thermal Energy Storage, Systems and Applications*. New York, New York: McGraw Hill, Inc., seventh ed., 2002.

[11] Flores, A. G., "Apparatus and method for actively cooling instrumentation in a high temperature environment." Schlumberger Technology Corporation, Dec. 1997. U.S. Patent 5,701,751.

[12] Gissler, R. W., "Thermal insulation vessel." Halliburton Energy Services, Inc., Apr. 2001. U.S. Patent 6,220,346.

[13] Gray, G. R., *Composition and Properties of Oil Well Drilling Fluids*. Houston, Texas: Gulf Publishing Company, fourth ed., 1981.

[14] Halliday, D., Resnick, R., and Walker, J., *Fundamentals of Physics*. New York, New York: John Wiley and Sons, Inc., fifth ed., 1997.

[15] Holman, J. P., *Experimental Methods for Engineers.* New York, New York: McGraw Hill, Inc., 2001.

[16] Incropera, F. P. and DeWitt, D. P., *Fundamentals of Heat and Mass Transfer.* New York, New York: John Wiley and Sons, Inc., fifth ed., 2002.

[17] Lamers, M. D. and Martelli, V. P., "Well logging evaporative thermal protection system." Measurement Analysis Corporation, Feb. 1981. U.S. Patent 4,248,298.

[18] Martin, F. S. and Bearden, J. L., "Downhole motor cooling and protection system." Baker Hughes, Inc., Sept. 1996. U.S. Patent 5,554,897.

[19] McCluskey, F. P., Das, D., Jordan, J., Grzybowski, R., Fink, J., Condra, L., and Torri, T. C., "Packaging of electronics for high temperature applications," *The International Journal of Microcircuits and Electronic Packaging*, vol. 20, no. 3, pp. 409–423, 1997.

[20] McCluskey, F. P., Grzybowski, R., and Podlesak, T., *High Temperature Electronics.* New York, New York: CRC Press, 1995.

[21] Owens, S. and Bouldin, B., "Downhole system for extending the life span of electronic components." PES, Inc., Aug. 1996. U.S. Patent 5,547,028.

[22] Owens, S., Bouldin, B., and Elliot, G., "Integrated converter for extending the life span of electronic components." PES, Inc., Feb. 1998. U.S. Patent 5,720,342.

[23] Owens, S., Bouldin, B., and Elliot, G., "Vacuum insulated converter for extending the life span of electronic components." PES, Inc., Mar. 1998. U.S. Patent 5,730,217.

[24] Parrot, R. A., Song, H., and Chen, K.-C., "Cooling system for downhole tools," Jan. 2002. U.S. Patent 6,336,408.

[25] Schultz, R. L., "Refrigerant-cooled downhole tool and method." Halliburton Company, Nov. 1993. U.S. Patent 5,265,677.

[26] Smolen, J. J., *Cased Hole and Production Log Evaluation.* Tulsa, Oklahoma: PennWell Books, 1996.

[27] Turner, W. E., Seppa, R., and Turner, W. E., "Cooled electrical system for use downhole," Aug. 1999. U.S. Patent 5,931,000.

[28] Turner, W. E., Seppa, R., Turner, W. E., and Sallwasser, A. J., "Cooled electrical system for use downhole." APS Technology, Inc., Oct. 2000. U.S. Patent 6,134,892.

[29] Wolk, P., "Well logging electronics cooling system," June 1987. U.S. Patent 4,671,349.